Cellulose nanofibril-guided orienting response of supramolecular network enables superstretchable, robust, and antifatigue hydrogel

Siheng Wang,[1,2,4] Le Yu,[2,4] Xiangzheng Jia,[3,4] Lei Zhang,[1] He Liu,[1,*] Enlai Gao,[3,*] and Chaoji Chen[2,*]

*Correspondence: liuhe.caf@gmail.com (H.L.); enlaigao@whu.edu.cn (E.G.); chenchaojili@whu.edu.cn (C.C.)

Received: June 27, 2024; Accepted: September 19, 2024; Published Online: September 24, 2024; https://doi.org/10.59717/j.xinn-mater.2024.100092

GRAPHICAL ABSTRACT

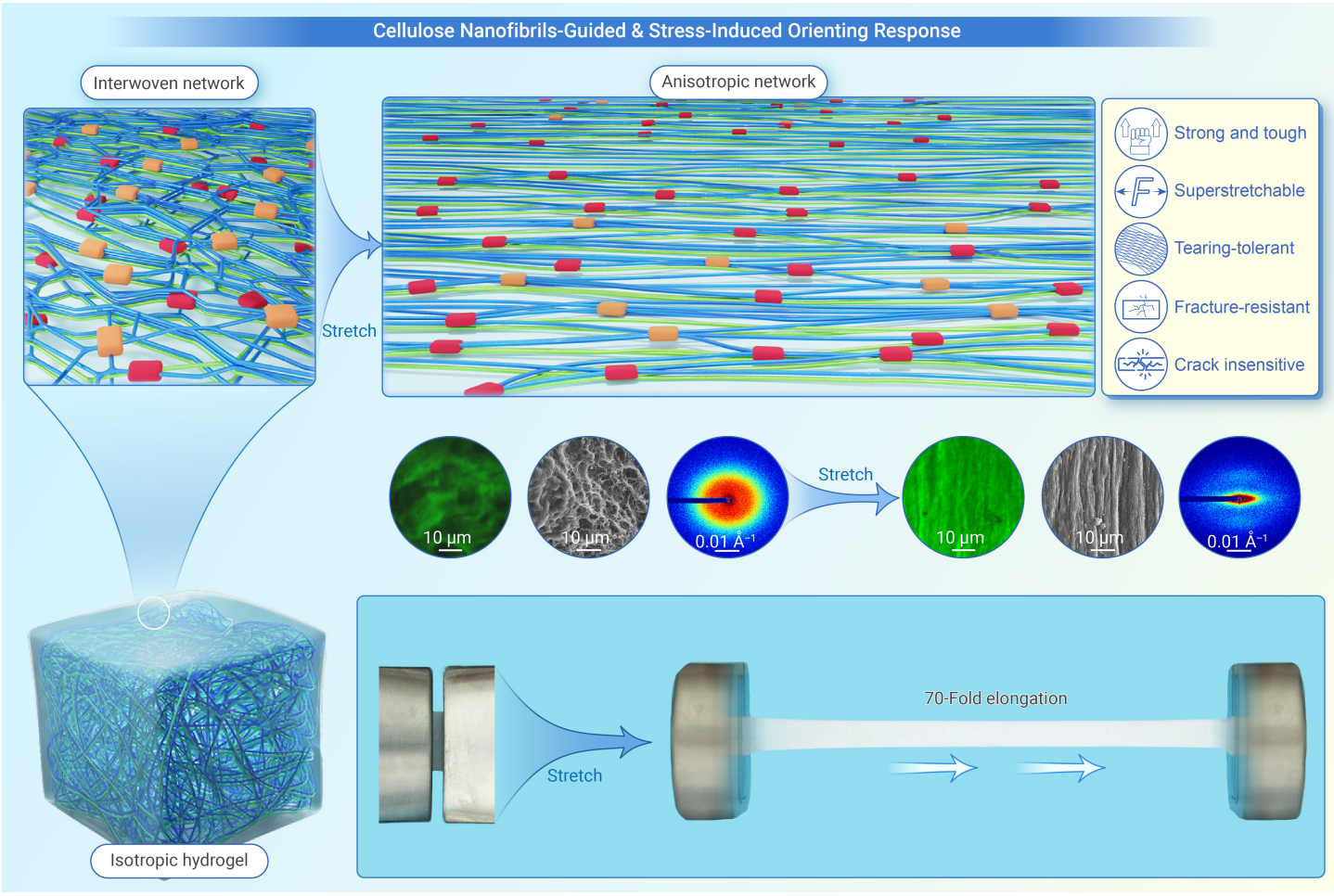

PUBLIC SUMMARY

- The high-performance hydrogel is constructed via cellulose nanofibril-guided orienting response of network.
- The supramolecular assembly process of cellulosic network from isotropic to aligned structure is revealed.
- The enabling hydrogel combines superstretchability, ultrarobustness, and fatigue-resistance.

Cellulose nanofibril-guided orienting response of supramolecular network enables superstretchable, robust, and antifatigue hydrogel

Siheng Wang,[1,2,4] Le Yu,[2,4] Xiangzheng Jia,[3,4] Lei Zhang,[1] He Liu,[1,*] Enlai Gao,[3,*] and Chaoji Chen[2,*]

[1]Key Laboratory of Biomass Energy and Material, Jiangsu Province; Key Laboratory of Chemical Engineering of Forest Products, National Forestry and Grassland Administration; National Engineering Research Center of Low-Carbon Processing and Utilization of Forest Biomass; Jiangsu Co-Innovation Center of Efficient Processing and Utilization of Forest Resources, Institute of Chemical Industry of Forest Products, Chinese Academy of Forestry, Nanjing 210042, China

[2]Hubei Biomass-Resource Chemistry and Environmental Biotechnology Key Laboratory, School of Resource and Environmental Sciences, Wuhan University, Wuhan 430079, China

[3]Department of Engineering Mechanics, School of Civil Engineering, Wuhan University, Wuhan 430072, China

[4]These authors contributed equally

*Correspondence: liuhe.caf@gmail.com (H.L.); enlaigao@whu.edu.cn (E.G.); chenchaojili@whu.edu.cn (C.C.)

Received: June 27, 2024; Accepted: September 19, 2024; Published Online: September 24, 2024; https://doi.org/10.59717/j.xinn-mater.2024.100092

Citation: Wang S., Yu L., Jia X., et al., (2024). Cellulose nanofibril-guided orienting response of supramolecular network enables superstretchable, robust, and antifatigue hydrogel. The Innovation Materials **2(3)**: 100092.

Hydrogels featuring randomly networked matrix typically show poor mechanical strength owing to the weak interchain interactions of the matrix. Encouragingly, the stretchability and toughness of hydrogel materials along a certain direction were recently improved to an unprecedented level with the design of structured and oriented matrix, the realization of excellent and concurrently isotropic mechanical performance for hydrogels now become the next- research goal. Herein, a self-assembling process of poly(vinyl alcohol) (PVA) macromolecular chain and cellulose nanofibril (CNF) induced by the salting-out effect was reported, which allowed the formation of a strongly hydrogen-bonded PVA-CNF supramolecular matrix. The resulting hydrogel, in any direction, can show an ultra-high stretchability of 7,400% and a true tensile strength of 420 MPa through the orientation of the supramolecular matrix. The robustness of the supramolecular interaction between PVA and CNF was experimentally demonstrated by the fact that the hydrogel showed a high fracture energy (reaching up to 95.7 kJ m^{-2}) and low notch sensitivity (fatigue threshold of 3,203 J m^{-2}), even outperforming most state-of-the-art anisotropic hydrogels. These results highlight that constructing supramolecular interaction among various components of gel matrix holds great promise for the design of future gel materials with the extraordinary mechanical performance.

INTRODUCTION

Due to the unique combination of many merits including flexibility, softness, and wetness, hydrogel has been considered one of the most promising engineering materials in various fields of soft robotics, artificial skins, wearable, and implantable electronics, etc.[1–3] Nevertheless, the matrices of conventional hydrogels are loosely crosslinked, thus are prone to mechanical failure once deformed.[4] Despite the energy dissipation theory, i.e., utilization of sacrificial bonds or structures has been widely adopted to strengthen the hydrogel, the application of hydrogels is still severely limited by the trade-off of mechanical properties, simultaneous achievement of high true strength (> 100 MPa), stretchability (> 2,000%), and fracture toughness (> 10 kJ m^{-2})[5–7] to fulfill the practical requirements remains pressing and challenging.

Encouragingly, during the past decade, anisotropic hydrogels can alleviate these mechanical demands.[8–13] However, as previously reported,[9] on account of the high orientation degree of the matrix structure of anisotropic hydrogels, their mechanical property parameters along the direction vertical to matrix alignment are typically a small percentage that along the alignment direction. Moreover, the manufacture of anisotropy hydrogels is limited to some laborious and energy-intensive methods (e.g., freeze-casting and ice-templating methods).[8,14–16] Consequently, developing more facile and economic approach towards the preparation of hydrogels possessing excellent mechanical properties without anisotropy is the next-stage goal of the hydrogel research community. Motivated by the excellent mechanical strength resulting from the aligned matrix structure of anisotropic hydrogels, one can envisage that the transformation of a randomly-networked matrix into an anisotropic architecture during stretching, with the prerequisite that the original matrix has certain compliance, can favor substantial improvements in mechanical performance of the hydrogels.[17–21] Salting-out treatment, as a facile yet feasible approach, has been developed to achieve mechanically strengthened hydrogels due to its ability to make aggregated polymer chains.[9,22–28] We hypothesize that the salting-out effect could be used to assist in the construction of an isotropic matrix with a dense aggregated network structure, which allows the matrix to achieve a certain degree of extension upon deformation. Distinct from the traditional anisotropic hydrogels demonstrating a preformed aligned matrix, the matrix of the above-conceptualized hydrogel is isotropic, thus theoretically is capable of delivering identical mechanical behavior in any direction.

Herein, for the first time, we propose an in situ self-assembly strategy to prepare supramolecular hydrogels assisted by the salting-out effect. As a proof-of-demonstration, two widely-used hydroxyl-abundant building blocks, poly(vinyl alcohol) (PVA) and cellulose nanofibrils (CNFs), were introduced to prepare an hydrogen-bonded (H-bonded) supramolecular hydrogel.[29–33] As demonstrated, a heavily interweaved PVA-CNF matrix could be formed by salting out-induced polymer chain aggregation, the tensile process directs the extensive formation of highly-aligned PVA-CNF assembly, making the hydrogel behave like other well-established anisotropic hydrogels to provide an astonishing fracture strain of 7,400% and meanwhile a true strength of 420 MPa (Figures 1A, S1 & S2). Especially, CNF with a large aspect ratio and salting-out assistance synergistically play a key role in inducing the orientation of the supramolecular network under tensile, enabling significant strengthening and toughening of the hydrogel compared to those controlled hydrogels without CNF guiding or salting out effects (Figure 1B). Additionally, benefiting from simplicity of the preparation approach, processing the hydrogel into various complicated shapes and scaling up the production could be readily realized to meet the practical application requirements (Figure S3). To give us a direct glimpse on the mechanical performance advantages of our supramolecular hydrogel, the mechanical properties parameters in terms of stretchability, true strength, fatigue resistance, tear tolerance, compressibility, and fracture toughness are visualized in the radar plots (Figure 1C). This design principle—utilizing H-bond interactions on supramolecular chemistry and stretch-induced structural transformations to provide highly oriented networks—may be applied to other polymers, for future high-performance soft materials.

MATERIALS AND MOTHODS

Preparation of CNFs

CNFs were produced by (2,2,6,6-tetramethylpiperidin-1-yl)oxidanyl (TEMPO) oxidation of biomass cellulose as before.[30] Briefly, 0.045 mol of NaClO per g of cellulose was fully reacted to obtain TEMPO oxidized CNFs under the condition that the pH of the system was maintained at 10–10.2. The resulting CNFs contained 1.28 mmol g^{-1} surface carboxylate groups (Figure S4). The average diameter and length of the obtained CNFs were 8.3 ± 1.3 nm and 200–800 nm, respectively, as confirmed by the surface morphology of the nanofibril (Figure S5). In addition, the strong and sharp peak at 1,608 cm^{-1} in the infrared curve of the CNF is attributed to the stretching vibration of the carbonyl moiety in the carboxyl group, and compared with the cellulose, the CNF still belongs to the cellulose I-type structure (Figure S6).

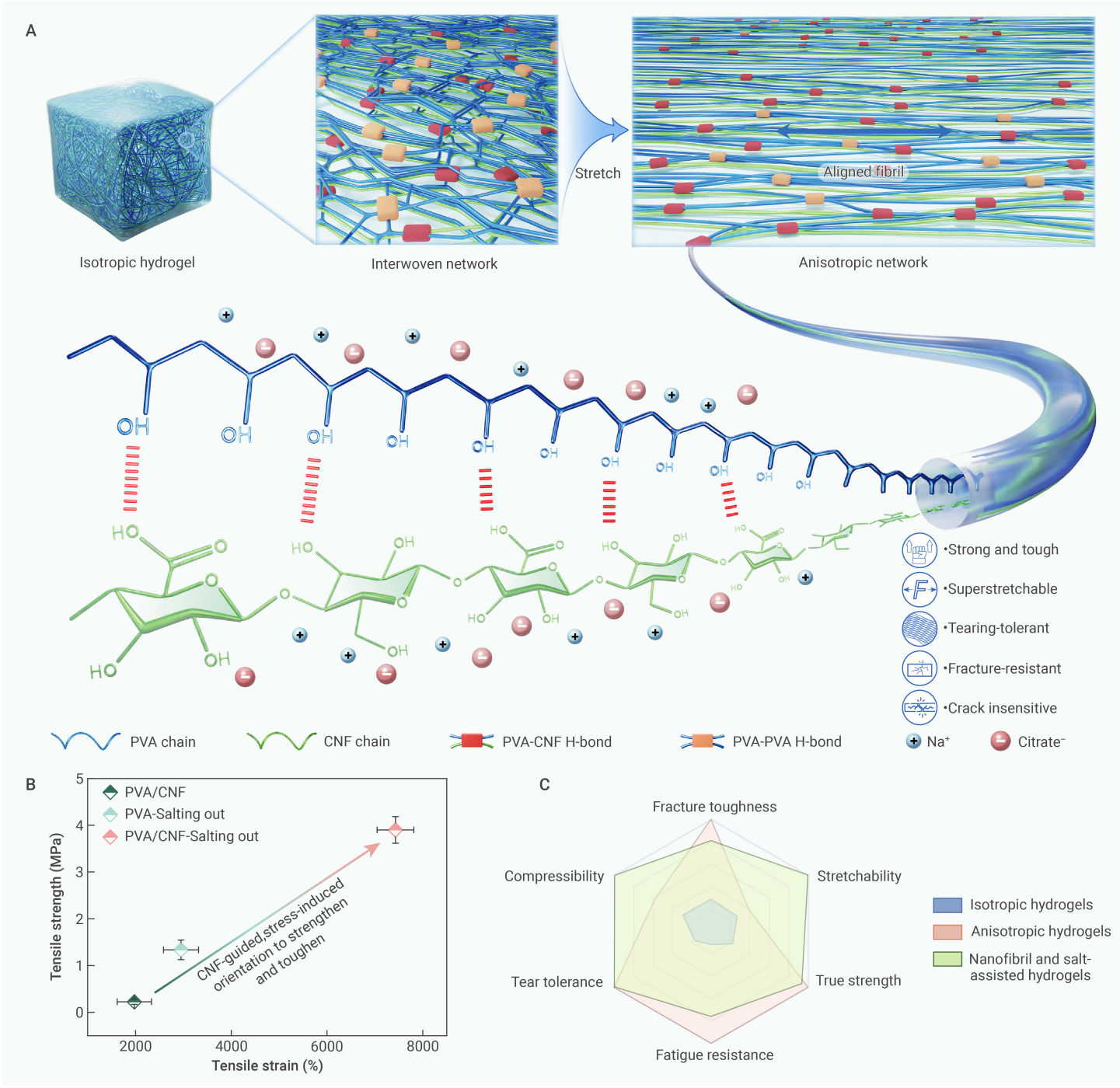

Figure 1. Design principle for the high-performance hydrogel (A) Fabrication of the PVA/CNF-Salting out hydrogel. By coupling the nanofibril and salting-out effect, based on H-bond interactions on supramolecular chemistry, an interwoven homogeneous network is formed between the PVA and CNF chains. An anisotropic network is realized induced by stretch. (B) Comparison of tensile strength and strain of PVA/CNF, PVA-Salting out, and PVA/CNF-Salting out hydrogels. (C) Radar plot showing comparisons among nanofibril and salt-assisted hydrogels (green area), isotropic hydrogels (blue area), and anisotropic hydrogels (red area). The data used are summarized in Tables S1 -S2. Error bars show the standard deviation from three independent specimens.

These favorable results all indicate that the successful acquisition of the CNF as consistent with the existing work.[34] For ease of use, the fabricated CNFs suspension (roughly 1 wt% solid content) was stored at 4°C for further preparation of hydrogels.

Preparation of salt solution

A 0.5 M sodium citrate solution was obtained by dissolving anhydrous sodium citrate powder in DI water. After sonicating for 10 min to remove air bubbles, a clear solution was prepared for later use.

Synthesis of PVA/CNF hydrogel

A uniform mixture of 10 wt% PVA and CNF was prepared by dissolving PVA powder in an aqueous CNF suspension with vigorous stirring and heating (90°C), where the mass of CNF was 5 wt% of the mass of PVA. After degassing by sonication for 1 h, a clear homogeneous mixture was obtained. To generate the freeze-thawed hydrogel, the regular freeze-casting method was used to cast the resulting mixture into cylindrical or cubic molds, frozen at −20°C for 8 h, and thawed at 25°C for 3 h, and this process was repeated for 3 cycles. Freeze-thawed hydrogels achieved with PVA and CNF mixture as well as pure PVA solution were denoted as PVA/CNF hydrogel and PVA hydrogel, respectively.

Fabrication of PVA/CNF-Salting out hydrogels

The PVA/CNF-Salting out hydrogel was prepared by immersing the PVA/CNF hydrogel into a 0.5 M sodium citrate solution for 24 h under ambi-

ent temperature. As a control, the PVA hydrogel was subjected to the same process to obtain the PVA-Salting out hydrogel.

DFTB calculations

Density functional theory-based tight-binding (DFTB) calculations were carried out using DFTB+ package.[35] All DFTB computations were performed with DFT-D3 dispersion correction with Becke-Jonhson damping.[36,37] The 3-ob-1 Slater-Koster set of parameters was employed.[38–40] Energy-minimized optimization tests were conducted using a conjugate gradient algorithm with a force-threshold criterion of 10^{-6} Hartree/Bohr. The models of PVA-PVA chains, CNF-CNF chains, PVA-CNF chains, PVA-water, CNF-water, and Salt-water were constructed to calculate the binding energies. The aperiodic boundary conditions were adopted along all directions with vacuum layer over 3 nm. The binding energy for each model was calculated as the sum of the energies of the isolated chains/molecules minus the total energy of the adsorbed structure upon structural optimization (normalized per atom).

Molecular dynamics simulation

To investigate the enhanced effect of CNF, all-atom molecular dynamics (MD) simulations were performed using large-scale atomic/molecular massively parallel simulator (LAMMPS) computational package.[41] The polymer consistent force field (PCFF) was adopted to describe the interatomic potentials.[42,43] The long-range Columbia interaction was included using particle-particle-particle mesh (PPPM) method, while the van der Waals interaction was described by the 6/9 Lennard-Jones potential with a cutoff distance of 1.0 nm. To integrate the Newton equations of motion, the Verlet algorithm was adopted with a time step of 0.5 fs. For comparing the rigidity of single chain, CNF and PVA chain with length of ~9 nm was surrounded by solvent environment filled with water molecules. Periodic boundary conditions along all directions were adopted. During the thermostat process, the temperature increased from nearly 0 K to room temperature of 300 K, which was then equilibrated for 1 ns. The radius of gyration (R_g) and end-to-end distance were utilized to characterize the compactness of the polymer chains, demonstrating the flexibility of PVA. Besides, we also calculated the persistence length of PVA and CNF chains considering that polymers will behave like a rigid rod at room temperature for lengths shorter than the persistence length. The results indicate that PVA chains are much more flexible than CNF chains, supporting our analyses on R_g and end-to-end distance.

For blend system of PVA, CNF, and water molecules, different molecules were blended into a box using PACKMOL package for specific ratios.[44] The mixtures with different water content (from 0 wt% to 90 wt%) were constructed by regulating the number of water molecules and then were equilibrated at 300 K in NPT ensemble. In all mixtures, the number of PVA and CNF chains remains a constant, and each chain is approximately 9 nm in length. To reduce the influence of thermal disturbance, the trajectory in the last 0.2 ns was adopted to analyze the H-bonds using VMD program. In comparison, we also performed simulations of PVA hydrogels with different water content from 0 wt% to 90 wt%. Herein, number of H-bonds per node, calculated by dividing the total number of H-bonds by the number of PVA/CNF chains, was adopted to focus on the enhanced effect of CNF.

Furthermore, a model with two amorphous PVA chains bridged by straight CNF chains was constructed to explore the contribution to strain. To ensure quasi-static loading, the uniaxial tensile strain was applied by uniaxially moving the atoms at the end with a tensile velocity of 3 m/s. The evolution of strain and pulling force provides insights into the differences in loading and deformation capacities between the two structures.

Finite element analysis simulation

To simulate the mechanical response of different hydrogel materials, numerical simulations were carried out with ABAQUS 2018 (SIMULIA, France). We used linear elastomer as a constitutive model to qualitatively reveal the underlying mechanism for the tensile test with pre-crack in mechanical properties. We employed a two-dimensional structure model for simulation. For the four systems of PVA, PVA/CNF, PVA-Salting out, and PVA/CNF-Salting out, their properties were used to construct the material parameters for the simulation, such as Young's modulus (0.008, 0.013, 0.042, and 0.05 MPa, respectively) and Poisson's ratio (0.3, 1.3, 2.3, and 3.3, respectively). Then, the cross-sections of the four materials were created and applied to the corresponding two-dimensional plane strain model. Next, we built the analysis step and set the corresponding time increment and minimum increment step requirements. At the same time, the corresponding field variable output was set in the analysis step module to simulate the crack growth of the finite element. Subsequently, the crack was pre-made in the interaction module to simulate the tension of the notched hydrogels, and the program was set to allow crack growth. In the simulation of crack growth, we used maximum principal stress criterion (Maxps Damage)[45] as the damage initiation and propagation criteria to qualitatively reveal the underlying mechanism for the tensile test with pre-crack in mechanical properties:

$$f = \{\langle \sigma_{max} \rangle / \sigma^0_{max}\}$$

Where σ^0_{max} is the value of critical maximum principal stress. When f in the range of $1.0 \le f \le 1.0 + f_{tol}$, the crack propagates.

In the load module, the bottom fixed boundary condition was used for all models, and the top was set with an upward tensile displacement boundary condition. In the mesh module, the entire model was meshed using plane strain quadrilateral elements, and the mesh type was a two-dimensional plane strain model. Finally, in the job module, a stretching program was created to obtain the calculation results.

Characterization

Transmission electron microscope (TEM) and atomic force microscopy (AFM) of CNFs were conducted using JEM-2100 UHR (JEOL, Japan) and RTESP-300 (Bruker, USA) instruments to observe the size. 3D macrostructure analyses of freeze-dried hydrogels were performed in a Zeiss Xradia 510 Versa 3D X-ray microscope (XRM), with a voltage of 60 kV and a power of 10 W. The obtained images were reconstructed via Carl Zeiss's Object Research Systems (ORS) image analysis program. Confocal laser scanning microscopy (CLSM) (LSM710, Zeiss, Germany) was performed to measure the pore structure of hydrogels stained with fluorescent dye solution. Scanning electron microscope (SEM) images of hydrogels were gained with environmental scanning electron microscopy (JSM-7600 Fs, Hitachi, Japan). In situ stretching small-angle X-ray scattering (SAXS) measurement was based on a stretch station which can be controlled by wireless. SAXS data of hydrogels were recorded at different strains from a SAXSpoint 2.0 apparatus (Anton Paar, Germany). Raman spectroscopy and spatial Raman mapping were performed using a Raman imaging microscope (Thermo Scientific DXR2xi, USA). The wavelength of the excitation laser was 532 nm. Raman mappings (scan range 60 μm × 60 μm; depth of scanning, 20 μm; layer of scanning, 4 layers) were collected using the condition that the laser power was 7.0 mW, the exposure time was 1.3 s, and the scan time was 10, and the image pixel size was 3.0 μm. The collected spectra were preprocessed by using cosmic-ray removal, noise filtering, and normalization techniques. The peak intensity method developed by OMINC software was employed for calculating the H-bond domains. The X-ray diffraction (XRD) patterns of all freeze-dried hydrogels, cellulose, and CNFs in the diffraction angle (2θ) range from 10° to 60° were recorded utilizing Siemens D5000 X-ray diffractometer (Siemens, Germany) at a scanning speed of 5° min^{-1}. AVTMR20-010V-I NMR analyzer (Suzhou Niumag Corporation, China) with a probe of VTMR20-Q-10mm was employed to measure the relaxation time (T_2) values of all of the hydrogel samples. The magnet temperature was set to 25 ± 0.01 °C to ensure the constant rate of molecular motion for probing the system. The attenuated total internal reflectance Fourier transform infrared (ATR-FTIR) spectra of all hydrogels, freeze-dried hydrogels, cellulose, and CNFs were recorded in the wavenumber range from 4,000 to 500 cm^{-1} by a Fourier transform infrared spectrometer (Nicolet iS50, Thermo Fisher Scientific, USA). The high-resolution solid-state ^{13}C cross-polarization/magic-angle spinning (CP/MAS) nuclear magnetic resonance (NMR) spectra of all freeze-dried hydrogels were performed on a 600 MHz spectrometer equipped with a MAS probe (AVANCE NEO, Bruker, Germany).

RESULTS AND DISCUSSION

Characterization of the PVA-CNF interactions

Figure 2A displays the optical photograph of a cubic-shaped PVA/CNF-Salting out hydrogel with a side length of 4 cm, which shows no liquid leakage or volume shrinkage over a period of 100 h (ambient temperature),

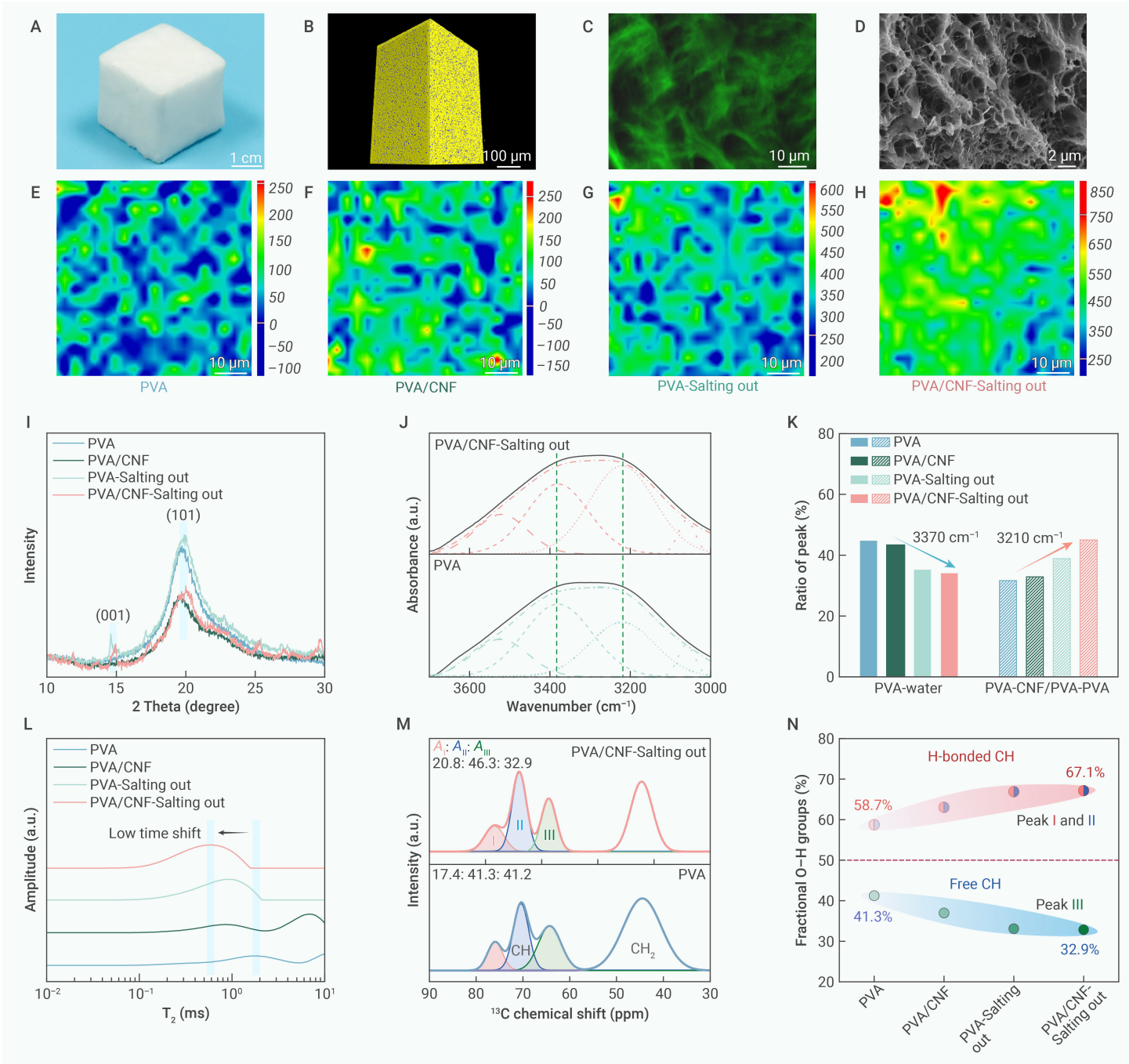

Figure 2. Morphology and structural analyses of hydrogels (A) The photograph of the PVA/CNF-Salting out hydrogel (4 × 4 × 4 cm). (B) Volume rendering presenting the overall microstructure of the PVA/CNF-Salting out hydrogel derived from the reconstructed 3D X-ray micro-CT image. (C-D) (C) Confocal and (D) scanning images showing the local microstructure of the PVA/CNF-Salting out hydrogel. (E–H) Reconstructed two-dimensional (2D) Raman images of the (E) PVA hydrogel, (F) PVA/CNF hydrogel, (G) PVA-Salting out hydrogel, and (H) PVA/CNF-Salting out hydrogel from the –OH bending vibration intensities, respectively. (I) XRD patterns of hydrogels. (J and K) ATR-FTIR (J) spectra and (K) ratios of the peaks located at 3,210 and 3,370 cm^{-1} of hydrogels. (L) Low-field ^{1}H NMR spectrums of hydrogels. (M-N) (M) High-resolution solid-state ^{13}C MAS NMR spectra of hydrogels and (N) corresponding fraction of free and H-bonded O–H groups according to peak area.

demonstrating its excellent structural stability. The reconstructed three-dimensional (3D) X-ray micro-computed tomography (micro-CT) image of the freeze-dried PVA/CNF-Salting out hydrogel reveals a uniform and isotropic pore structure, where blue indicates porous regions and yellow indicates non-porous regions (Figure 2B & Movie S1). Figures 2C-D show the confocal laser scanning microscopy (CLSM) and scanning electron microscopy (SEM) images of the PVA/CNF-Salting out hydrogel, compared to the loose macropores of the PVA hydrogel, the formation of a dense 3D interwoven network was demonstrated, which is tentatively attributed to the strong interaction of PVA and CNF (Figure S7), which is often observed in robust hydrogel materials.[46–49]

The impact of CNF on PVA-CNF intra-chain interactions under salting-out treatment was systematically investigated at the molecular level.[50] As first revealed by the 2D Raman images shown in Figures 2E–H, the intensity of the CH–OH bending vibration of the four hydrogel samples studied in this work follows the order PVA < PVA/CNF < PVA-Salting out < PVA/CNF-Salting out, which is a powerful proof of the ever-increasing H-bond density with the introduction of CNF and salting out mechanism in a baseline PVA hydrogel. The good spatial homogeneity and improved density of H-bond interactions in the PVA/CNF-Salting out hydrogel are also further supported by the 3D reconstructed Raman images shown in Figure S8. X-ray diffractometer (XRD) were performed to probe the microstructure evolution of the hydrogels under the salting-out effect. Four types of hydrogels all show an obvious characteristic peak localized at around 2θ = 19.9°, corresponding to the typical (101) planes of PVA.[51] Notably, both the PVA- and PVA/CNF-Salting out hydrogels show a significant new characteristic peak localized at 2θ = 14.9°. This peak

is assigned to the (001) crystal planes diffractions of the crystalline PVA as previously reported.[51–53] Compared with the initial PVA and PVA/CNF hydrogels, the intensity of (101) planes exhibits a slightly increasing trend and the appearance of new (001) planes in the PVA- and PVA/CNF-Salting out hydrogels, which jointly suggest that salting-out treatment can enable the reassembly of the PVA and CNF into new a topological structure.[27] In addition, the introduction of CNF causes a significant decrease in the typical (101) planes of PVA, which is due to the fact that the strong H-bonds between PVA and CNF lead to the rearrangement of PVA chains and the inhibition of crystallization, which is a good agreement with previous reports.[54,55]

The attenuated total internal reflectance Fourier transform infrared (ATR-FTIR) spectra of all hydrogels feature a broad hydroxyl vibration band deconvoluted into four subpeaks at around 3,530, 3,370, 3,210, and 3,060 cm^{-1} (Figures 2J & S9). Among them, the subpeaks localized at 3,370 and 3,210 cm^{-1} correspond to the H-bond of PVA-water and PVA-PVA/PVA-CNF, respectively.[56,57] The subpeaks around 3,530 and 3,060 cm^{-1} are attributed to the non-H-bonded O–H stretching mode in the PVA chains as reported.[58,59] These peaks are observed in all hydrogels because free hydroxyl groups and H-bonded hydroxyl groups both existed in the systems. The abundance of different H-bonded patterns is determined by their integral area ratio. It is observed that the inter- and intra-macromolecular H-bond instead of macromolecule-water H-bond interactions become the dominant. More quantitatively, a much higher inter- and intra-macromolecular H-bond ratio of 45.0% as compared to 31.6%, 32.8% and 38.9% of the PVA hydrogel before/after salting-out treatment and PVA/CNF hydrogel are observed, respectively. This is in good accordance with the low-filed NMR (LF NMR) results. The hydrogel releases more free water through combining the CNF and ion-enhancing approaches, resulting in a large amount of immediate and bound water,

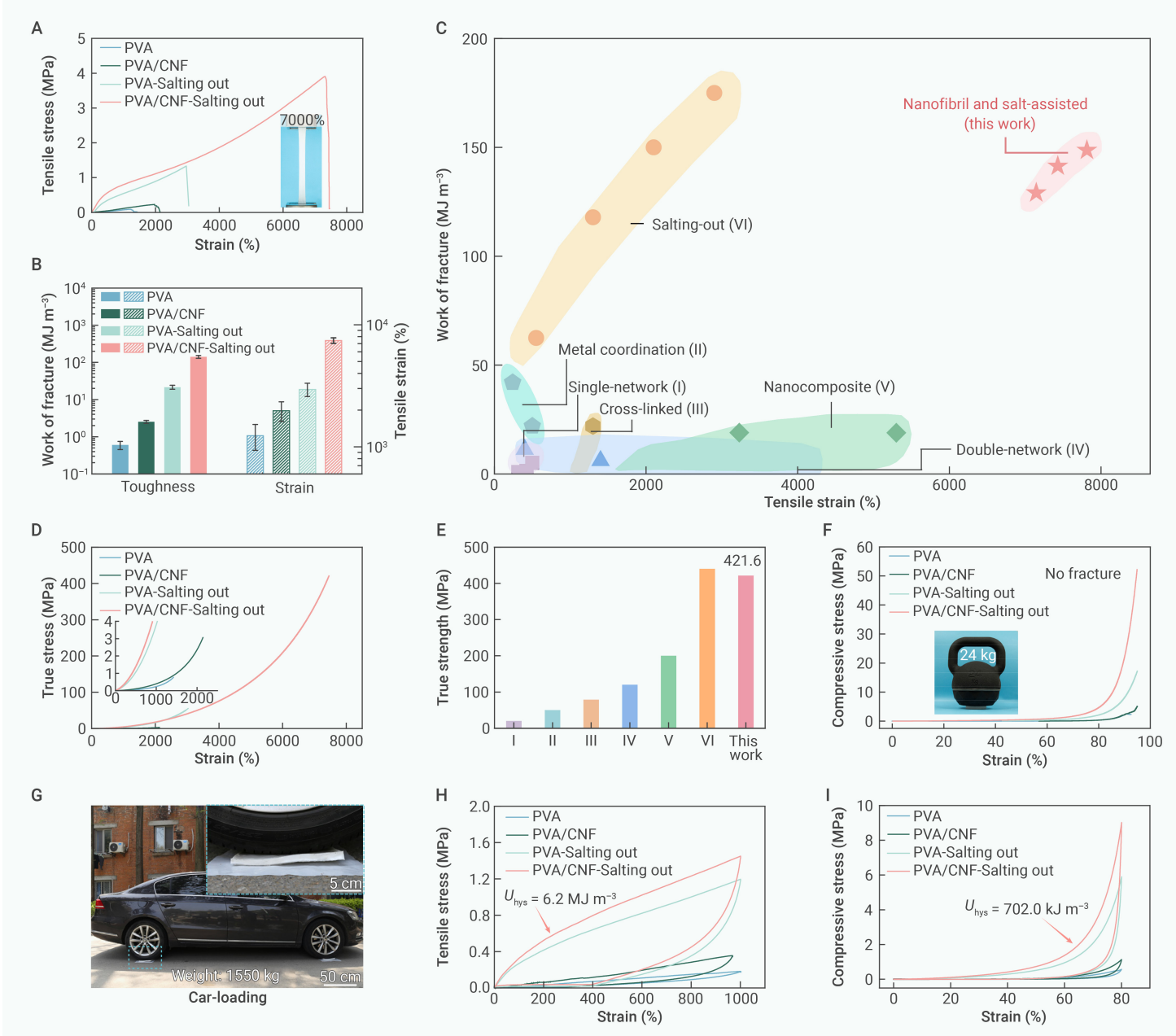

Figure 3. Tensile and compressive performance of hydrogels (A) Typical tensile stress-strain curves of hydrogels. The inset image is that the PVA/CNF-Salting out hydrogel is uniaxially stretched to 7,000% strain. (B) A comparison of work of fracture and tensile strain of hydrogels. (C) A comparison of the toughness and ultimate tensile strain of our obtained hydrogel with previously reported tough hydrogels. The data used are summarized in Tables S2 and S3. (D) Typical true tensile stress-strain curves of hydrogels and the corresponding enlarged one showing in the inset. (E) True strength of our resultant hydrogel and other tough hydrogels. I, II, III, IV, V, VI correspond to the six types of hydrogels described in (C). The data used are summarized in Tables S2 -S3. (F) Typical compressive stress-strain curves of hydrogels. The inset image shows that a sample can easily hold a weight of 24 kg that is 400-fold its own weight. (G) Photographs of the PVA/CNF-Salting out hydrogel supporting the weight of a car, in which the structure remained intact after loading. (H) Tensile loading-unloading curves of hydrogels to a strain of 1,000%. (I) Compressive loading-unloading curves of hydrogels to a strain of 80%. Error bars show the standard deviation from three independent specimens.

which is ascribed to the H-bonded-induced confinement behavior on the mobility of water among chains (Figure S10).[60] As expected, the LF NMR spectral displays that the bound water-related relaxation time (T_2) in the PVA/CNF-Salting out hydrogel is shifted toward shorter times, suggesting an intense H-bond network (Figure 2L).

We also applied solid-state ^{13}C magic-angle spinning (MAS) nuclear magnetic resonance (NMR) spectroscopy to gain ulteriorly insights into molecular evolutions in hydrogel systems. As presented in Figure 2M and Figure S11, in addition to the characteristic peak of $-CH_2$ located at 44.6 ppm, the characteristic peak of the CH moiety could be deconvoluted into three component peaks (I, II, and III) localized at around 76.1, 70.9, and 64.5 ppm, corresponding to the inter- and intra-molecular H-bonded CH (I and II) and free CH (III), respectively.[61,62] The combined relative area ratio of peaks I and II increase from 58.7% for the virgin PVA hydrogel to 67.1% for the PVA/CNF-Salting out hydrogel, meaning the stronger existence of H-bond crosslinking after salting out treatment (Figure 2N), which is mainly responsible for the formation of the nano- and microscopic isotropic network.

Quantitative study of mechanical properties

Tensile and compressive strain-stress were conducted to quantitatively investigate the mechanical properties of hydrogels, the fracture strain of PVA/CNF-Salting out hydrogel is measured to be up to ~7,430%, concurrently with an ultimate stress of 3.9 MPa (Figure 3A). These two parameters are significantly higher than that of other three control hydrogel samples, about 43.3 and 6.1 times that of the PVA hydrogel, respectively. The inset image in Figure 3A indicates that the PVA/CNF-Salting out hydrogel has the ability to be uniaxially stretched to 7,000% strain. As a result of the simultaneous achievement of high tensile strength and fracture strain, a high toughness of 141.4 MJ m^{-3} that is 240 times that of the PVA hydrogel is delivered by the PVA/CNF-Salting out hydrogel (Figures 3B & S12). Figure S13 shows that a pillar-like hydrogel sample with 0.45 cm^2 cross-sectional area is able to hold a 12-kg dumbbell, about 2,400 times that of the hydrogel. Due to the excellent stretchability is not achieved through substantially reducing the water content (Figures S14 & S15) and/or preforming a directionally-structured matrix with extra steps (prestretching or others), all the above mechanical properties show independency of the loading direction (Figure S16), differentiating our PVA/CNF-Salting out hydrogel with previous ones.[63,64]

The unique combination of high stretchability and toughness places our PVA/CNF-Salting out hydrogel at the upper right corner of the Ashby plot of tensile strain versus toughness (Figure 3C). In consideration of the dramatical decreased cross-sectional area at conditions of high elongation over 7,000%, the corrected true tensile strength of the PVA/CNF-Salting out hydrogel is estimated to be ~420 MPa (Figure 3D). This result, to our best knowledge, also ranks the toughest anisotropic hydrogels ever reported (Figure 3E).[9] Notably, compared with the PVA-salting out hydrogel and PVA/CNF hydrogel, the PVA/CNF-salting out hydrogel show more outstanding stretchability and strength, underscoring that CNF aided with salting out synergistically promote improved mechanical performance of the hydrogel. This can be explained by the introduction of CNF which can guide the formation of enhanced H-bonded supramolecular network assisted by salting out treatment.

Figure 3F shows the compressive strain-stress curves of four investigated hydrogels under 95% compressive strain, the PVA/CNF-Salting out hydrogel shows the highest stress of 51.7 MPa, which is 21.4, 10.1, and 2.9 times that of the pure PVA hydrogel, PVA/CNF hydrogel, and PVA-Salting out hydrogel, showing excellent compressibility and compressive strength (Figures S17 & S18). The high toughness and compression strength are further visually presented by that a 23 × 20 × 2 cm hydrogel plate can withstand the run over of a 1,550 kg car and rapidly recover its original appearance (Figure 3G & Movie S2).

Tensile and compressive loading-unloading tests were carried out to investigate the energy dissipation mechanism to gain further insight into H-bond interaction in different hydrogels. Under tensile mode, the PVA/CNF-Salting out hydrogel exhibits a high mechanical hysteresis (U_{hys}, up to 6.2 MJ m^{-3} at 1,000% strain) and a large residual strain (around 400%) after unloading (Figures 3H & S19); under compression mode the U_{hys} is measured to be up to 702.0 kJ m^{-3} at 80% compression (Figures 3I & S20). U_{hys} of the PVA/CNF-Salting out hydrogel obtained at both two testing modes are approximately 21.6% and 56.6% higher than that of the PVA-Salting out hydrogel, 5.9 to 14.5 times and 10.1 to 16.6 times that of the two investigated hydrogels without salting out treatment, indicating its superior energy dissipation ability facilitated by high-density sacrificial H-bonds (Figures S21 & S22).

Fracture tolerance and fatigue resistance of hydrogels

To deepen the knowledge on the relationship between the fracture behavior of hydrogels and their H-bond networks, the fracture toughness of different hydrogels was thoroughly investigated via a combined approach of trouser-tearing and pure shear tests.[65,66] It is found that, from the trouser-like tear test, the PVA/CNF-Salting out hydrogel shows significantly higher tear displacement and tear force than the other three types of comparative hydrogels (Figures 4A-B). The PVA/CNF-Salting out hydrogel consequently exhibits a high tearing energy (T) of 11.9 kJ m^{-2}, which is 1.8 times that of the PVA-Salting out hydrogel of 6.5 kJ m^{-2}, and 17.0 times that of the PVA/CNF hydrogel of 0.7 kJ m^{-2} (Figures 4C & S23). Moreover, the notched PVA/CNF-Salting out hydrogel presents superb crack tolerance in the fracture process with a maximum strain around 4,000% from the pure shear test (Figure 4D). The calculated fracture energy (Γ) of the PVA/CNF-Salting out hydrogel is as high as 95.7 kJ m^{-2}, delivering 3.4 times that of the PVA-Salting out hydrogel of 28.3 kJ m^{-2}, and 23.9 times that of the PVA/CNF hydrogel of 4.0 kJ m^{-2} (Figures 4E & S24). These observations demonstrate the excellent fracture toughness of the PVA/CNF-Salting out hydrogel and the positive reinforcing effect of CNF aided with salting out treatments in retarding crack growth. This can be attributed to the strong H-bond interactions between PVA and CNF due to the salting-out effect, in which CNF functioned as a stress dissipation and transfer center.[67] Finite element analysis (FEA) simulation of the stress distribution was performed to visualize the stress-concentration evolution at the crack tip in the notched hydrogels (Figure 4F & Movie S3). It is shown that the stress at the crack propagation site of the PVA/CNF-Salting out hydrogel is around 102.9 kPa, significantly higher than that of other three hydrogels (6.6, 20.2, and 70.1 for the PVA, PVA/CNF, and PVA-Salting out hydrogel respectively), also theoretically highlighting the significant role of CNF aided with salting out in preventing crack propagation (Figure S25).

The cracking behavior was investigated by recording the crack propagation of the PVA/CNF-Salting out hydrogel with a precut notch under different constant strains (Figures S26 & S27). It can be found that the maximum stress and strain do not show catastrophic degradation during consecutive stretch at fixed strains of 50, 100%, and 150%, indicating that the tensile stress of each deformation is comparable and the hydrogel delivers negligible crack growth. The result demonstrates that the PVA/CNF-Salting out hydrogel can exhibit excellent fatigue resistance with a record-high fatigue threshold (Γ_0) of 3,202.7 J m^{-2}, which is about twice that of the 2D isotropically fatigue-resistant hydrogel (Figure 4G).[15] We applied an energy release rate (G_c) of 2,949.7 J m^{-2} to a notched sample over 10,000 cycles, and observed no crack propagation or redirection, profoundly validating this extremely high fatigue threshold (Figure 4H), making it one of the most promising fatigue-resistant hydrogel materials (Figure 4I). The unprecedented improvements of mechanical properties, in terms of ultra-stretchability, high strength, toughness, tear tolerance, as well as fatigue resistance, underscore that the hydrogel material developed herein may access an entirely unexplored property area.

Mechanism for strengthening and toughening hydrogels

As shown in Figure 5A, the PVA/CNF-Salting out hydrogel could be elongated to 70 times of its initial length, showing extraordinary stretchability. A combined approach of in situ CLSM, SEM, and small-angle X-ray scattering (SAXS) were performed to reveal the underlying mechanism behind the extraordinary stretchability of the PVA/CNF-Salting out hydrogel (Figures 5B–D). Both the CLSM and SEM images shown in Figure 5B-C reveal that, compared to the original state of random distribution, the fibrils in the PVA/CNF-Salting out hydrogel at 1,500% and 4,000% strains become highly oriented, indicating that the ease of directional realignment of the fibrils is mainly responsible for the excellent stretchability. From the 2D SAXS patterns of the PVA/CNF-Salting out hydrogel at different strains, we find that as the tensile strain increases, the scattering ring gradually become rhombic, and

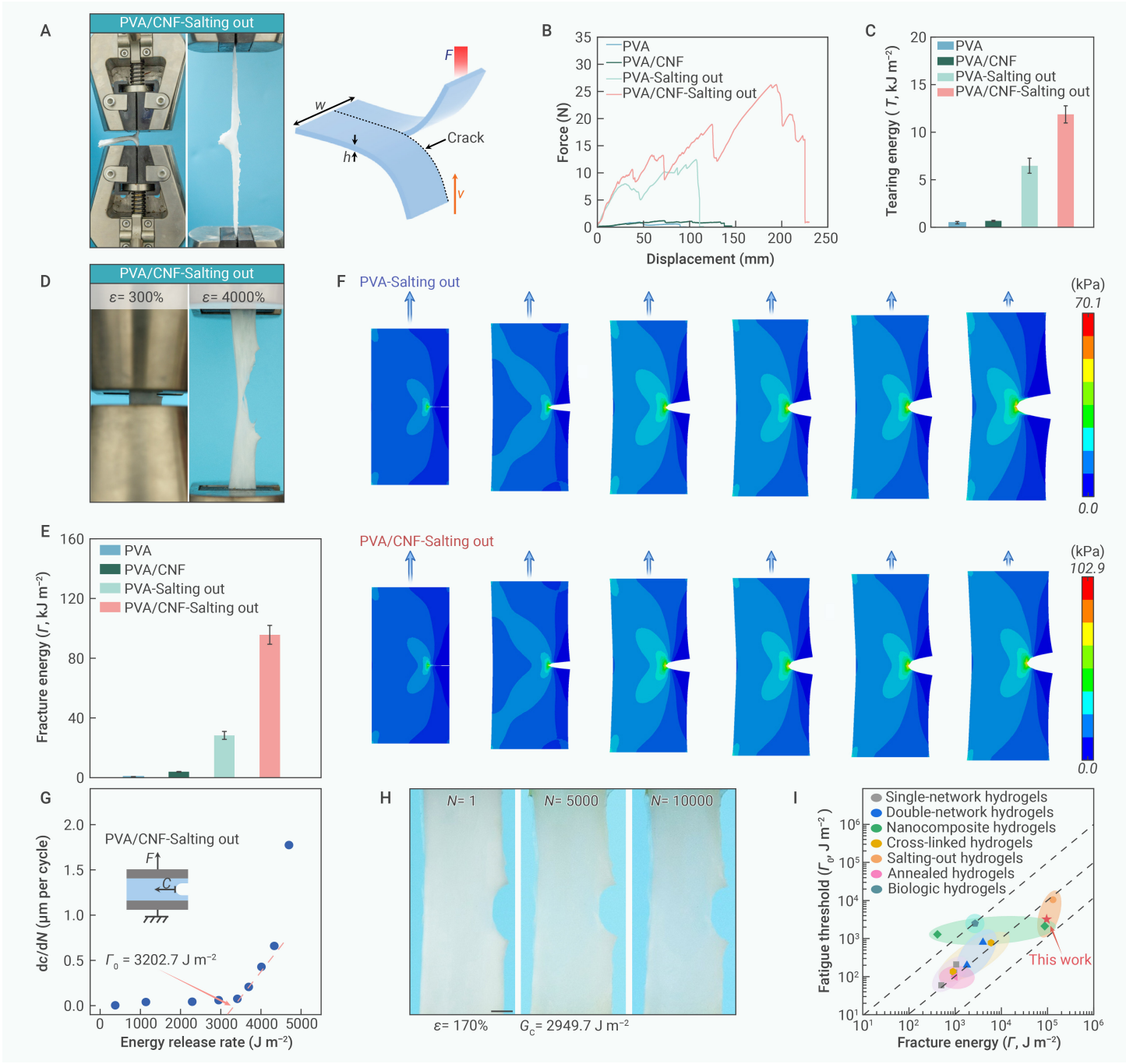

Figure 4. Antifatigue performance of hydrogels (A) Photographs of tearing tests of the PVA/CNF-Salting out hydrogel and schematic of the tearing test trouser-like samples, with important dimensions labelled. (B-C) (B) Tearing force-displacement curves of the hydrogels and (C) the corresponding tearing energy (T). (D) Photographs of pure shear tests of the PVA/CNF-Salting out hydrogel. (E) Fracture energy (Γ) of the hydrogels. (F) The FEA nephogram of the stress distribution inside the PVA/CNF-Salting out and PVA-Salting out hydrogels during crack propagation. The scale bar from blue to red indicates the stress concentration is from low to high. (G) The crack propagation per loading cycle, dc/dN, versus energy release rate for the PVA/CNF-Salting out hydrogel. (H) Validation of an energy release rate (G_c) of 2,949.7 J m^{-2} for the PVA/CNF-Salting out hydrogel sample using the single-notch test at the cycle number of 3,000, 5,000, and 10,000. Scale bars, 25 mm. (I) A comparison between this work and previously reported antifatigue hydrogels plotted by fatigue threshold (Γ_0) versus fracture energy (Γ). The data used are summarized in Table S4. Error bars show the standard deviation from three independent specimens.

the scattering signal changes from a spherically distributed state to ellipsoidal distribution along the equatorial direction, revealing the PVA-CNF assembly become directionally bundled along the strain direction (Figure 5D). This sharply contrasts with that no obvious orientation is observed for the PVA hydrogel without salting out treatment (Figure S28).[29,68,69] The structural evolution of the PVA-Salting out hydrogel and PVA/CNF hydrogel show a similar trend with the PVA/CNF-Salting out hydrogel, albeit to a much lower extent, which is attribute to less pronounced H-bond interaction in the absence of CNF incorporation and/or salting out treatment (Figures S29 & S30).

The extracted 1D SAXS profiles of hydrogels also provide favorable evidences, i.e., the critical vector corresponding to the peak intensity shows a high-shifting trend from 0.484 to 0.698 Å^{-1} with increasing strain from 0% to 4,000% in the PVA/CNF-Salting out hydrogel, which demonstrates that the average distance L between adjacent aggregated domains shortens from 1.09 to 0.83 nm according to the Bragg expression (Figure S31).[70] While the PVA-Salting out hydrogel presents higher L at the same tensile strain due to the absence of CNF, further revealing the positive contribution of CNF for guiding the cellulosic network to form aligned arrangements under deformation. A comparative analysis of above results points to the indispensable role of both incorporating CNF and salting out treatment in enabling superior stretchability, which also promotes the generation of strengthened and

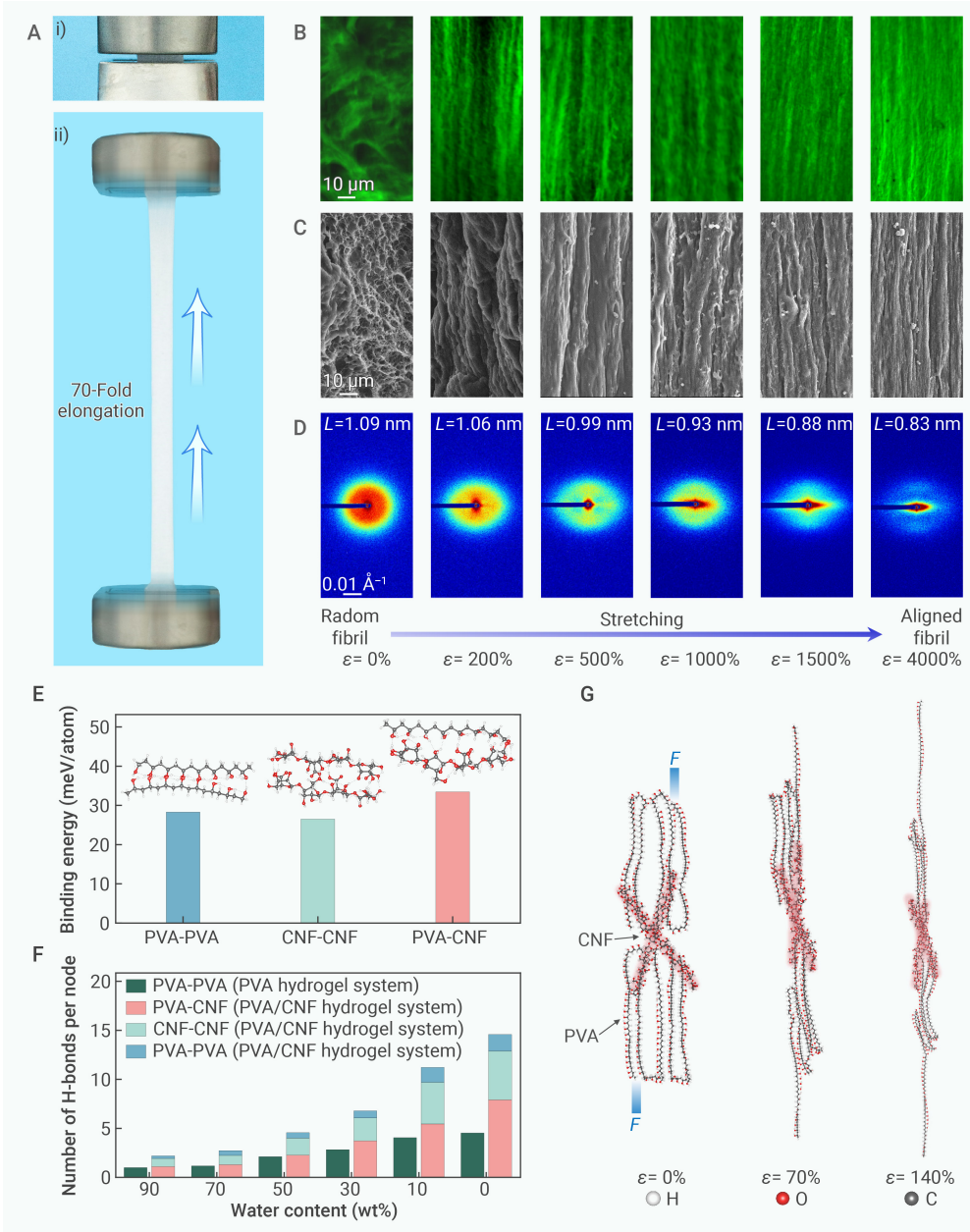

Figure 5. Structural evolution during stretching of the PVA/CNF-Salting out hydrogel (A) Photographs of the PVA/CNF-Salting out hydrogel stretched to a strain of 7,000%. i) represents the initial state and ii) represents the 70-fold elongated state. (B–D) (B) Confocal and (C) scanning images show the deformation of the PVA/CNF-Salting out hydrogel network from homogeneous structure to orientation during stretching and (D) the corresponding in situ SAXS patterns. Scale bars, 10 μm (in B and C); 0.01 $Å^{-1}$ (in D). (E) Binding energy of different molecules. (F) Number of H-bonds per node. (G) Simulation snapshots of PVA-CNF under tension.

toughened hydrogels.

DFTB combined with all-atom MD simulations were conducted to provide computational evidence on the salting-out effect and working mechanism of CNF at the molecular scale. First, the binding energy between various components of the investigated hydrogels was calculated to gain basic understanding of the intermolecular interaction. As shown in Figure S32, sodium citrate shows much higher binding energy with water (380 meV/atom) compared to PVA (86 meV/atom) and CNF (110 meV/atom), confirming the ability of sodium citrate to drive out water from the interspaces of the macromolecule matrix (Figure S33), known as the salting-out effect. The inter-molecular interaction calculation results, 28.31, 26.52, and 33.45 meV/atom respectively for PVA-PVA, CNF-CNF, and PVA-CNF, suggest PVA have a strong tendency to form PVA-CNF supramolecular assembly (Figure 5E).

To theoretically reveal the mechanism underlying the enhanced mechanical performance of PVA/CNF-Salting out hydrogel, to begin with, the kinetic behaviors of PVA and CNF chains (both with an initial length of 8.5 nm) in water were studied. After equilibration at room temperature (300 K) for 1 ns, the simulated radius of gyration (R_g, characterizing the compactness of the chain) and end-to-end distance (reflecting the rigidity and flexibility of the chain) demonstrate the high rigidity of CNF chain compared to PVA chain (Figure S34). DFTB calculations show that the persistence length of PVA and CNF chains are 0.55 nm and 6.04 nm, respectively (Figure S35). The curling behavior of PVA is believed to severely limit its interaction with adjacent PVA through H-bond interactions, as suggested by the H-bond density of intermolecular interaction node in PVA hydrogel and PVA/CNF hydrogel obtained from MD simulations (Figures S36 & S37): the number of H-bonds per node in PVA/CNF hydrogel is significantly higher than that of the PVA hydrogel, more importantly, H-bonds belong to PVA-CNF play a dominate role, jointly indicating the critical role of CNF in boosting H-bond density of the polymer matrix. Further considering that the salting out treatment can drive out water molecules among polymer chains to enable a localized low-water-content environment, hydrogel models with low water contents were constructed and simulated, which show significant increase in the number of H-bonds, providing solid theoretical evidence for salting out treatment in enabling denser H-bonded network (Figures 5F & S38). With the above merits, further simulation of a tensile test suggests that the CNF can strongly bond adjacent PVA chains, facilitating the dissipation of mechanical load by chain sliding and thus dramatically improving the tensile strain (Figures 5G, S39 & Movie S4). Theoretically, a small simulative PVA-CNF assembly can sustain a strain of up to 140%, promising an extraordinarily high stretchability of the practical PVA-CNF hydrogel.

Practical application demonstration

As an added benefit of the incorporation of sodium citrate during salting out treatment, the PVA/CNF-Salting out hydrogel shows a freezing point as low as −19°C, thus even at sub-zero temperatures, it can show high ionic conductivity (6.8 mS cm^{-1} at −10°C) and desirable mechanical performance, superior to most reported strong and ionic-conductive hydrogels (Figures S40–S42). Compared with the PVA-Salting out hydrogel, we found that, unexpectedly, the presence of CNF can significantly improve the ionic conductivity of hydrogel, maybe resulted from that the negatively charged CNF is susceptible to correlate with the cation and speed up the cation transport as previous works proposed (Figure S43).[71] Such a combination of high ionic conductivity and mechanical strength over a wide temperature allow us to demonstrate the broad application prospects, especially for scenarios call for long-term and reliable operation of the hydrogel parts (Figure S44 & S45). In a proof-of-concept demonstration, we applied this hydrogel as sensing element to continuously monitor the human movements and physiological signals, reproducible responses with high signal-to-noise ratio are observed over a wide temperature range, implying the long-term stability of the PVA/CNF-Salting out hydrogel for handling real-life applications (Figure S46 & Movies S5).

CONCLUSION

By incorporating CNF followed by salting-out treatment, we realized the transformation of a weakly H-bonded PVA hydrogel into a mechanically strong hydrogel featuring a strongly H-bonded PVA-CNF supramolecular matrix, showing an unprecedent combination of superstretchability (7,430%), true strength (420 MPa), fracture energy (95.7 kJ m^{-2}), and fatigue threshold (3,202.7 J m^{-2}). It was experimentally and theoretically revealed that the CNF guided, stress-induced orientation behavior of PVA-CNF assembly, and energy dissipation ability of the very high-density H-bonds formed among various components jointly contribute to the high stretchability and fatigue resistance. Considering the economic, efficiency, and effectiveness, we are convinced that, by constructing a densely H-bonded polymer/nanofiller matrix and leveraging the nanofibril-guided and stress-induced orientation mechanism to prepare a supramolecular hydrogel is a promising alternative strategy to previously developed methods of pre-stretching, ice-templating, etc.

REFERENCES

1. Yang, C. and Suo, Z. (2018). Hydrogel ionotronics. Nat. Rev. Mater. **3**: 125–142. DOI: 10.1038/s41578-018-0018-7.
2. Ye, Y., Yu, L., Lizundia, E., et al. (2023). Cellulose-based ionic conductor: an emerging material toward sustainable devices. Chem. Rev. **123**: 9204–9264. DOI: 10.1021/acs.chemrev.2c00618.
3. Liu, X., Liu, J., Lin, S., et al. (2020). Hydrogel machines. Mater. Today **36**: 102–124. DOI: 10.1016/j.mattod.2019.12.026.
4. Zhang, Y.S., and Khademhosseini, A. (2017). Advances in engineering hydrogels. Science **356**: eaaf3627. DOI: 10.1126/science.aaf3627.
5. Zhao, X. (2017). Designing toughness and strength for soft materials. Proc. Natl. Acad. Sci. USA **114**: 8138–8140. DOI: 10.1073/pnas.1710942114.
6. Zhao, X., Chen, X., Yuk, H., et al. (2021). Soft materials by design: Unconventional Polymer networks give extreme properties. Chem. Rev. **121**: 4309–4372. DOI: 10.1021/acs.chemrev.0c01088.
7. Gong, J.P. (2014). Materials both tough and soft. Science **344**: 161–162. DOI: 10.1126/science.1252389.
8. Shao, G., Hanaor, D.A.H., Shen, X., and Gurlo, A. (2020). Freeze casting: From low-dimensional building blocks to aligned porous structures-a review of novel materials, methods, and applications. Adv. Mater. **32**: 1907176. DOI: 10.1002/adma.201907176.
9. Hua, M., Wu, S., Ma, Y., et al. (2021). Strong tough hydrogels via the synergy of freeze-casting and salting out. Nature **590**: 594–599. DOI: 10.1038/s41586-021-03212-z.
10. Cui, K., and Gong, J.P. (2021). Aggregated structures and their functionalities in hydrogels. Aggregate **2**: e33. DOI: 10.1002/agt2.33.
11. Lin, S., Liu, J., Liu, X., and Zhao, X. (2019). Muscle-like fatigue-resistant hydrogels by mechanical training. Proc. Natl. Acad. Sci. USA **116**: 10244–10249. DOI: 10.1073/pnas.1903019116.
12. Zhang, Y., Li, D., Liu, Y., et al. (2024). 3D-bioprinted anisotropic bicellular living hydrogels boost osteochondral regeneration via reconstruction of cartilage-bone interface. The Innovation **5**: 100542. DOI: 10.1016/j.xinn.2023.100542.
13. Li, L., Zhang, Y., Lu, H., et al. (2020). Cryopolymerization enables anisotropic polyaniline hybrid hydrogels with superelasticity and highly deformation-tolerant electrochemical energy storage. Nat. Commun. **11**: 62. DOI: 10.1038/s41467-019-13959-9.
14. Liang, X., Chen, G., Lin, S., et al. (2021). Anisotropically fatigue-resistant hydrogels. Adv. Mater. **33**: 2102011. DOI: 10.1002/adma.202102011.
15. Liang, X., Chen, G., Lin, S., et al. (2022). Bioinspired 2D isotropically fatigue-resistant hydrogels. Adv. Mater. **34**: 2107106. DOI: 10.1002/adma.202107106.
16. Mredha, M.T.I., Guo, Y.Z., Nonoyama, T., et al. (2018). A facile method to fabricate anisotropic hydrogels with perfectly aligned hierarchical fibrous structures. Adv. Mater. **30**: 1704937. DOI: 10.1002/adma.201704937.
17. Liu, C., Morimoto, N., Jiang, L., et al. (2021). Tough hydrogels with rapid self-reinforcement. Science **372**: 1078–1081. DOI: 10.1126/science.aaz6694.
18. Zhang, S., Shi, W., and Wang, X. (2022). Locking volatile organic molecules by subnanometer inorganic nanowire-based organogels. Science **377**: 100–104. DOI: 10.1126/science.abm7574.
19. Wang, Z., Zheng, X., Ouchi, T., et al. (2021). Toughening hydrogels through force-triggered chemical reactions that lengthen polymer strands. Sciecne **373**: 193–196. DOI: 10.1126/science.abg2689.
20. Han, Z., Wang, P., Lu, Y., et al. (2022). A versatile hydrogel network–repairing strategy achieved by the covalent-like hydrogen bond interaction. Sci. Adv. **8**: eabl5066. DOI: 10.1126/sciadv.abl5066.
21. Jiang, G., Wang, G., Zhu, Y., et al. (2022). A scalable bacterial cellulose ionogel for multisensory electronic skin. Research **2022**: 1–11. DOI: 10.34133/2022/9814767.
22. Wu, S., Hua, M., Alsaid, Y., et al. (2021). Poly(vinyl alcohol) hydrogels with broad-range tunable mechanical properties via the hofmeister effect. Adv. Mater. **33**: 2007829. DOI: 10.1002/adma.202007829.
23. Cui, W., Zheng, Y., Zhu, R., et al. (2022). Strong tough conductive hydrogels via the synergy of ion - induced cross - linking and salting - out. Adv. Funct. Mater. **32**: 2204823. DOI: 10.1002/adfm.202204823.
24. Lloyd, G.O. and Steed, J.W. (2009). Anion-tuning of supramolecular gel properties. Nat. Chem. **1**: 437–442. DOI: 10.1038/nchem.283.
25. Jungwirth, P. and Cremer, P.S. (2014). Beyond hofmeister. Nat. Chem. **6**: 261–263. DOI: 10.1038/nchem.1899.
26. Sun, X., Mao, Y., Yu, Z., et al. (2024). A biomimetic "salting out-alignment-locking" tactic to design strong and tough hydrogel. Adv. Mater. **36**: 2400084. DOI: 10.1002/adma.202400084.
27. Xu, L., Qiao, Y., and Qiu, D. (2023). Coordinatively stiffen and toughen hydrogels with adaptable crystal-domain cross-linking. Adv. Mater. **35**: 2209913. DOI: 10.1002/adma.202209913.
28. Liu, D., Cao, Y., Jiang, P., et al. (2023). Tough, transparent, and slippery PVA hydrogel led by syneresis. Small **19**: 2206819. DOI: 10.1002/smll.202206819.
29. Wang, S., Zhang, L., Wang, Z., et al. (2024). Humidity - adaptive, mechanically robust, and recyclable bioplastic films amplified by nanoconfined assembly. Aggregate **Early View**: e643 DOI: 10.1002/agt2.643.
30. Zhang, L., Chen, L., Wang, S., et al. (2024). Cellulose nanofiber-mediated manifold dynamic synergy enabling adhesive and photo-detachable hydrogel for self-powered E-skin. Nat. Commun. **15**: 3859. DOI: 10.1038/s41467-024-47986-y.
31. Sun, X., Pang, Z., Zhu, Y., et al. (2023). All-cellulose hydrogel-based adhesive. The Innovation Materials **1**: 100040. DOI: 10.59717/j.xinn-mater.2023.100040.
32. Wang, Z., Xu, C., Qi, L., et al. (2024). Chemical modification of polysaccharides for sustainable bioplastics. Trends Chem. **6**: 314–331. DOI: 10.1016/j.trechm.2024.04.009.
33. Niu, X., He, Y., Musl, O., et al. (2024). Bark extractives as sources of carbon-efficient functional precursors and materials. The Innovation Materials **2**: 100074. DOI: 10.59717/j.xinn-mater.2024.100074.
34. Ye, Y., Zhang, Y., Chen, Y., et al. (2020). Cellulose nanofibrils enhanced, strong, stretchable, freezing - tolerant ionic conductive organohydrogel for multi - functional sensors. Adv. Funct. Mater. **30**: 2003430. DOI: 10.1002/adfm.202003430.
35. Hourahine, B., Aradi, B., Blum, V., et al. (2020). DFTB+, a software package for efficient approximate density functional theory based atomistic simulations. J. Chem. Phys. **152**: 124101. DOI: 10.1063/1.5143190.
36. Grimme, S., Antony, J., Ehrlich, S., et al. (2010). A consistent and accurate ab initio parametrization of density functional dispersion correction (DFT-D) for the 94 elements H-Pu. J. Chem. Phys. **132**: 154104. DOI: 10.1063/1.3382344.
37. Grimme, S., Ehrlich, S., and Goerigk, L. (2011). Effect of the damping function in dispersion corrected density functional theory. J. Comput. Chem. **32**: 1456–1465. DOI: 10.1002/jcc.21759.
38. Gaus, M., Goez, A., and Elstner, M. (2013). Parametrization and benchmark of DFTB3 for organic molecules. J. Chem. Theory Comput. **9**: 338–354. DOI: 10.1021/ct300849w.
39. Gaus, M., Lu, X., Elstner, M., et al. (2014). Parameterization of DFTB3/3OB for sulfur and phosphorus for chemical and biological applications. J. Chem. Theory Comput. **10**: 1518–1537. DOI: 10.1021/ct401002w.
40. Lu, X., Gaus, M., Elstner, M., et al. (2015). Parametrization of DFTB3/3OB for magnesium and zinc for chemical and biological applications. J. Phys. Chem. B **119**: 1062–1082. DOI: 10.1021/jp506557r.
41. Plimpton, S. (1995). Fast parallel algorithms for short-range molecular dynamics. J. Comput. Phys. **117**: 1–19. DOI: 10.1006/jcph.1995.1039.
42. Sun, H., Mumby, S.J., Maple, J.R., et al. (2002). An ab Initio CFF93 all-atom force field for polycarbonates. J. Am. Chem. Soc. **116**: 2978–2987. DOI: 10.1021/ja00086a030.
43. Lordi, V. and Yao, N. (2011). Molecular mechanics of binding in carbon-nanotube–polymer composites. J. Mater. Res. **15**: 2770–2779. DOI: 10.1557/jmr.2000.0396.
44. Martinez, L., Andrade, R., Birgin, E.G., et al. (2009). PACKMOL: A package for building initial configurations for molecular dynamics simulations. J. Comput. Chem. **30**: 2157–2164. DOI: 10.1002/jcc.21224.
45. Gallina, D. (2011). Finite element prediction of crack formation induced by quenching in a forged valve. Eng. Failure Anal. **18**: 2250–2259. DOI: 10.1016/j.engfailanal.2011.07.020.
46. Wang, S., Yu, L., Wang, S., et al. (2022). Strong, tough, ionic conductive, and freezing-tolerant all-natural hydrogel enabled by cellulose-bentonite coordination interactions. Nat. Commun. **13**: 3408. DOI: 10.1038/s41467-022-30224-8.
47. Alsaid, Y., Wu, S., Wu, D., et al. (2021). Tunable sponge-like hierarchically porous hydrogels with simultaneously enhanced diffusivity and mechanical properties. Adv. Mater. **33**: 2008235. DOI: 10.1002/adma.202008235.
48. Wang, S., Wang, Z., Zhang, L., et al. (2024). Sweat-adaptive adhesive hydrogel electronics enabled by dynamic hydrogen bond networks. Chem. Eng. J. **492**: 152290. DOI: 10.1016/j.cej.2024.152290.
49. Wang, Z., Wang, S., Zhang, L., et al. (2024). Highly strong, tough, and cryogenically adaptive hydrogel ionic conductors via coordination interactions. Research **7**: 0298. DOI: 10.34133/research.0298.
50. Zhao, D., Pang, B., Zhu, Y., et al. (2022). A stiffness-switchable, biomimetic smart material enabled by supramolecular reconfiguration. Adv. Mater. **34**: 2107857. DOI: 10.1002/adma.202107857.
51. Cao, J., Zhao, X., and Ye, L. (2020). Facile method to fabricate superstrong and tough poly(vinyl alcohol) hydrogels with high energy dissipation. Ind. Eng. Chem. Res. **59**:

10705–10715. DOI: 10.1021/acs.iecr.0c01083.
52. Assender, H.E., and Windle, A.H. (1998). Crystallinity in poly(vinyl alcohol) 2. Computer modelling of crystal structure over a range of tacticities. Polymer **39**: 4303–4312. DOI: 10.1016/s0032-3861(97)10297-x.
53. Hao, B., Ding, Z., Tao, X., et al. (2023). Atomic-scale imaging of polyvinyl alcohol crystallinity using electron ptychography. Polymer **284**: 126305. DOI: 10.1016/j.polymer.2023.126305.
54. Chen, H., Wei, P., Qi, Y., et al. (2023). Water-induced cellulose nanofibers/poly(vinyl alcohol) hydrogels regulated by hydrogen bonding for in situ water shutoff. ACS Appl. Mater. Interfaces **15**: 39883–39895. DOI: 10.1021/acsami.3c07989.
55. Li, Y., Ren, P., Sun, Z., et al. (2024). High-strength, anti-fatigue, cellulose nanofiber reinforced polyvinyl alcohol based ionic conductive hydrogels for flexible strain/pressure sensors and triboelectric nanogenerators. J. Colloid Interface Sci. **669**: 248–257. DOI: 10.1016/j.jcis.2024.05.011.
56. Xu, L., Gao, S., Guo, Q., et al. (2020). A solvent-exchange strategy to regulate noncovalent interactions for strong and antiswelling hydrogels. Adv. Mater. **32**: 2004579. DOI: 10.1002/adma.202004579.
57. Otsuka, E., Komiya, S., Sasaki, S., et al. (2012). Effects of preparation temperature on swelling and mechanical properties of PVA cast gels. Soft Matter **8**: 8129. DOI: 10.1039/c2sm25513h.
58. Tang, N., Jiang, Y., Wei, K., et al. (2024). Evolutionary reinforcement of polymer networks: A stepwise-enhanced strategy for ultrarobust eutectogels. Adv. Mater. **36**: 2309576. DOI: 10.1002/adma.202309576.
59. Zuo, B., Hu, Y., Lu, X., et al. (2013). Surface properties of poly(vinyl alcohol) films dominated by spontaneous adsorption of ethanol and governed by hydrogen bonding. The J. Phys. Chem. C **117**: 3396–3406. DOI: 10.1021/jp3113304.
60. Wang, J., Wu, B., Wei, P., et al. (2022). Fatigue-free artificial ionic skin toughened by self-healable elastic nanomesh. Nat. Commun. **13**: 4411. DOI: 10.1038/s41467-022-32140-3.
61. Liu, L., Zhu, M., Xu, X., et al. (2021). Dynamic nanoconfinement enabled highly stretchable and supratough polymeric materials with desirable healability and biocompatibility. Adv. Mater. **33**: 2105829. DOI: 10.1002/adma.202105829.
62. Kobayash, M., Ando, I., Ishii, Takahiro., et al. (1995). Structural study of poly (vinyl alcohol) in the gel state by high-resolution solid-state ^{13}C NMR spectroscopy. Macromolecules **28**: 6677–6679. DOI: 10.1021/ma00123a039.
63. Xu, L., Wang, C., Cui, Y., et al. (2019). Conjoined-network rendered stiff and tough hydrogels from biogenic molecules. Sci. Adv. **5**: eaau3442. DOI: 10.1126/sciadv.aau3442.
64. Ji, D., Park, J.M., Oh, M.S., et al. (2022). Superstrong, superstiff, and conductive alginate hydrogels. Nat. Commun. **13**: 3019. DOI: 10.1038/s41467-022-30691-z.
65. Bai, R., Chen, B., Yang, J., et al. (2019). Tearing a hydrogel of complex rheology. J. Mech. Phys. Solids **125**: 749–761. DOI: 10.1016/j.jmps.2019.01.017.
66. Bai, R., Yang, J., and Suo, Z. (2019). Fatigue of hydrogels. Eur. J. Mech. A. Solids **74**: 337–370. DOI: 10.1016/j.euromechsol.2018.12.001.
67. Li, W., Wang, X., Liu, Z., et al. (2024). Nanoconfined polymerization limits crack propagation in hysteresis-free gels. Nat. Mater. **23**: 131–138. DOI: 10.1038/s41563-023-01697-9.
68. Wang, Y., Huang, X., and Zhang, X. (2021). Ultrarobust, tough and highly stretchable self-healing materials based on cartilage-inspired noncovalent assembly nanostructure. Nat. Commun. **12**: 1291. DOI: 10.1038/s41467-021-21577-7.
69. Lei, Z., Gao, W., Zhu, W., et al. (2022). Anti - fatigue and highly conductive thermocells for continuous electricity generation. Adv. Funct. Mater. **32**: 2201021. DOI: 10.1002/adfm.202201021.
70. Lin, S., Liu, X., Liu, J., et al. (2019). Anti-fatigue-fracture hydrogels. Sci. Adv. **5**: eaau8528. DOI: 10.1126/sciadv.aau8528.
71. Zhou, Y., Chen, C., Zhang, X., et al. (2019). Decoupling ionic and electronic pathways in low-dimensional hybrid conductors. J. Am. Chem. Soc. **141**: 17830–17837. DOI: 10.1021/jacs.9b09009.

FUNDING AND ACKNOWLEDGMENTS

This work was supported by the National Natural Science Foundation of China (Grant No. 31890774) to H.L., the Forestry Science and Technology Innovation and Extension Project of Jiangsu Province (Grant No. LYKJ[2021]04) to H.L. C.C. thanks the National Natural Science Foundation of China (Grant No. 52273091) and the start-up fund (Grant No. 691000003) of Wuhan University for the financial support. The funders had no role in study design, data collection and analysis, decision to publish or preparation of the manuscript.

AUTHOR CONTRIBUTIONS

S.W., L.Y., and X.J. contributed equally to this work. H.L. and C.C. conceived the idea and supervised the project. S.W. and L.Y. performed most experiments and analysis. L.Z. assisted in completing the photographs of samples. E.G. and X.J. carried out the computational simulation and analyzed the results. H.L., E.G., C.C., S.W., L.Y., and X.J. wrote and revised the manuscript. All authors commented on the submitted version of the manuscript.

DECLARATION OF INTERESTS

The authors declare no competing interests.

DATA AND CODE AVAILABILITY

The authors declare that the main data supporting the findings of this study are available within the paper and its Supplemental Information. Extra data are available on reasonable request from the corresponding author.

SUPPLEMENTAL INFORMATION

It can be found online at https://doi.org/10.59717/j.xinn-mater.2024.100092

The Innovation Materials, *Volume 2*

Supplemental Information

Cellulose nanofibril-guided orienting response of supramolecular network enables superstretchable, robust, and antifatigue hydrogel

DOI: https://doi.org/10.59717/j.xinn-mater.2024.100092

Siheng Wang, Le Yu, Xiangzheng Jia, Lei Zhang, He Liu, Enlai Gao, Chaoji Chen

Table of Contents

Supplemental Materials and Methods

Supplemental Figures

Figure S1. Design of nanofibril and salt-assisted hydrogels.

Figure S2. Photographs of the PVA hydrogel and PVA/CNF-Salting out hydrogel.

Figure S3. Photographs of PVA/CNF-Salting out hydrogels with different shapes and large scales.

Figure S4. Typical conductometric titration curve of obtained CNFs for determining the surface charge density.

Figure S5. Surface morphology analysis of our obtained CNFs.

Figure S6. Structural characterizations of our obtained CNFs.

Figure S7. Micromorphology analysis of the PVA hydrogel and PVA/CNF-Salting out hydrogel.

Figure S8. Raman spectra and reconstructed 2D Raman images of hydrogels.

Figure S9. ATR-FTIR spectra of hydrogels.

Figure S10. Low-field (LF) NMR spectra of hydrogels.

Figure S11. High-resolution solid-state 13C MAS NMR spectra of hydrogels.

Figure S12. Tensile strength, modulus, tensile strain, and toughness of hydrogels.

Figure S13. Photograph showing a thin strip of the specimen can lift a weight of 12 kg.

Figure S14. The water content of hydrogels.

Figure S15. Tensile and compressive stress-strain curves of hydrogels with 90% and 70% water content.

Figure S16. Tensile and compressive properties of the PVA/CNF-Salting out hydrogel in different directions.

Figure S17. Photographs of hydrogels before and after being compressed to 95% strain.

Figure S18. Comparisons of compressive strength and modulus of hydrogels**.**

Figure S19. Cyclic tensile properties of the PVA/CNF-Salting out hydrogel.

Figure S20. Cyclic compressive properties of the PVA/CNF-Salting out hydrogel.

Figure S21. Hysteresis energy and maximum stress of cyclic tensile tests of hydrogels at a fixed strain of 1,000%.

Figure S22. Hysteresis energy and maximum stress of cyclic compressive tests of hydrogels at a fixed strain of 80%.

Figure S23. Tear resistance of hydrogels.

Figure S24. Pure shear testing of hydrogels.

Figure S25. The FEA nephogram of the stress distribution inside hydrogels during crack propagation.

Figure S26. Cyclic tensile stress curve (cycles 1−3,000) of the notched PVA/CNF-Salting out hydrogel at different strains.

Figure S27. Fatigue resistance of the PVA/CNF-Salting out hydrogel.

Figure S28. Random alignment behavior of the PVA hydrogel even during stretching.

Figure S29. Network structure of the PVA/CNF hydrogel during stretching.

Figure S30. Network structure of the PVA-Salting out hydrogel during stretching.

Figure S31. Representative SAXS profiles of hydrogels during stretching.

Figure S32. Binding energy of different molecules.

Figure S33. Schematic diagram of the CNF enhancement effect assisted with salt.

Figure S34. Total radius of gyration and end-to-end distance of PVA and CNF in water.

Figure S35. Comparison of rigidity between PVA and CNF.

Figure S36. Simulation snapshots of PVA/CNF hydrogels with different water content.

Figure S37. Simulation snapshots of PVA hydrogels with different water content.

Figure S38. Number of H-bonds of the hydrogels containing different water content.

Figure S39. Effect of CNF on the load transfer behaviors.

Figure S40. Freezing resistance properties of hydrogels.

Figure S41. Photographs of hydrogels at low temperature.

Figure S42. Electrochemical AC impedance spectra (IMP) of hydrogels.

Figure S43. Electrochemical properties of hydrogels.

Figure S44. Photographs of the PVA/CNF-Salting out hydrogel as ionic conductor lighting up LED lamps.

Figure S45. Photographs of the PVA/CNF-Salting out hydrogel lighting up LED lamps under different deformations at −10 °C.

Figure S46. Advanced the PVA/CNF-Salting out hydrogel-based sensor in monitoring human joints and physiological signals.

Supplemental Tables

Table S1. Summary of the four types of produced hydrogels.

Table S2. Summary of strong and tough hydrogels.

Table S3. Summary of stretchable and tough hydrogels.

Table S4. Summary of tough and fatigue-resistant hydrogels.

Supplemental References

Supplemental Materials and Methods

Materials

Poly(vinyl alcohol) (PVA) [weight-average molecular weight (Mw of 89,000~98,000 and degree of hydrolysis of 99.0%)], sodium citrate (NaCitr, AR, 98%), sodium hydroxide (NaOH, AR, 96%), and (2,2,6,6-tetramethylpiperidin-1-yl)oxidanyl (TEMPO, AR, >97%) were obtained from Aladdin. Sodium hypochlorite solution (NaClO, available chlorine content is 13%~16%), sodium chlorite ($NaClO_2$, 80%), and sodium bromide (NaBr, AR, 99%) were gained from Macklin. Poplar powder was purchased from Qingdao Ruilibo International Trade Co., Ltd. Biomass cellulose was obtained by soaking poplar powder in an alkaline solution to remove hemicellulose, lignin, and other components according to our previous work.[1] Deionized (DI) water obtained from a laboratory water purifying system was used throughout the experiments. Unless otherwise stated, all the chemicals in this work were used as received and directly used without further purification.

Tensile and compressive testing

Tensile and compressive measurements were performed on hydrogel specimens using a SUNS UTM6503 universal testing machine equipped with 100-N and 5,000-N loading cells. The width and thickness of each individual rectangular hydrogel specimen, measured with a caliper, were typically around 20 and 2 mm, respectively, for regular tensile testing. Tensile stress-strain curves were obtained at a continuous tensile speed of 10 mm min^{-1}. For the compressive test, cylinder-shaped hydrogel specimens with a height of 15 mm and a diameter of 10 mm were existed on the center of the lower flat plate and compressed by a constant loading rate of test of 5 mm min^{-1}. Cyclic tensile and compressive tests were performed by conducting subsequent trials immediately after initial loading. Three hydrogel specimens were tested for each condition and the average results were recorded.

True stress

The corrected true tensile strength of the hydrogels is more representative of the actual stress, given the shrinkage of the cross-sectional area of the hydrogels, especially when stretched beyond 5,000%. We therefore employed a classical broad uniaxial deformation approach for polymer networks,[2] and it has been demonstrated that the stress-strain relation can be described

by a constitutive equation relating the true stress (σ_{true}) with the elongation ratio (λ) as following:

$$\sigma_{true} = \frac{G}{3}(\lambda^2 - \lambda^{-1})\left(1 + 2\left(1 - \frac{\beta(\lambda^2 + 2/\lambda)}{3}\right)^{-2}\right) \quad (1)$$

where G is the rigid modulus of the hydrogels, and $\beta = \left\langle R_0^2 \right\rangle / R_{max}^2$ is the ratio of the mean-square average end-to-end distance of the strand in the hydrogel networks to the square of the end-to-end distance of the fully stretched strand R_{max}^2.

Water content measurements

Excess water on the surface of the hydrogel specimens was wiped off before they were continuously snap-frozen with liquid nitrogen followed by a freeze-drying process. The water content of the hydrogels was measured by comparing their weights before and after freeze-drying, and the water content (W) can be obtained by the following formula:

$$W(\%) = \frac{m_{wet} - m_{dry}}{m_{wet}} \quad (2)$$

where m_{wet} and m_{dry} are the weight of the hydrogels before and after freeze-drying in equilibrium, respectively.

Trouser-tearing tests

Trouser-tearing tests were carried out to measure the tearing fracture energy of hydrogels. The tests were performed using a tensile tester (UTM6503, SUNS) equipped with a 100-N loading cell. The hydrogel specimen was prepared with 50 mm of length, 20 mm of width (W), and about 1 mm of thickness (h). An initial crack of 25 mm was made in the middle of the hydrogel specimen along the length direction with a sharp blade. One leg of the hydrogel specimen was fixed on the base and another one on the crosshead, which is pulled upward at a speed of 50 mm min^{-1}. After testing, the tearing force-displacement curves were obtained to calculate the tearing energy (T) specimens by the following equation:[3,4]

$$T = \frac{2F}{h} \quad (3)$$

where F is the tearing force at the steady state during tearing, h is the thickness of the hydrogel specimen.

Pure shear tests

For fracture energy testing, pure shear tests were performed at a stretching rate of 10 mm min^{-1}, the rectangular specimens are 20 mm wide, 2 mm thick, and a crack width of 5 mm. The critical stretch (ε_c) for unstable propagation of the crack hydrogel specimens was obtained from the stretch at the break. The pairing unnotched hydrogel specimens were subsequently stretched until $\varepsilon = \varepsilon_c$. After testing, the fracture energy (Γ) was obtained by the following equation:[5]

$$\Gamma = H\int_{\varepsilon=0}^{\varepsilon=\varepsilon_c} \sigma \mathrm{d}\varepsilon \tag{4}$$

where σ is the stress of the unnotched hydrogel specimen under tension, H is the gauge length.

Fatigue tests

To validate the fatigue threshold of our hydrogels, we employed the simple single-edge notch method at ambient conditions (25 °C, 70 ± 1 RH%).[6] The used rectangular specimen had a width of 20 mm and a thickness of 2 mm with a notch of 1/5 the width. The notched hydrogel specimens were subjected to continuous cyclic tensile tests at a speed of 500 min mm^{-1} without relaxation time. A digital camera (EOS 6D, Cannon) was employed to record the crack propagation of the hydrogel samples. The energy release rate (G) of the notched specimens under the N^{th} cycle with a maximal applied strain of ε_m was calculated as follows:

$$G(\varepsilon_m, N) = 2k(\varepsilon_m)\cdot c(N)\cdot W(\varepsilon_m, N) \tag{5}$$

Where $k(\varepsilon_m)$ is a slowly varying function of the applied strain, determined empirically by $k(\varepsilon_m) = 3/\sqrt{\varepsilon_m + 1}$, $c(N)$ is the propagation length, and $W(\varepsilon_m, N)$ is the strain energy density of the parallel dimensional unnotched hydrogel specimens stretched to the same applied strain ε_m.

Freeze resistance tests

The storage and loss modulus of the hydrogel specimens were obtained by a TA Instruments DMA 850 in tensile mode at a constant frequency of 1 Hz at a cooling rate of 5 °C min^{-1}. The freezing point of the hydrogel specimens was performed using a TA Instruments DSC 8500 with a cooling speed of 5 °C min^{-1} by cooling the samples from 25 to −30 °C.

Electrochemical performance tests

The electrochemical properties of the hydrogels were tested using a Chenhua (CHI 760E)

electrochemical workstation. The real-time resistance of the hydrogel-based sensor under tension and bending was recorded by a Keithley digital multimeter (DMM 7510). The real-time voltage and current data of the hydrogel-based triboelectric nanogenerator were collected utilizing a high-resistance electrometer (Keithley 6514). The data of impedances were obtained by electrochemical AC impedance spectroscopy (IMP) method at ambient and low temperature, and the frequency of all hydrogel specimens was swept from 10^{-1} to 10^{5}. The formula for calculating the ionic conductivity (σ_c) of the hydrogel was as follows:

$$\sigma_c = \frac{L}{RA} \tag{6}$$

where L is the distance between the two electrodes, R is the electrical resistance of the hydrogel specimen and A is the cross-sectional area of the hydrogel specimen.

Supplemental Figures

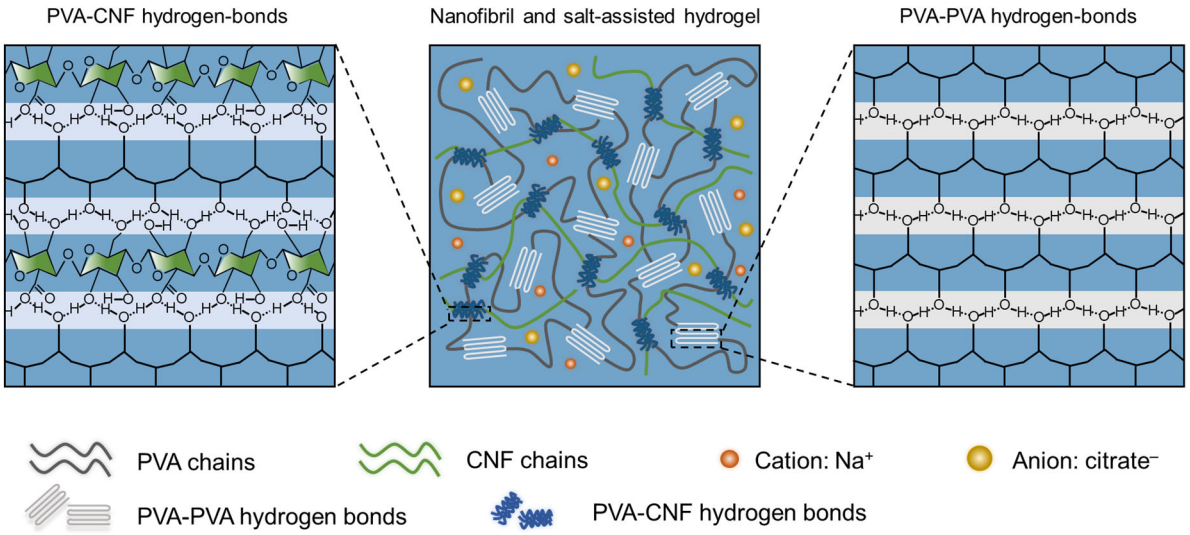

Figure S1. Design of nanofibril and salt-assisted hydrogels.

The nanofibril and salt-assisted hydrogel is obtained using CNFs and salting-out treatment, which mainly contains two types of H-bonds crosslinked networks, that is, PVA-CNF H-bonds and PVA-PVA H-bonds.

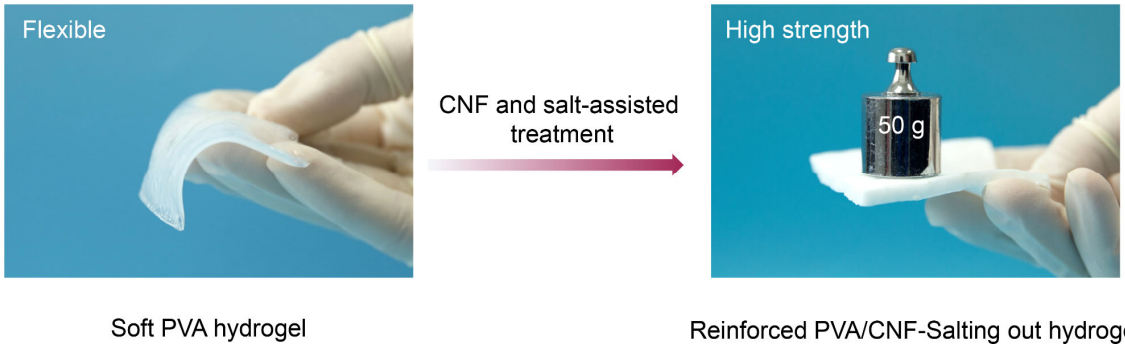

Figure S2. Photographs of the PVA hydrogel and PVA/CNF-Salting out hydrogel.

The PVA hydrogel exhibits flexibility and softness due to its inherent relatively loose network structure. Encouragingly, by coupling of CNFs and salt-assisted treatment, the obtained reinforced PVA/CNF-Salting out hydrogel is able to easily support a weight of 50 g, showing high strength and stiffness. This can be explained by that the strong H-bond interaction between the PVA and CNF chains that enables a robust network architecture to bear the force.

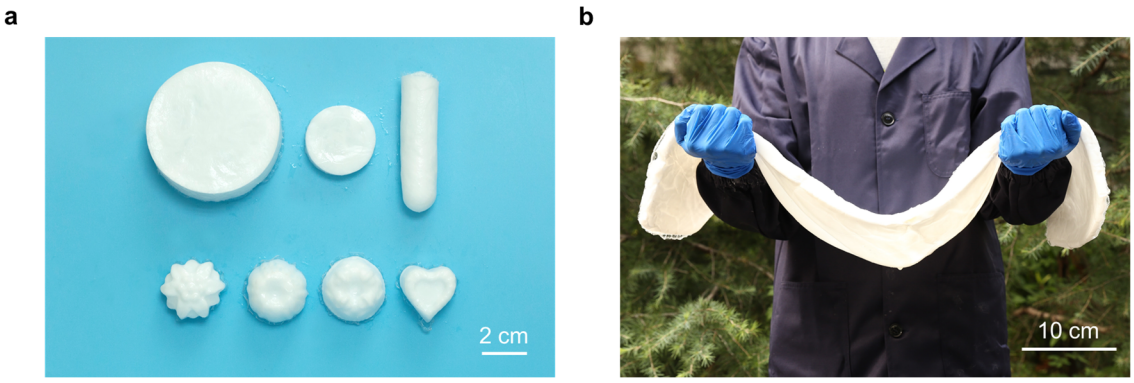

Figure S3. Photographs of PVA/CNF-Salting out hydrogels with different shapes (**a**) and large scales (**b**) (100 cm by 25 cm by 1 cm).

Benefiting from the facile fabrication process, the traditional anisotropic hydrogels prepared by freeze-casting and ice-templating methods are freed from the confinement of complicate forming equipment, which can be realized into arbitrary modes, such as the shape of cylinders, hearts, and stars etc. Furthermore, a large-scale production potential is enabled to apply to real-world requirements.

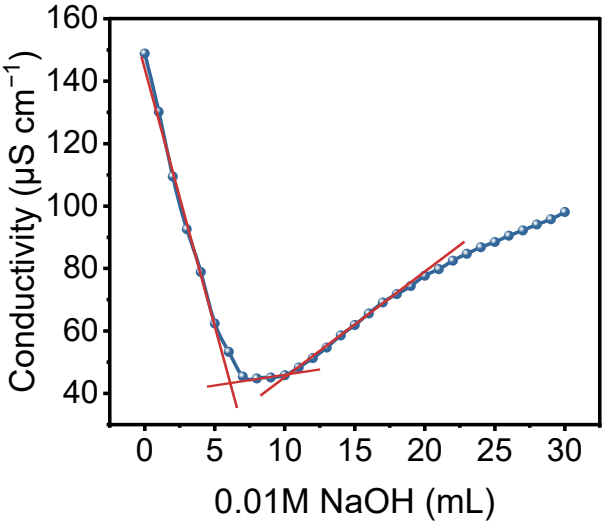

Figure S4. Typical conductometric titration curve of our obtained CNFs for determining the surface charge density.

Surface carboxylate groups content of our prepared CNFs for hydrogels is calculated as 1.28 mmol g^{-1}.

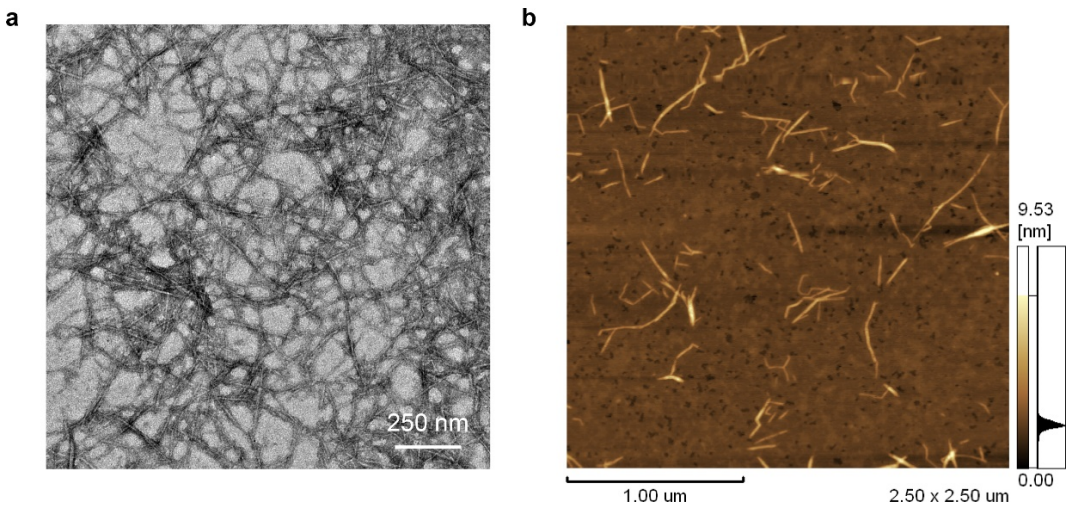

Figure S5. Surface morphology analysis of our obtained CNFs. TEM (**a**) and AFM (**b**) images of our obtained CNFs.

TEM and AFM images showing the average diameter and length of the fabricated CNFs are 8.3 ± 1.3 nm and 200−800 nm, respectively.

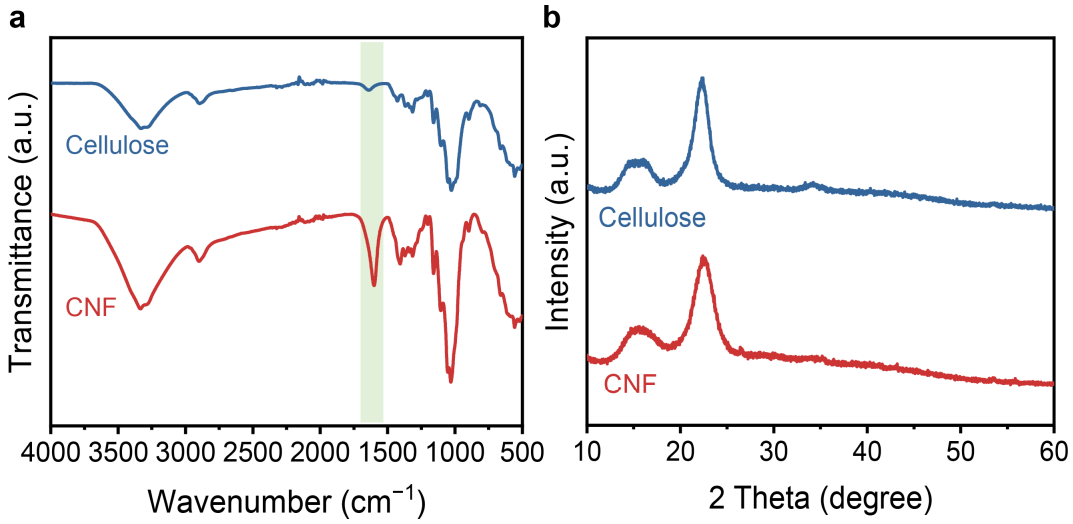

Figure S6. Structural characterizations of our obtained CNFs. FTIR curves (**a**) and XRD patterns (**b**) of CNFs.

The strong and sharp peak at 1,608 cm^{-1} in the FTIR curve of the CNF is attributed to the stretching vibration of the carbonyl peak in the carboxyl group, indicating the successful preparation of CNFs. From the XRD pattern, we can find that, compared with the cellulose, the characteristic diffraction peaks of the CNF have no visible transformation and attenuation, which proves that the crystalline structure of the CNF is retained as the cellulose I-type structure.

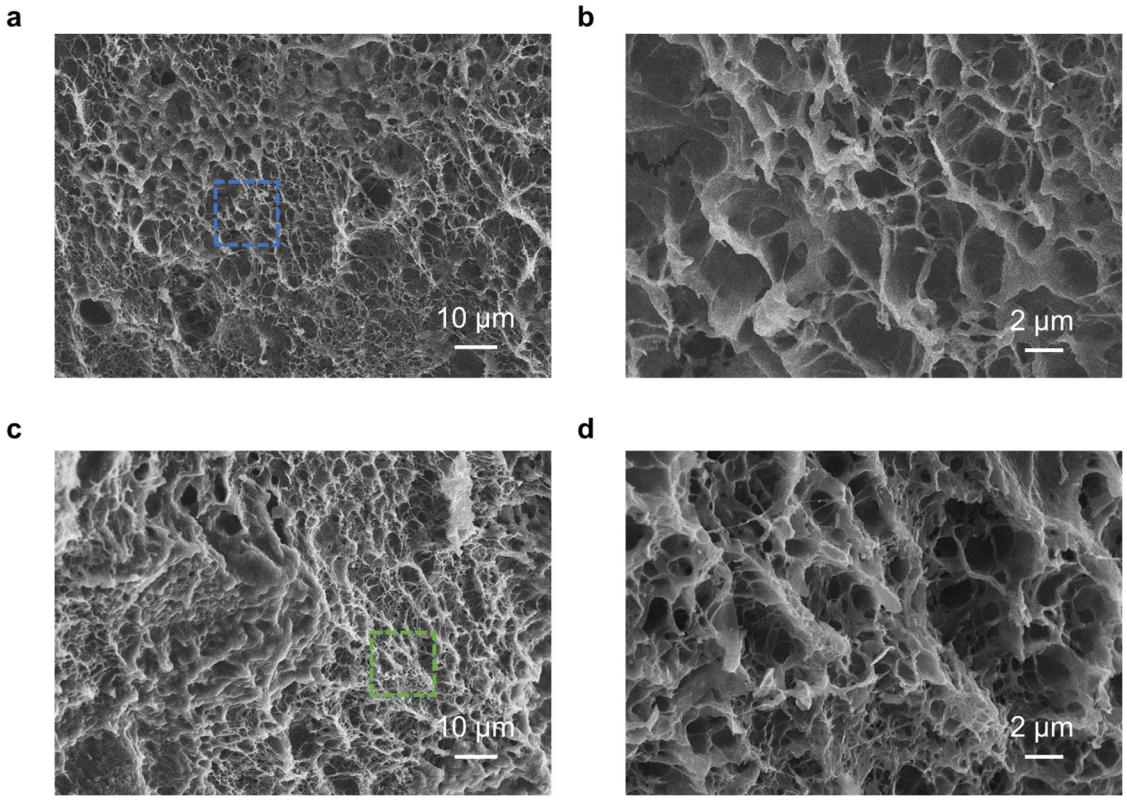

Figure S7. Micromorphology analysis of the PVA hydrogel and PVA/CNF-Salting out hydrogel. a, b SEM images of the PVA hydrogel at high (**a**) and low (**b**) magnifications. **c, d** SEM images of the PVA/CNF-Salting out hydrogel at high (**c**) and low (**d**) magnifications.

SEM images confirm the fact that the PVA hydrogel exhibits large microporous structures due to the infirm H-bond crosslinked network. Conversely, the PVA/CNF-Salting out hydrogel presents densely compact pores on account of the attachment of CNFs to the PVA chains, which is attributed to the strong H-bond interaction between the PVA and CNF chains contributing to the interwove robust architecture.

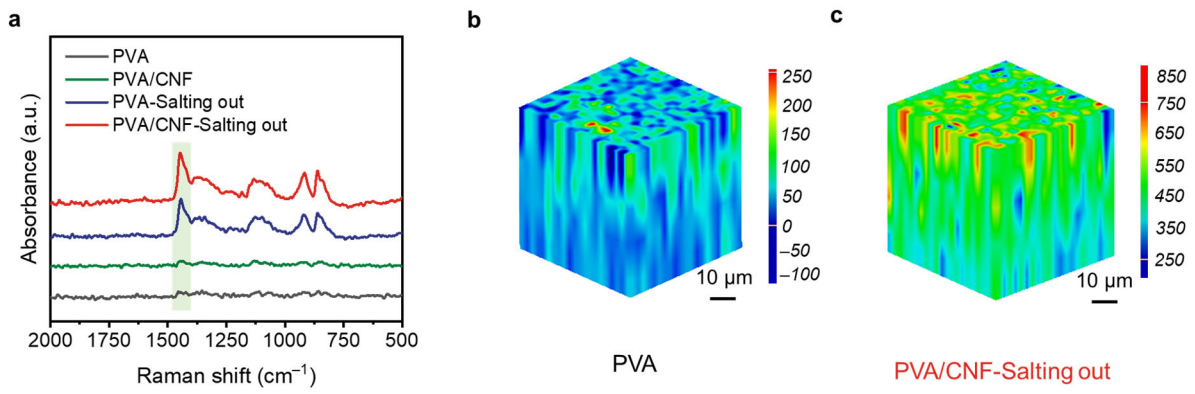

Figure S8. a, Raman spectra of different hydrogels. **b, c** Reconstructed 2D Raman images of the PVA-Salting out hydrogel (**b**) and PVA/CNF hydrogel (**c**).

The intensity of the peak at 1,475 cm^{-1} belonging to the CH−OH bending vibration represents the degree of H-bond crosslinking in the hydrogel (Figure S8a). We can find that the characteristic peak intensity of the PVA/CNF-Salting out hydrogel is much higher than that of the PVA hydrogel, indicating that it has the intense H-bond crosslinking domains. This is consistent with the results of the reconstructed 3D Raman images. Particularly, the PVA/CNF-Salting out hydrogel displays relatively high H-bond crosslinking domains, which is opposite to that of the PVA hydrogel (Figure S8b, c).

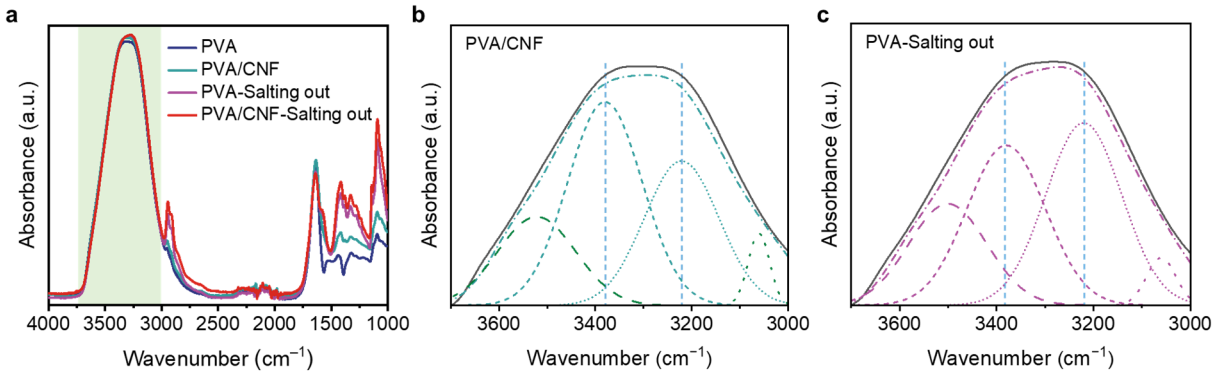

Figure S9. a, ATR-FTIR spectra of different hydrogels. **b, c** The ratios of the peaks located at 3,210 and 3,370 cm^{-1} of the PVA/CNF hydrogel (**b**) and PVA-Salting out hydrogel (**c**).

The region of 3,000−3,400 cm^{-1} in the ATR-FTIR curve is ascribed to a broad −OH stretching vibration, which can be deconvoluted into two subpeaks around 3,210 and 3,370 cm^{-1}, corresponding to the H-bond of PVA-CNF/PVA-PVA and PVA-water, respectively (Figure S9a). We found that the PVA-Salting out hydrogel exhibits intenser the H-bond of PVA-CNF/PVA-PVA than the PVA/CNF hydrogel, which proves that the operation of salting out treatment presents a more favorable positive effect on the formation to the H-bond between polymer chains in the hydrogel (Figure S9b, c).

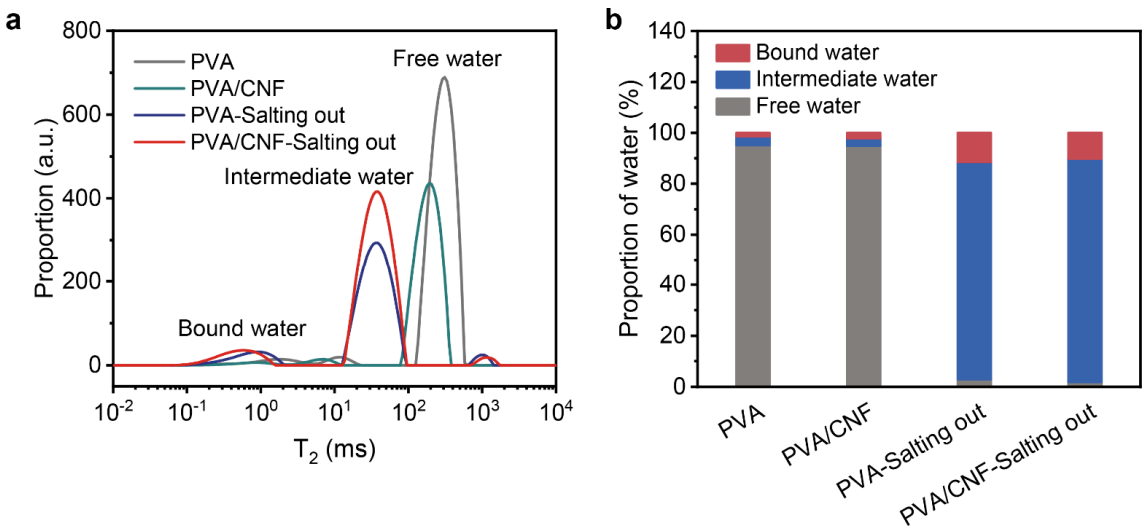

Figure S10. a, Low-field (LF) NMR spectra of different hydrogels. **b,** The content distributions of the three types of water in different hydrogels are calculated from the integrated areas of the corresponding characteristic peaks in the LF curves.

The LF test results show that there are mainly three types of water in the hydrogels, that is, free water, immediate water, and bound water (Figure S10a). Obviously, when the PVA hydrogel is treated by CNFs with salt assistance, the obtained PVA/CNF-Salting out hydrogel presents a significant reduction in free water, which is on account of the compact H-bond crosslinked network between the PVA and CNF chains restricts the free movement of water, thereby promoting the formation of more immediate water (Figure S10b).

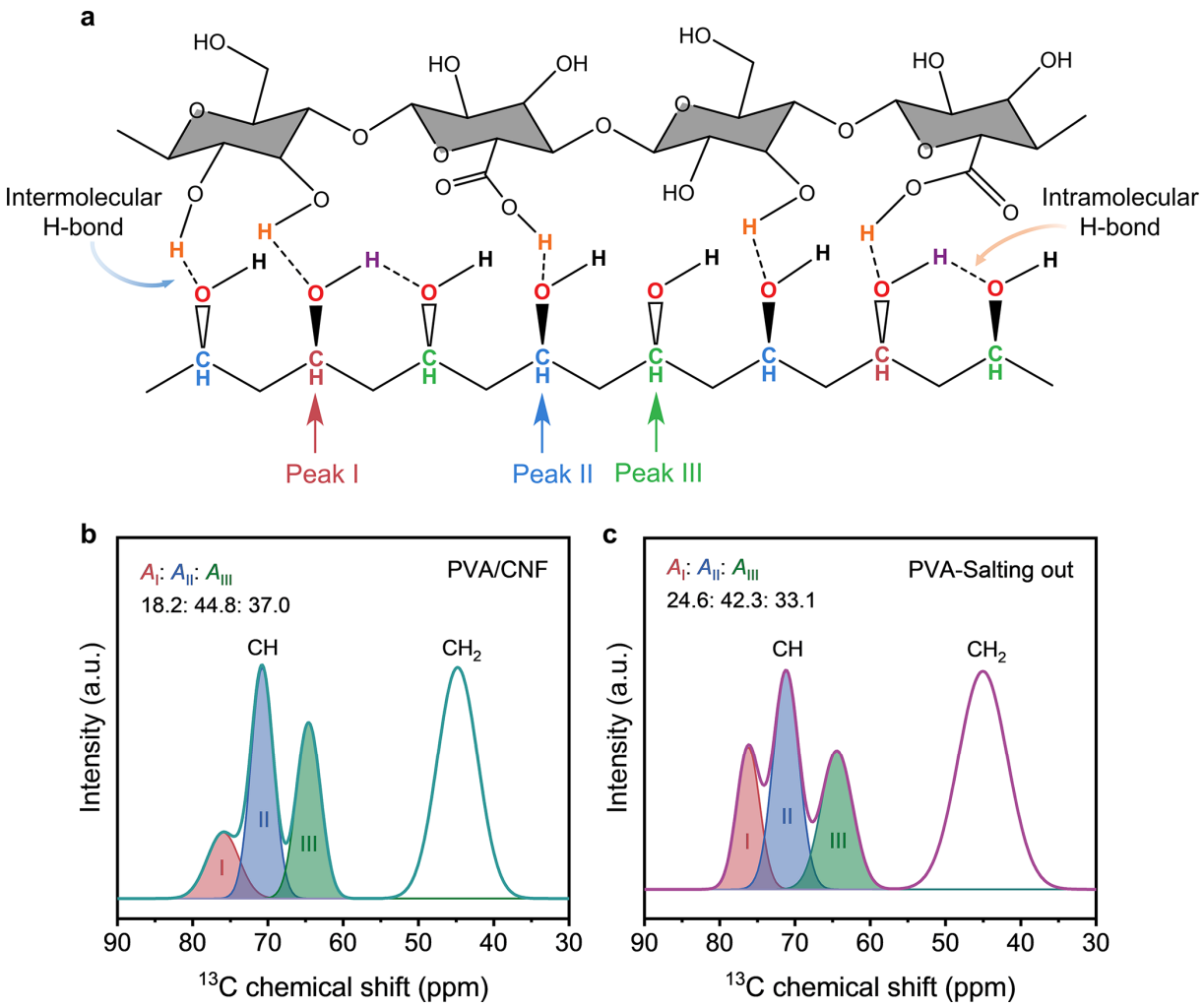

Figure S11. a, Schematic representation for inter- and intramolecular H-bond interactions between the PVA and CNF chains. **b, c** High-resolution solid-state ^{13}C MAS NMR spectra of the PVA/CNF hydrogel (**b**) and PVA-Salting out hydrogel (**c**).

In addition to the characteristic peak of CH_2 at 44.6 ppm, the chemical shift peak of the CH group is split into three bands (I, II, and III) localized at around 76.1, 70.9, and 64.5 ppm corresponded to the inter- and intra-molecular H-bonded CH (I and II) and free CH (III), respectively (Figure S11a). Figure S11b and c show the change in the ratio of inter- and intra-molecular H-bonds, as well as free CH in hydrogels. We found that the proportion of H-bonds for the PVA-Salting out is higher than that of the PVA/CNF hydrogel, which is attributed to the formation of more strong H-bonds among PVA chains with salt assistance.

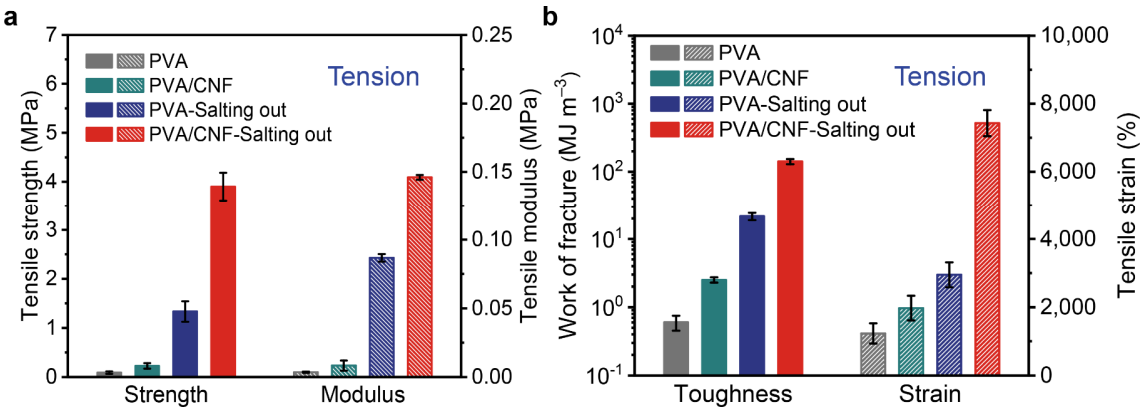

Figure S12. a, b Comparisons of tensile strength and modulus (**a**) and tensile strain and toughness (**b**) of the four types of hydrogels. Error bars show the standard deviation from three independent specimens.

Benefiting from the stretch-induced in situ self-assembly based on the strong H-bond interactions between PVA and CNF chains on supramolecular chemistry, the PVA/CNF-Salting out hydrogel presents excellent stretchable performance. Specifically, for the PVA/CNF-Salting out hydrogel, exhibiting tensile strength of 3.9 MPa, tensile modulus of 0.15 MPa, tensile strain of 7,430%, and toughness of 141.4 MJ m^{-3}, which is 43.3 times, 50 times, 6.1 times, and 234.7 times that of the corresponding the PVA hydrogel, respectively, implying its comprehensively superior mechanical properties.

Figure S13. Photograph showing a thin strip of the specimen can successfully lift a weight of 12 kg that is 2,400-fold its own weight.

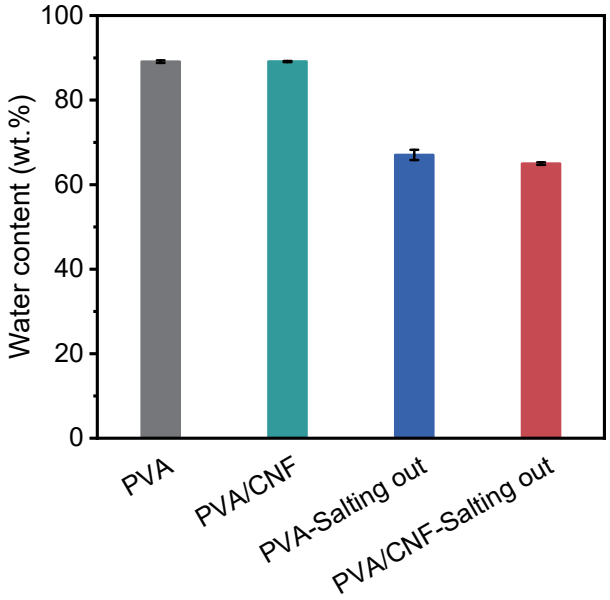

Figure S14. The water content of four types of hydrogels. Error bars show the standard deviation from three independent specimens.

The water content of the obtained PVA/CNF-Salting out hydrogel after CNF and salt-assisted enhancement treatment is around 70%, which is attributed to the ion-specific effect, that is, the salting-out operation makes the free water in the network move outward. It is worth noting that despite the decrease in water content, it still maintains the inherent feature of high water content of polymer hydrogels, which is rare in highly strong tough hydrogels.

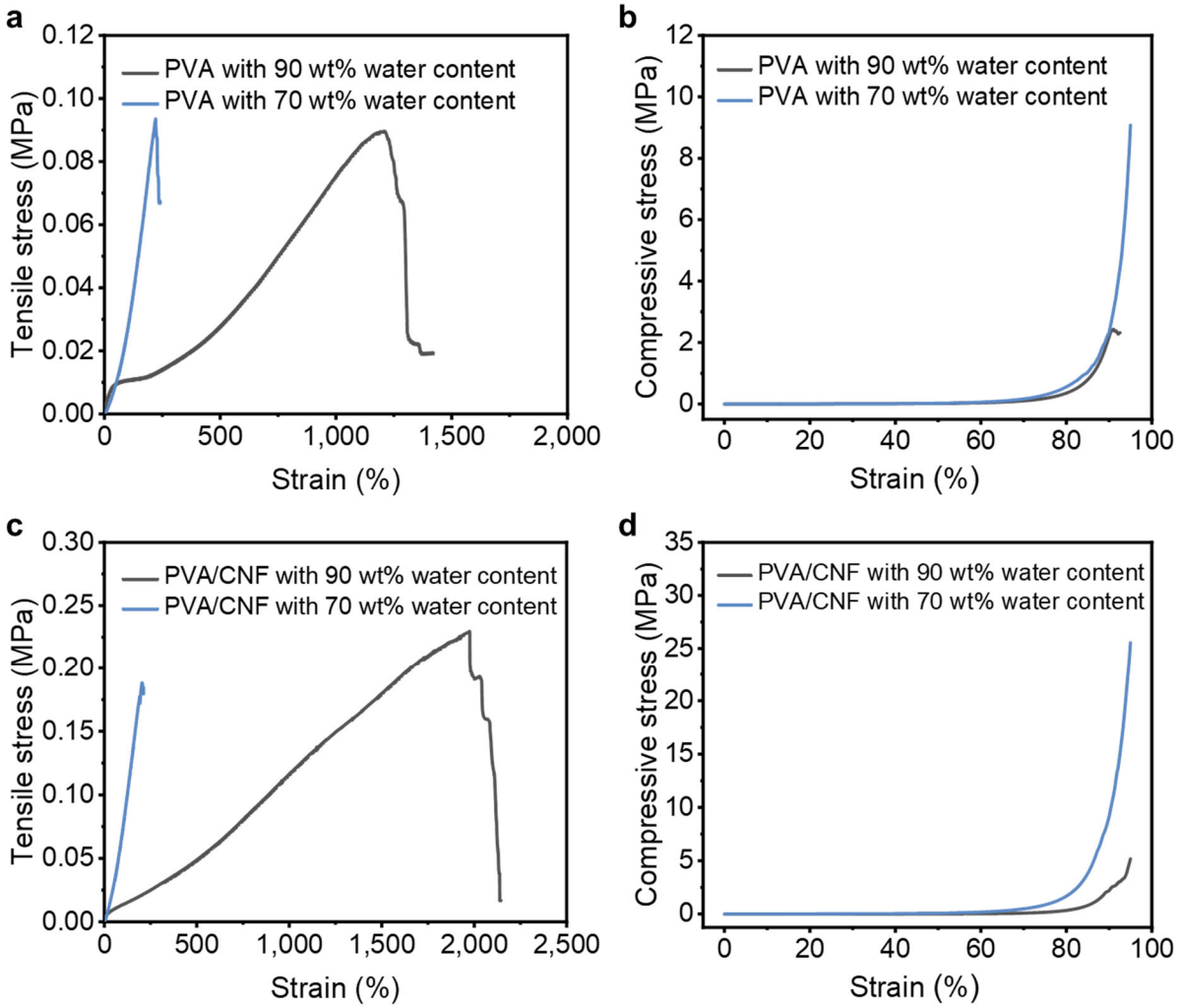

Figure S15. a,b Tensile (**a**) and compressive (**b**) stress-strain curves of the PVA hydrogel at 90% and 70% water content. **c,d** Tensile (**c**) and compressive (**d**) stress-strain curves of the PVA/CNF hydrogel at 90% and 70% water content.

The tensile and compressive behaviors of the PVA hydrogel and the PVA/CNF hydrogel are consistent with those of conventional hydrogels, that is, with decreasing water content in the hydrogel system, an increased tensile and compressive strength yet decreased fracture strain are exhibited. However, at a water content of 70%, the strength and strain both under tension and compression present inferiority compared to the corresponding PVA-Salting out hydrogel and PVA/CNF-Salting out hydrogel.

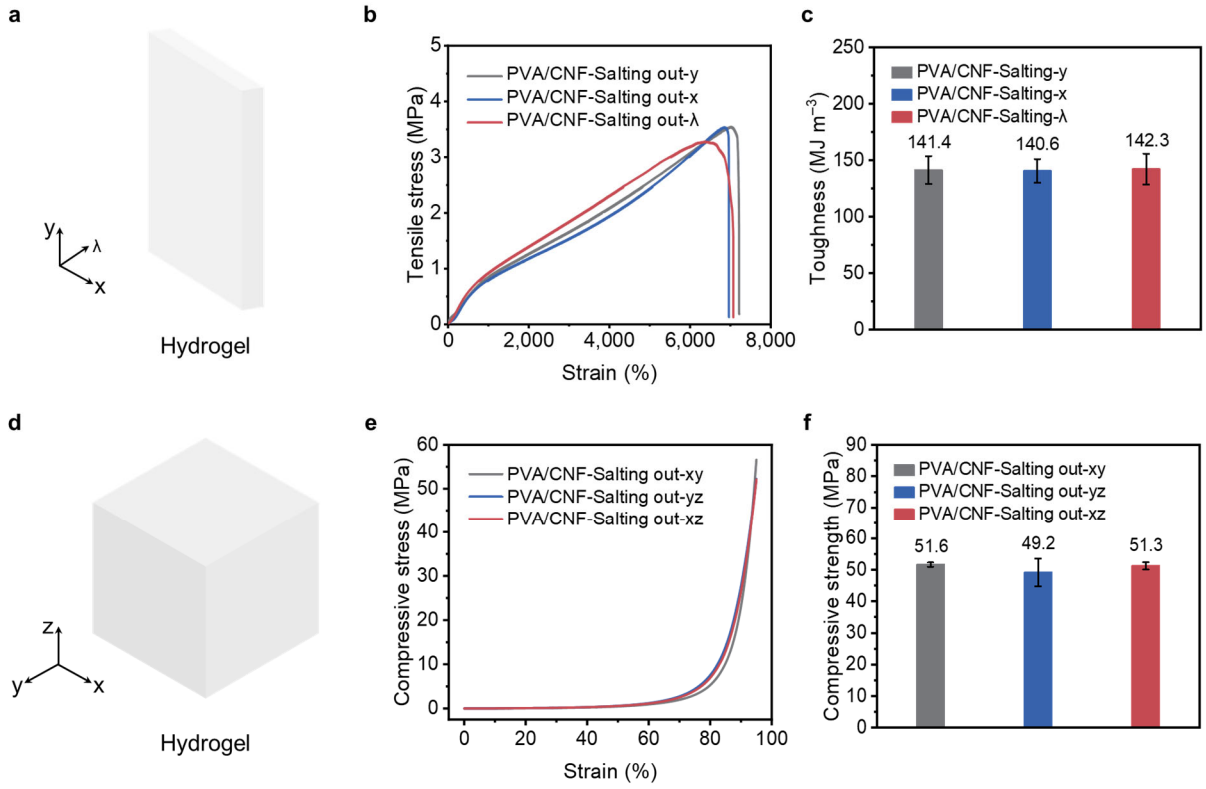

Figure S16. a, Schematic illustration of the PVA/CNF-Salting out hydrogel being stretched along different directions. **b, c** Tensile stress-strain curves (**b**) and corresponding toughness (**c**) of the PVA/CNF-Salting out hydrogel in different directions. **d,** Schematic illustration of the PVA/CNF-Salting out hydrogel being compressed along different directions. **e, f** Compressive stress-strain curves (**e**) and corresponding compressive strength (**f**) of the PVA/CNF-Salting out hydrogel in different directions. Error bars show the standard deviation from three independent specimens.

Benefiting from the isotropic homogeneous robust H-bond crosslinked network from the PVA/CNF-Salting out hydrogel, when stretched in three directions, the tensile stress-strain curves are close to coincide, and the corresponding toughness is not without obvious differences, indicating that it has excellent superstretchability despite the force loading at varied angles. This impressive result demonstrates its verifiable, stable, and trustworthy mechanical performances. As we expected, similar to the isotropic tensile properties, the PVA/CNF-Salting out hydrogel also presents stable, undifferentiated compressive mechanical properties at varied directions, further demonstrating the homogeneous and steady mechanical properties facilitated by the intense isotropic H-bond crosslinked network.

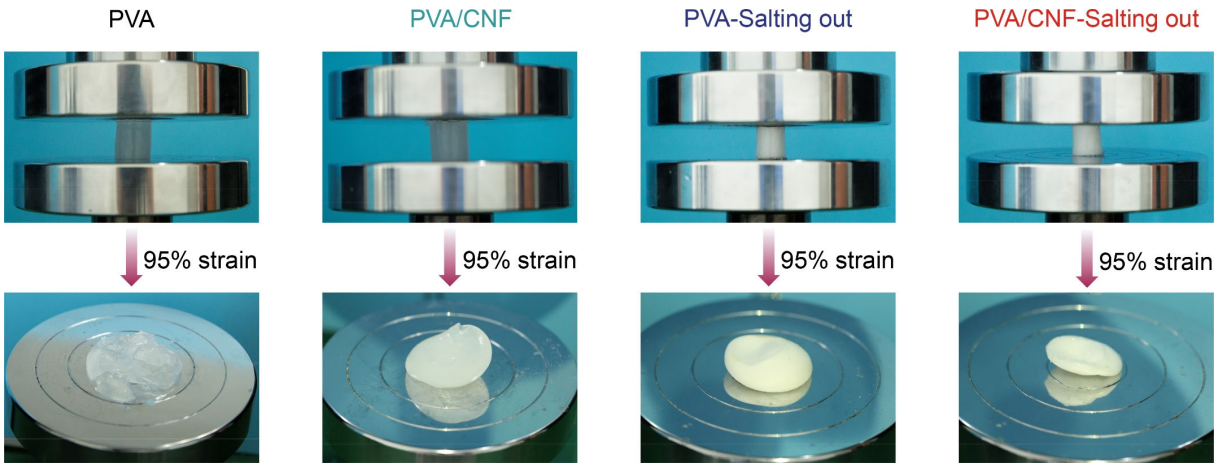

Figure S17. Photographs of hydrogels before and after being compressed to 95% strain.

It is observed that the PVA/CNF-Salting out hydrogels show only a squashed state but no visible fracture after being compressed to an ultimate strain of 95%, while the remaining three hydrogels exist or more or less destroyed. This can be explained by the fact that the presence of a highly compact interwoven H-bonded crosslinked network in the PVA/CNF-Salting out hydrogel facilitates resistance to extrusion even under extreme deformation.

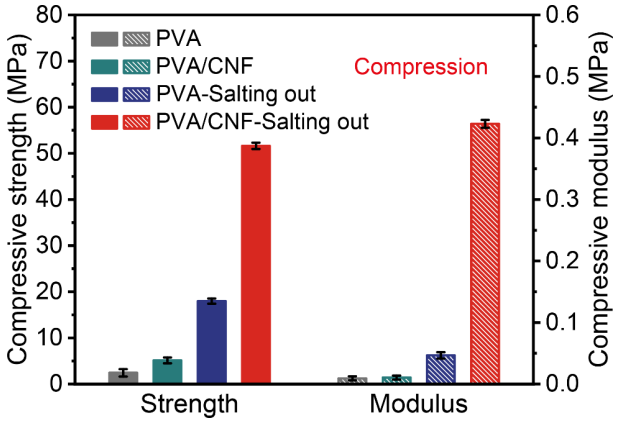

Figure S18. Comparisons of compressive strength and modulus of the four types of hydrogels. Error bars show the standard deviation from three independent specimens.

The maximum stress of the PVA/CNF-Salting out hydrogel is 51.7 MPa at an astonishing strain of 95%, which is 21.4 times that of the pure PVA hydrogel, implying a good indicator of high strength and robustness. Additionally, the compressive modulus of the PVA/CNF-Salting out hydrogel reaches 0.423 MPa, which is an order of magnitude higher than that of the PVA hydrogel (below 0.01 MPa), indicating its strong yet stiff features.

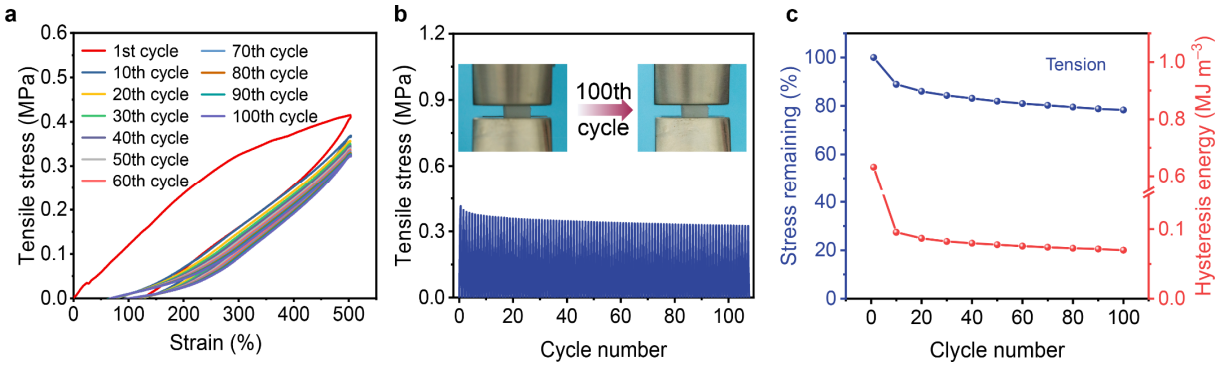

Figure S19. Cyclic tensile properties of the PVA/CNF-Salting out hydrogel. **a,** Multiple loading-unloading curves of the PVA/CNF-Salting out hydrogel. **b,** Tensile stress of the PVA/CNF-Salting out hydrogel at different cycles. **c,** Stress retention and hysteresis energy of the PVA/CNF-Salting out hydrogel at different cycles.

The PVA/CNF-Salting out hydrogel still has good stress retention and energy hysteresis after repeated cyclic stretching, suggesting a positive indicator of the capacity of the durability and strain memory.

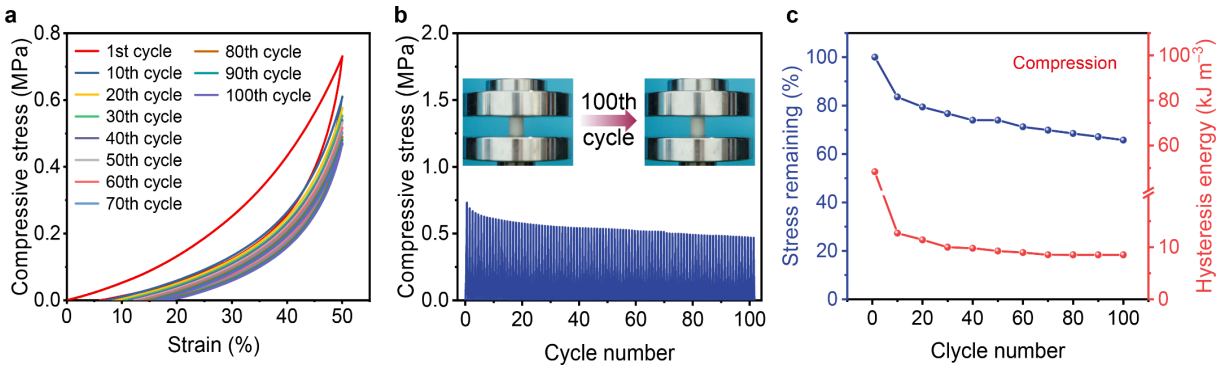

Figure S20. Cyclic compressive properties of the PVA/CNF-Salting out hydrogel. **a,** Multiple loading-unloading curves of the PVA/CNF-Salting out hydrogel. **b,** Compressive stress of the PVA/CNF-Salting out hydrogel at different cycles. **c,** Stress retention and hysteresis energy of the PVA/CNF-Salting out hydrogel at different cycles.

The PVA/CNF-Salting out hydrogel still has good stress retention and energy hysteresis after repeated cyclic compressing, indicating its durability and strain memory.

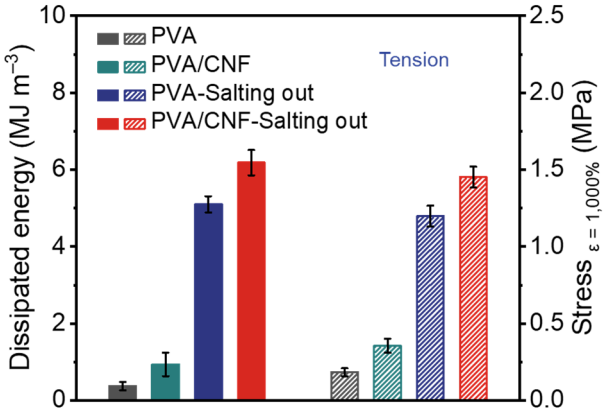

Figure S21. Hysteresis energy and maximum stress of cyclic tensile tests of hydrogels at a fixed strain of 1,000%. Error bars show the standard deviation from three independent specimens.

On account of the destruction of an enormous of sacrificial H-bonds during deformation, the PVA/CNF-Salting out hydrogel exhibits a substantial mechanical hysteresis (up to 6.2 MJ m^{-3}) after unloading, indicating its efficient energy dissipation capability. By contrast, the PVA hydrogel yields negligible energy dissipation of 0.4 MJ m^{-3} as a result of the weak H-bond between PVA chains. Similarly, the stress at a strain of 1,000% display the same trend. These good results all prove that there are a large number of H-bonds in the PVA/CNF-Salting out hydrogel to bear the force.

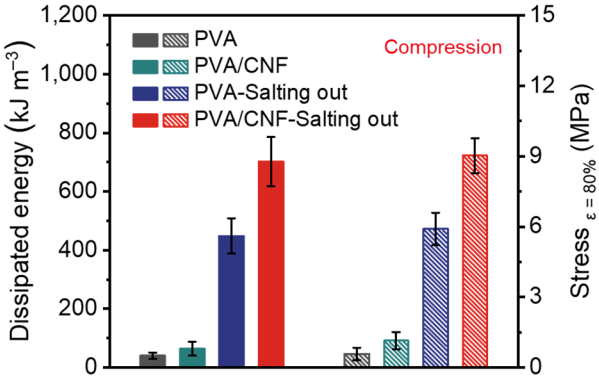

Figure S22. Hysteresis energy and maximum stress of cyclic compressive tests of hydrogels at a fixed strain of 80%. Error bars show the standard deviation from three independent specimens.

Owing to a substantial of sacrificial H-bonds crosslinking, during compression, for the PVA/CNF-Salting out hydrogel, the energy dissipation of 702.02 kJ m^{-3} can be realized by reputing the H-bond, and its maximum stress at a fixed strain of 80% reaches 9.02 MPa, which is 14.8 times higher than that of the PVA hydrogel, further revealing the strong yet tough performances.

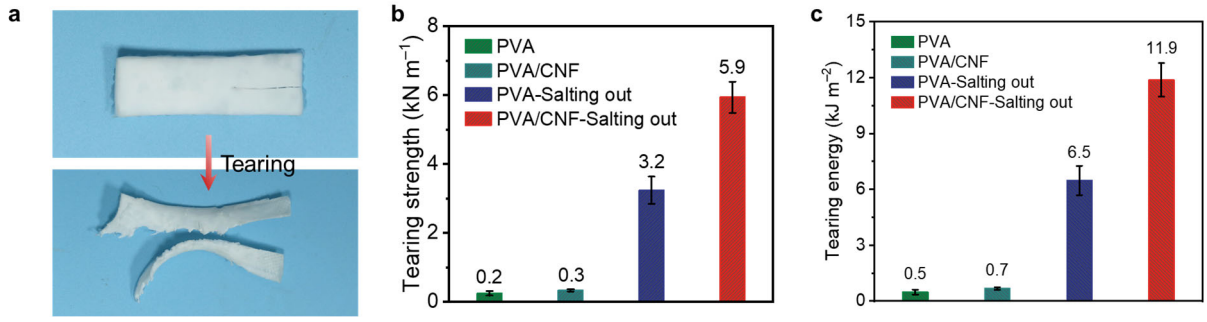

Figure S23. Tear resistance of hydrogels. a, Photographs before and after the PVA/CNF-Salting out hydrogel tearing test **b, c,** Tearing strength (**b**) and tearing energy (**c**) of the hydrogels. Error bars show the standard deviation from three independent specimens.

The results of the trouser-tearing test show that the PVA/CNF-Salting out hydrogel have high tearing force, and the corresponding tearing strength and tearing energy are 5.9 kN m^{-1} and 11.9 kJ m^{-2}, respectively.

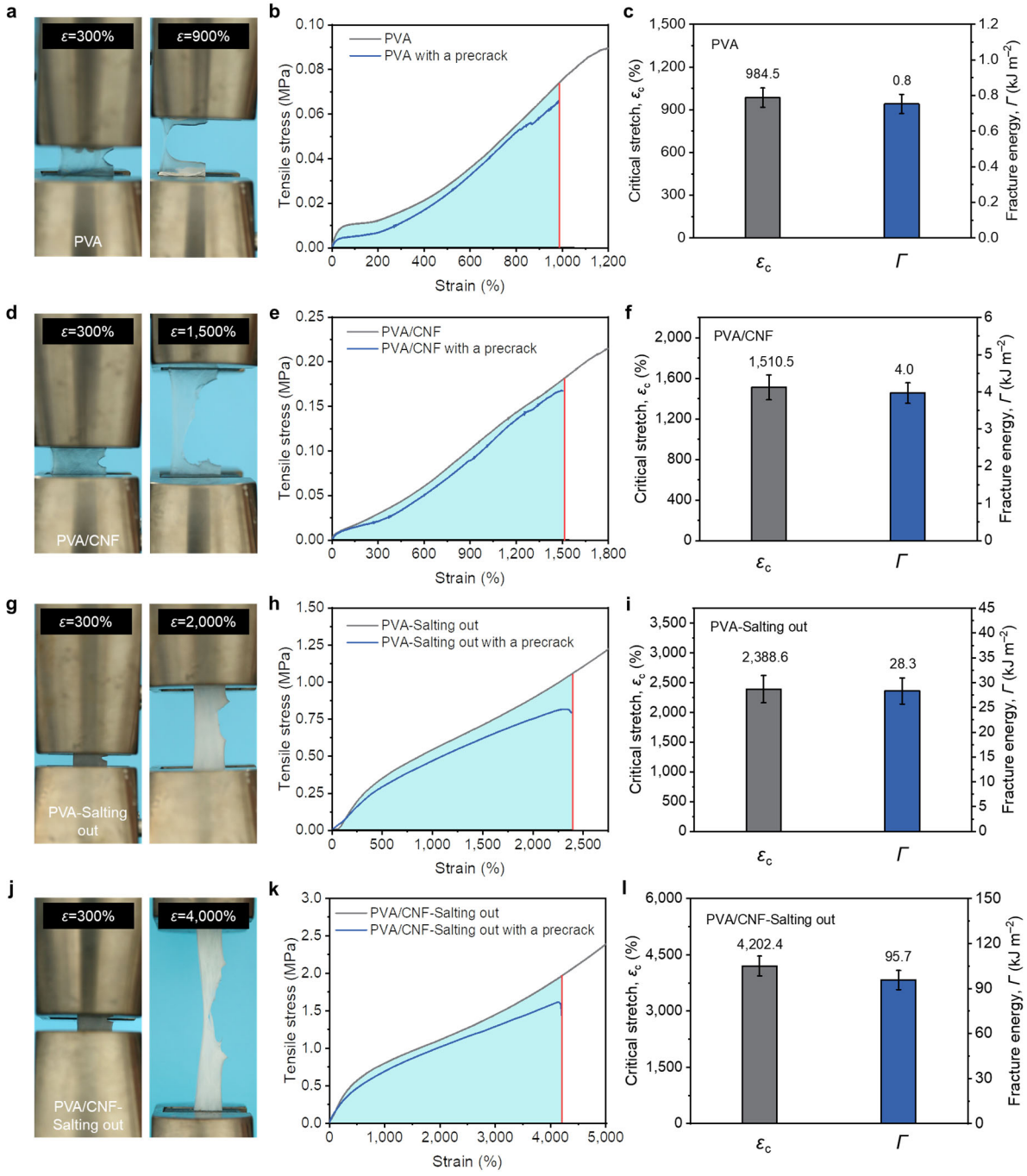

Figure S24. Pure shear testing of hydrogels. a Photographs of pure shear testing of the PVA hydrogel. **b, c** Stress-strain curves (**b**) of notched and unnotched the PVA hydrogel, and the corresponding critical stretch and fracture energy (**c**). Similarly, **d-f** belong to the PVA/CNF hydrogel, **g-i** represent the PVA-Salting out hydrogel, and **j-l** are assigned to the PVA/CNF-Salting out hydrogel. Error bars show the standard deviation from three independent specimens.

The pure shear test results present that the PVA/CNF-Salting out hydrogel has the highest fracture toughness, and its fracture energy is as high as 95.7 kJ m^{-2}, which is two orders of magnitude higher than that of PVA hydrogel, specifically 127.6 times.

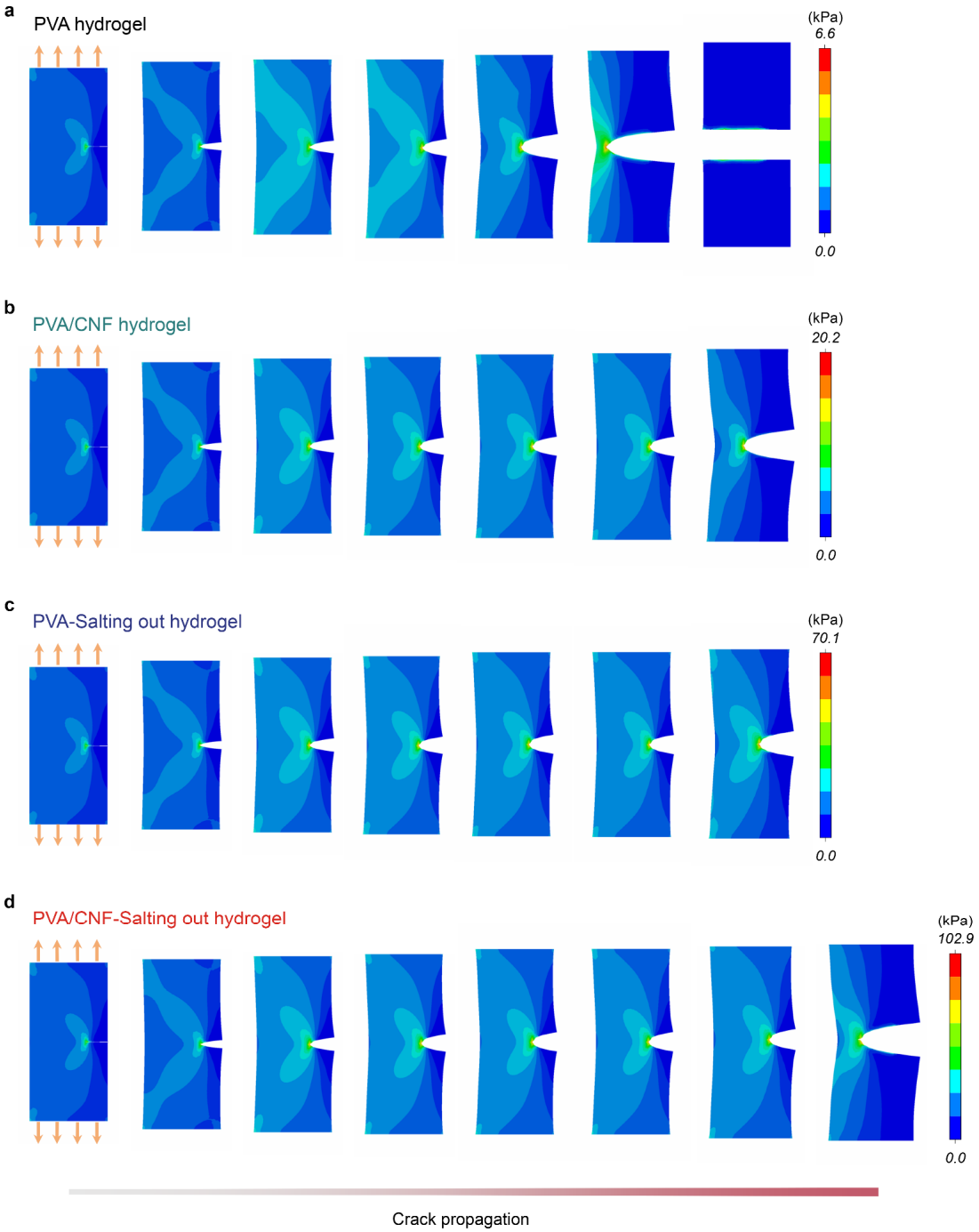

Figure S25. The FEA nephogram of the stress distribution inside the PVA hydrogel (**a**), PVA/CNF hydrogel (**b**), PVA-Salting out hydrogel (**c**), and PVA/CNF-Salting out hydrogel (**d**) during crack propagation. The scale bar from blue to red indicates the stress concentration is from low to high.

The FEA results show that the stress of the PVA/CNF-Salting out hydrogel at the crack propagation site is around 102.9 kPa, significantly higher than its rest part (less than 100 kPa), and also exceeds the other three type of hydrogels as result of the existence of the robust H-bond cross-linked network.

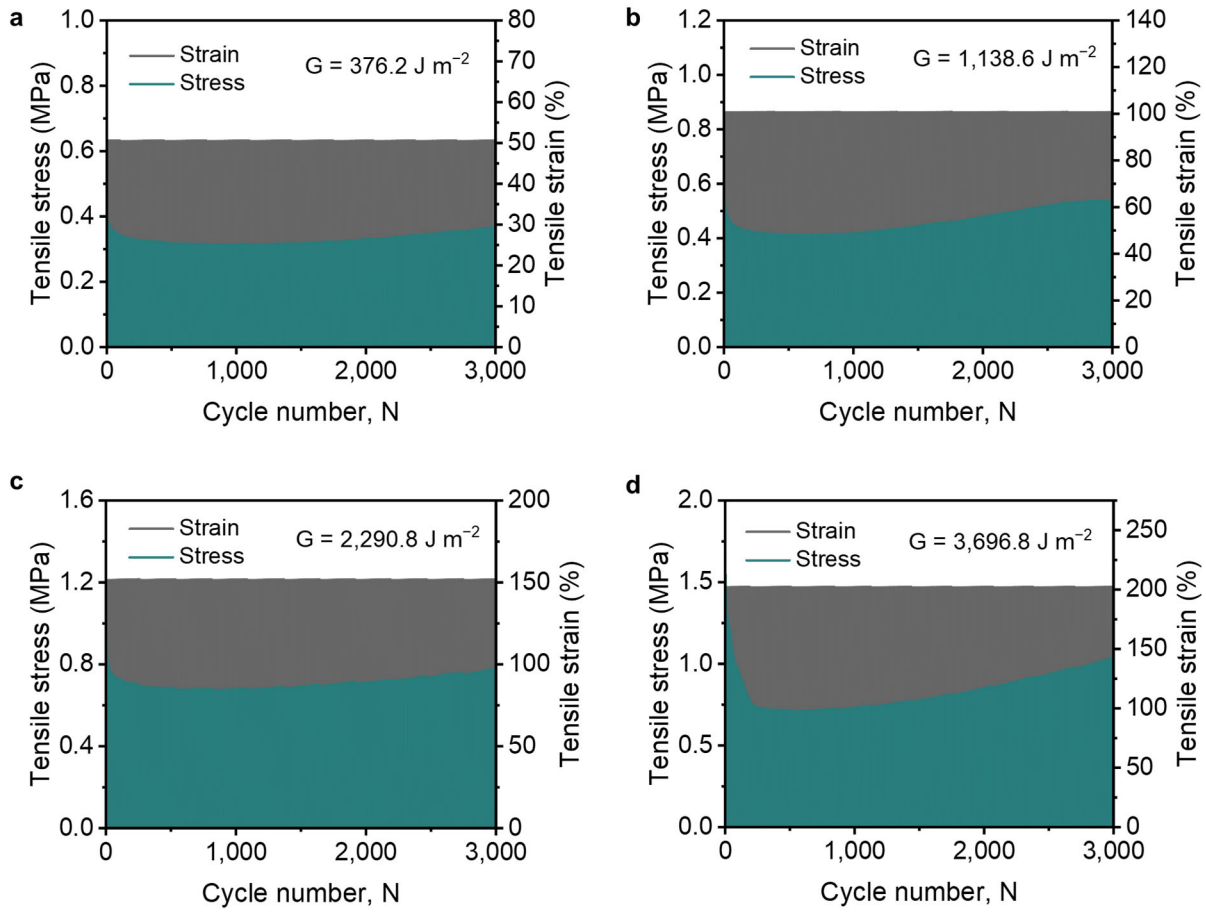

Figure S26. Cyclic tensile stress curve (cycles 1−3,000) of the notched PVA/CNF-Salting out hydrogel at strains of 50% (**a**), 100% (**b**), 150% (**c**), and 200% (**d**).

The maximum stress and strain do not show catastrophic degradation during 3,000 consecutive stretches at fixed strains of 50, 100%, and 150%, indicating that the tensile stress of each deformation is comparable and the hydrogel delivers negligible crack growth. These impressive observations demonstrate the excellent fatigue resistance of the PVA/CNF-Salting out hydrogel. However, at an applied strain of 200%, the maximum stress of the hydrogel exhibits a noticeable decay after around 250 cycles of stretching, which is caused by crack propagation in the notched hydrogel. Notably, a slight increase in the maximum stress is observed at all four strains, which is attributed to the elevated density of the molecular chains due to water evaporation (approximately 5 wt%).

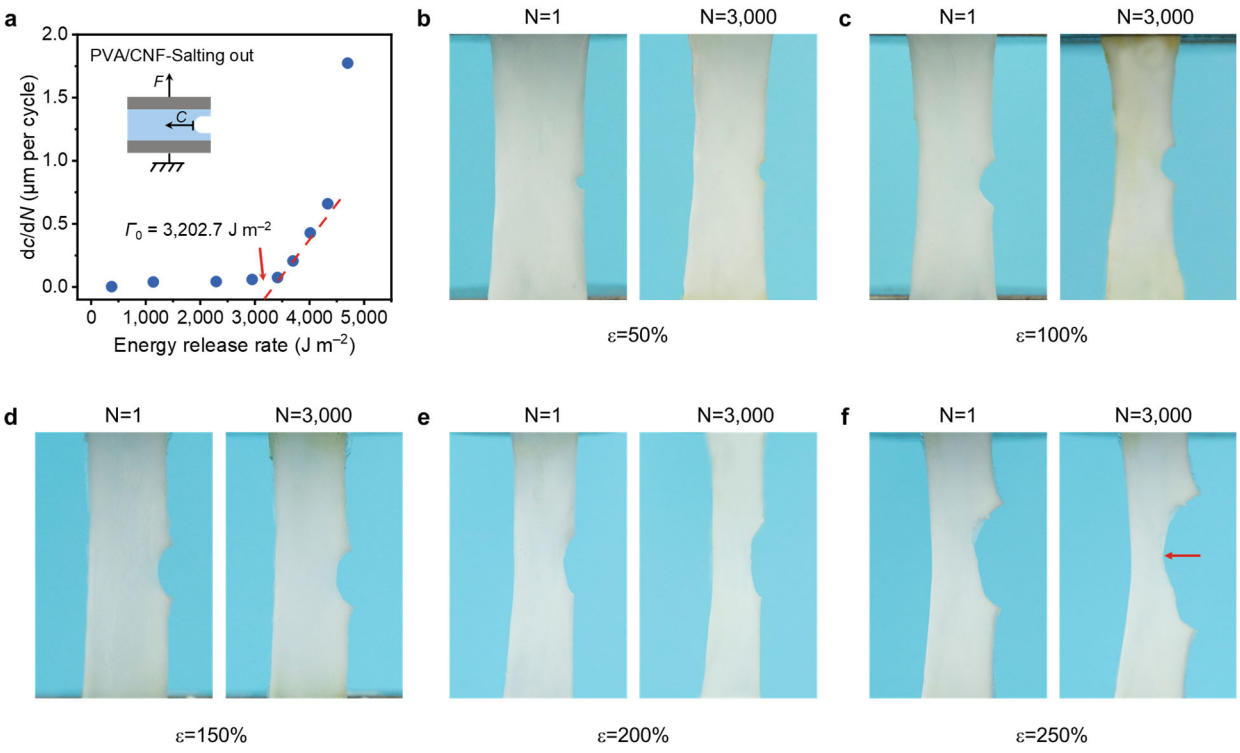

Figure S27. Fatigue resistance of the PVA/CNF-Salting out hydrogel. a, The crack propagation per loading cycle, d*c*/d*N*, versus energy release rate for the PVA/CNF-Salting out hydrogel. **b-f** Fatigue tests of the PVA/CNF-Salting out hydrogel at strains of 50% (**b**), 100% (**c**), 150% (**d**), 200% (**e**), and 250% (**f**), respectively.

Fatigue test results display that the notched PVA/CNF-Salting out hydrogel is loaded and unloaded for 3,000 cycles at strains below 200%, and no visible crack growth or failure is obversed, until crack propagation occurrs at a strain of 250%. Furthermore, a high fatigue threshold of 3,202.7 J m^{-2} is realized, indicating that the hydrogel possesses excellent fatigue resistance.

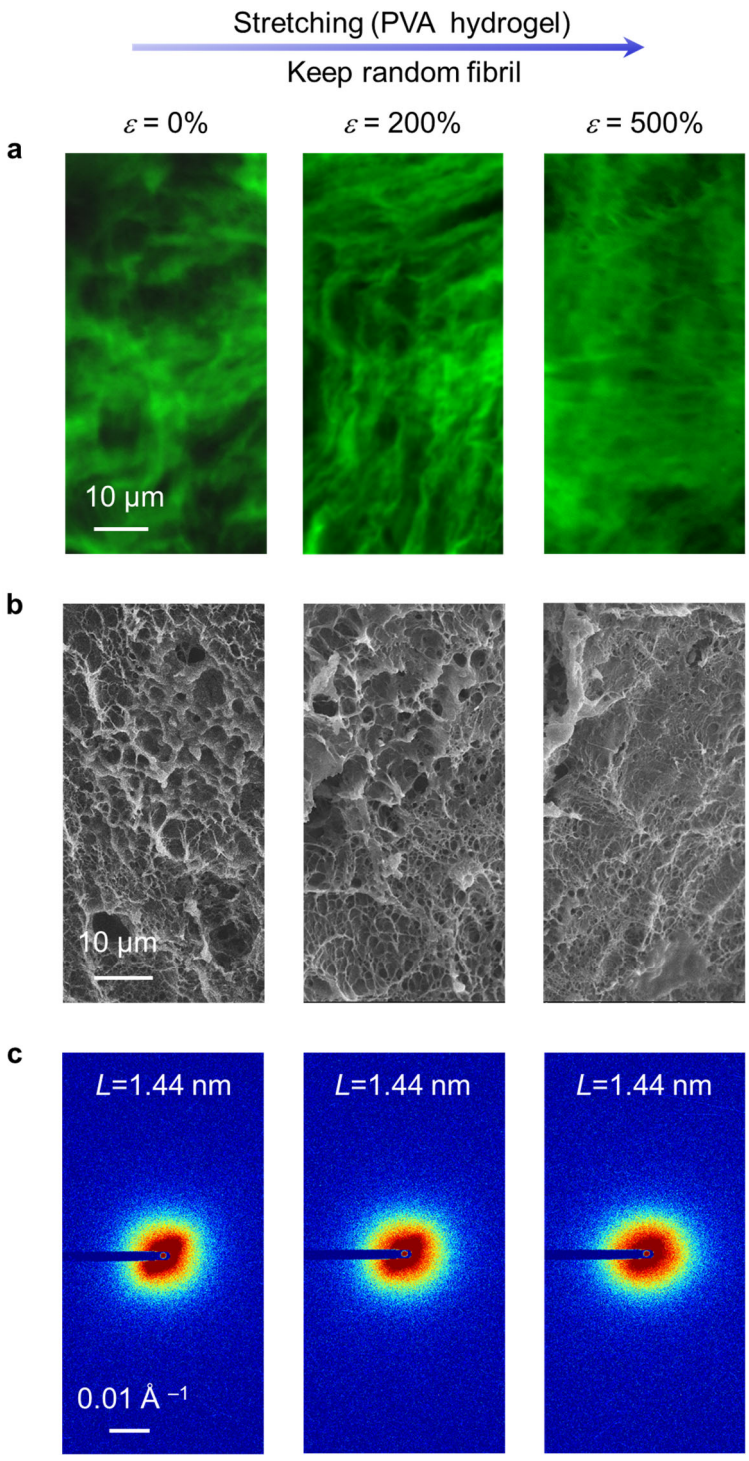

Figure S28. Random alignment behavior of the PVA hydrogel even during stretching. a, b CLSM (**a**) and SEM (**b**) images of the PVA hydrogel at different tensile strains. **c,** In situ stretched SAXS patterns of the PVA hydrogel.

As a control, we found that even at a tensile strain of 500%, the PVA hydrogel consistently remains a random network structure, which is also well demonstrated from the corresponding 2D scattering images.

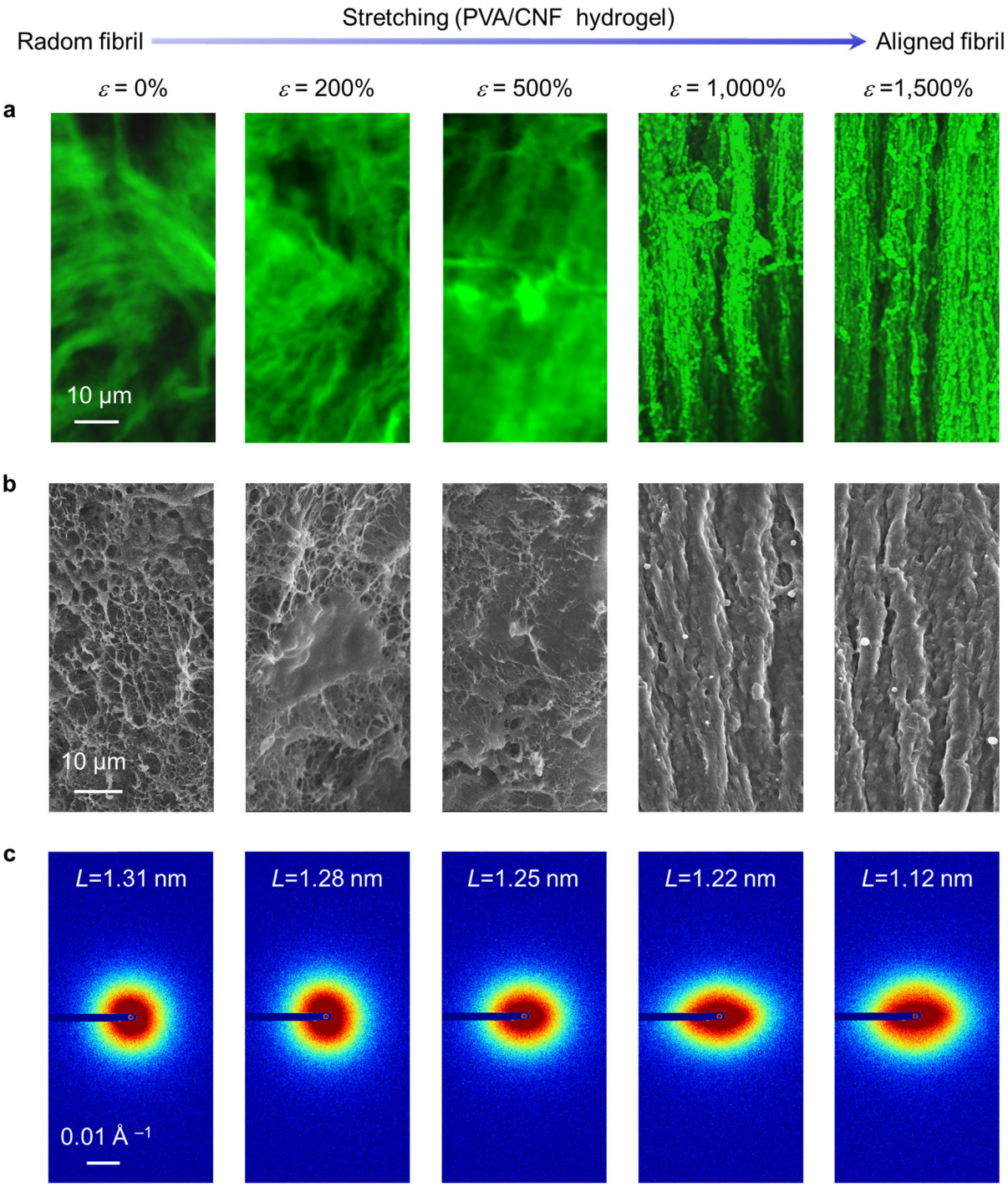

Figure S29. Network structure of the PVA/CNF hydrogel during stretching. a, b CLSM (**a**) and SEM (**b**) images of the PVA/CNF hydrogel at different tensile strains. **c,** In situ stretched SAXS patterns of the PVA/CNF hydrogel.

For the PVA/CNF hydrogel, it can be observed that compared with the PVA hydrogel, a certain alignment structure is presented when the tensile strain is higher than 500%, indicating that CNF contributes to the directional alignment. However, compared with the PVA/CNF-Salting out hydrogel, it exhibits a relatively lower stretchability due to the lack of specific ions.

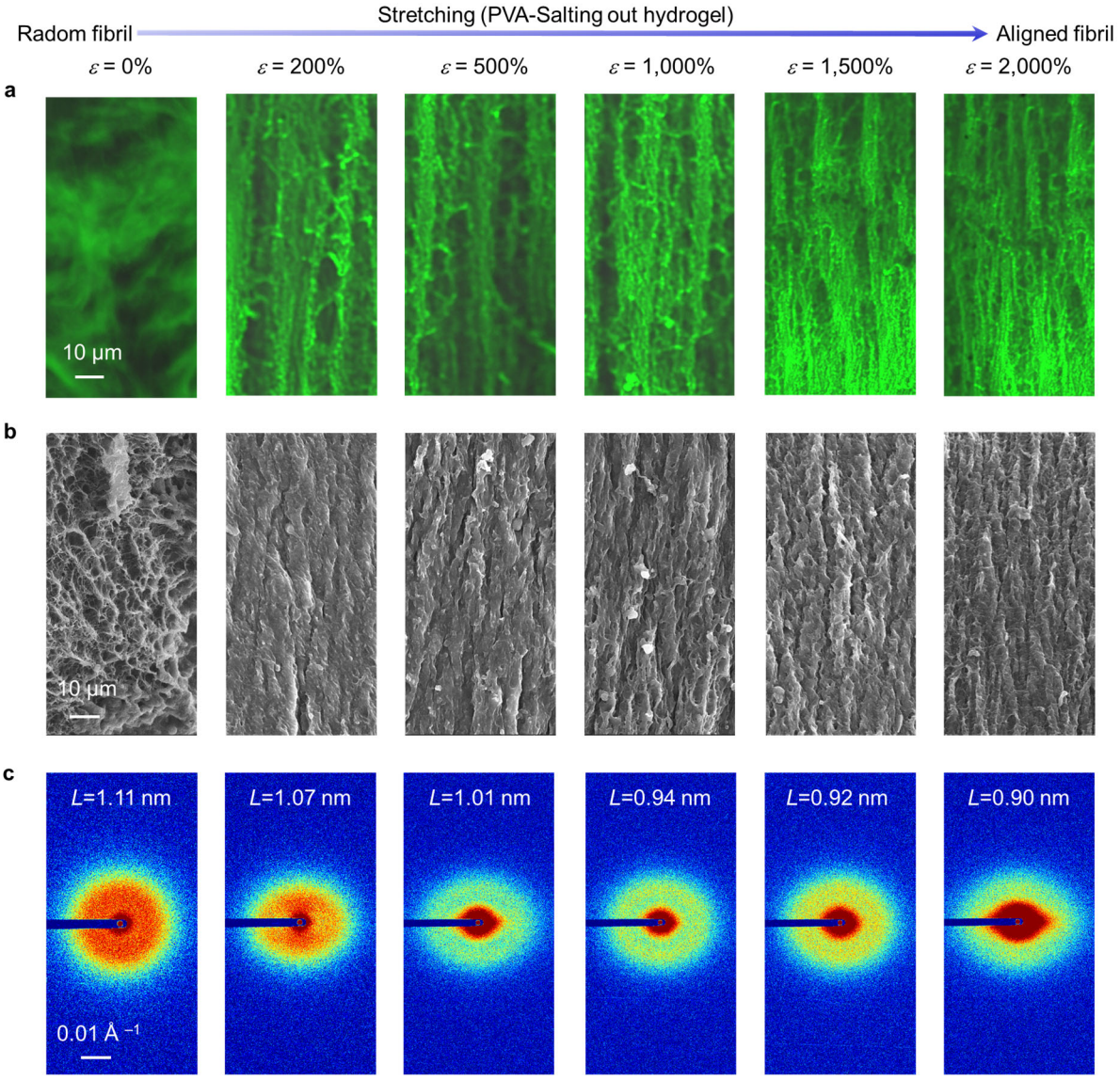

Figure S30. Network structure of the PVA-Salting out hydrogel during stretching. a, b CLSM (**a**) and SEM (**b**) images of the PVA-Salting out hydrogel at different tensile strains. **c,** In situ stretched SAXS patterns of the PVA-Salting out hydrogel.

It can be observed that although the PVA-Salting out hydrogel also has a certain fibril orientation during stretching, when it is stretched to 2,000% strain, the PVA chains are prone to decouple and the hydrogel is easy to break. Note that compared to the PVA/CNF-Salting out hydrogel, the PVA-Salting out hydrogel exhibits lower stretchability.

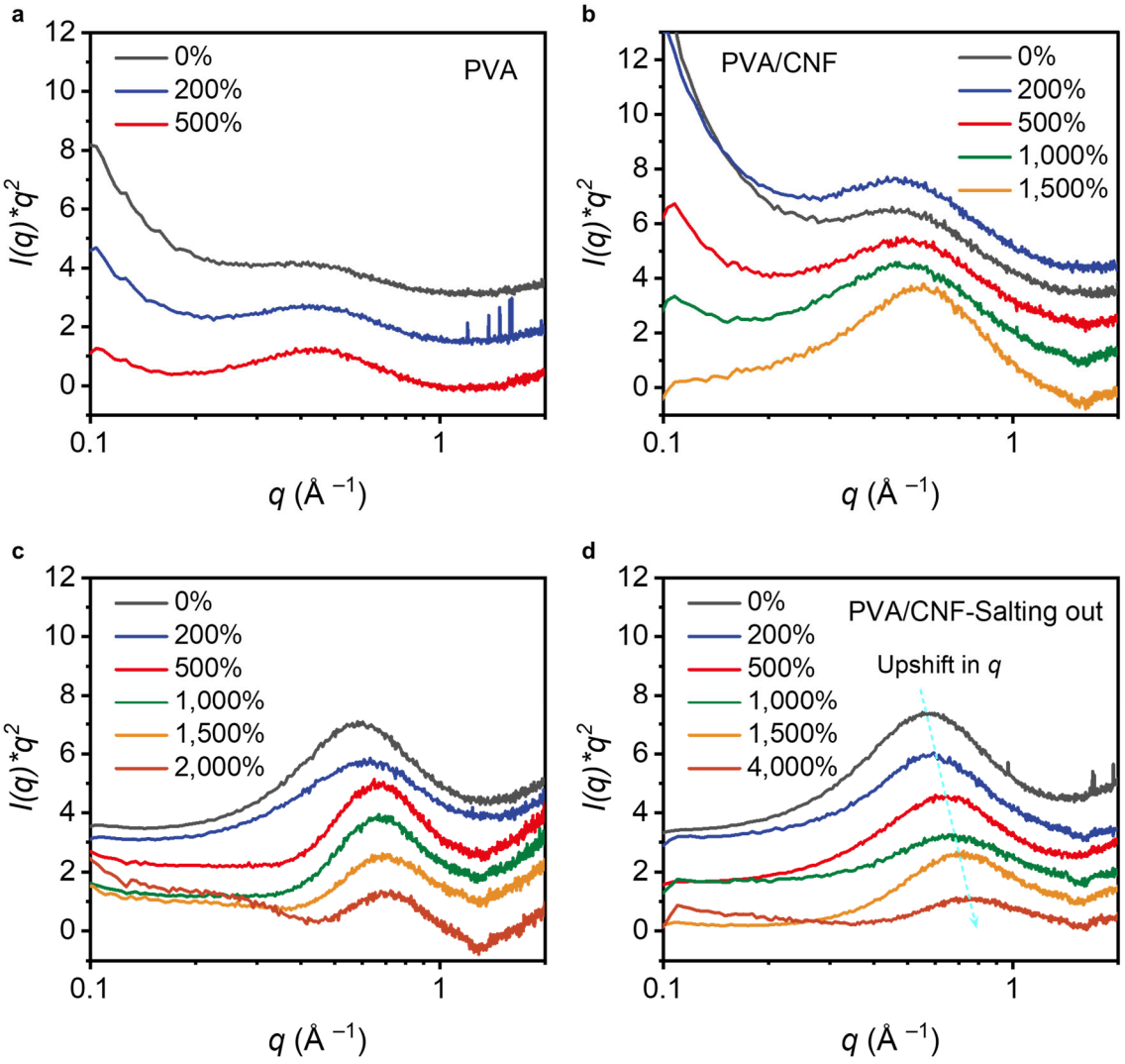

Figure S31. Representative SAXS profiles of four types of hydrogels during stretching. a, SAXS curves of the PVA hydrogel under different strains. **b,** SAXS curves of the PVA/CNF hydrogel under different strains. **c,** SAXS curves of the PVA-Salting out hydrogel under different strains. **d,** SAXS curves of the PVA/CNF-Salting out hydrogel under different strains.

For the PVA hydrogel, with changing strain, the critical vector at $q = 0.435$ corresponding to the peak intensity does not show a significant shift, and the corresponding average distance L is 1.44 nm. For the PVA/CNF hydrogel, the average distance L shortens from 1.31 to 1.12 nm with varying tensile strain. For the PVA-Salting out hydrogel, the average distance L shortens from 1.11 to 0.90 nm with varying tensile strain. For the PVA/CNF-Salting out hydrogel, the average distance L shortens from 1.09 to 0.83 nm with varying tensile strain.

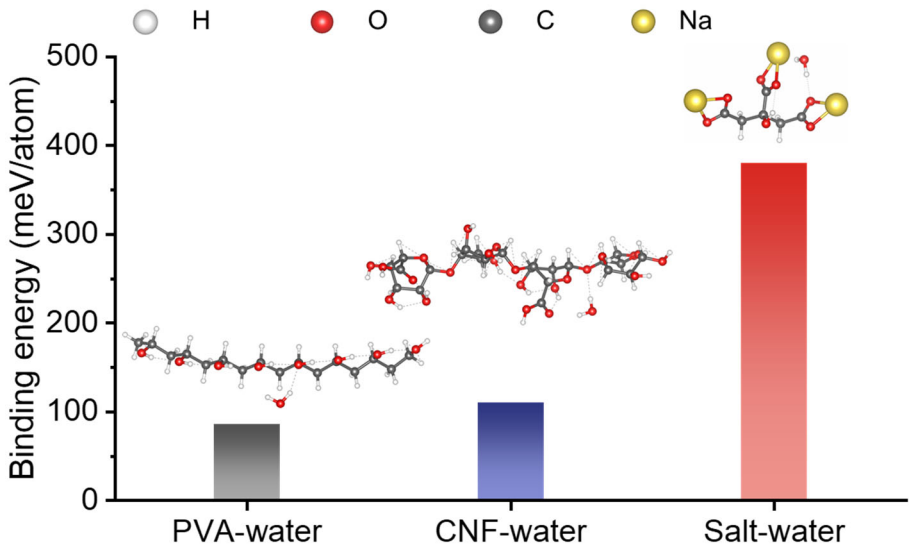

Figure S32. Binding energy of different molecules.

The binding energy of salt-water (380 meV/atom) was much higher than that of PVA-water (86 meV/atom) and CNF-water (110 meV/atom).

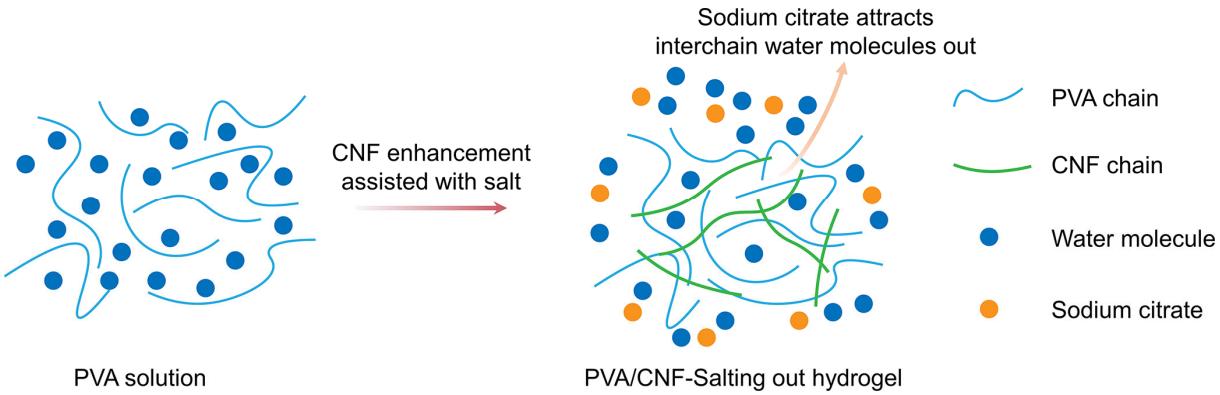

Figure S33. Schematic diagram of the CNF enhancement effect assisted with salt.

This indicates that salt tends to break the H-bonds interaction between water molecules and PVA chains, which accounts for the removal of water molecules between PVA chains and provides the evidence of salting-out effect.

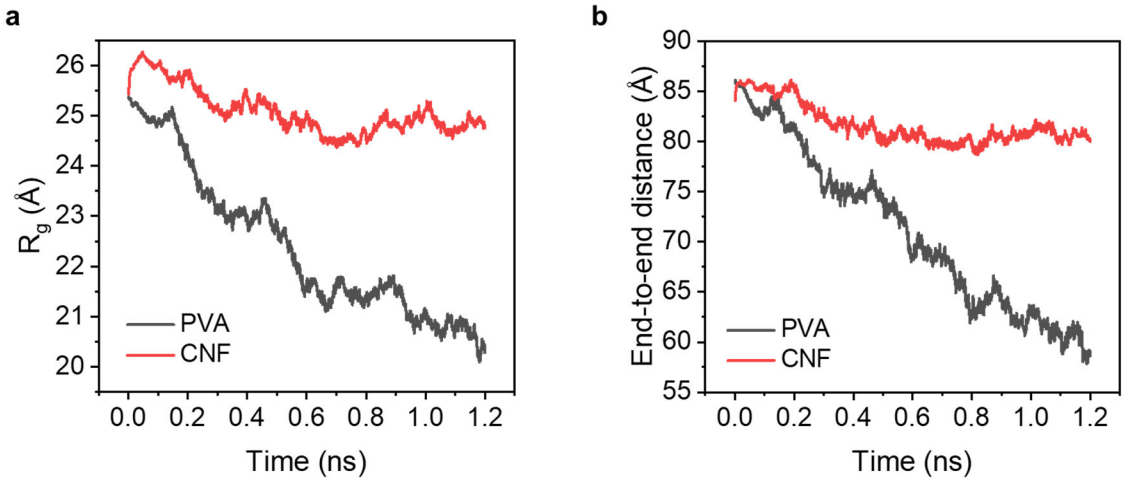

Figure S34. a, b Total radius of gyration **(a)** and end-to-end distance **(b)** of PVA and CNF in water.

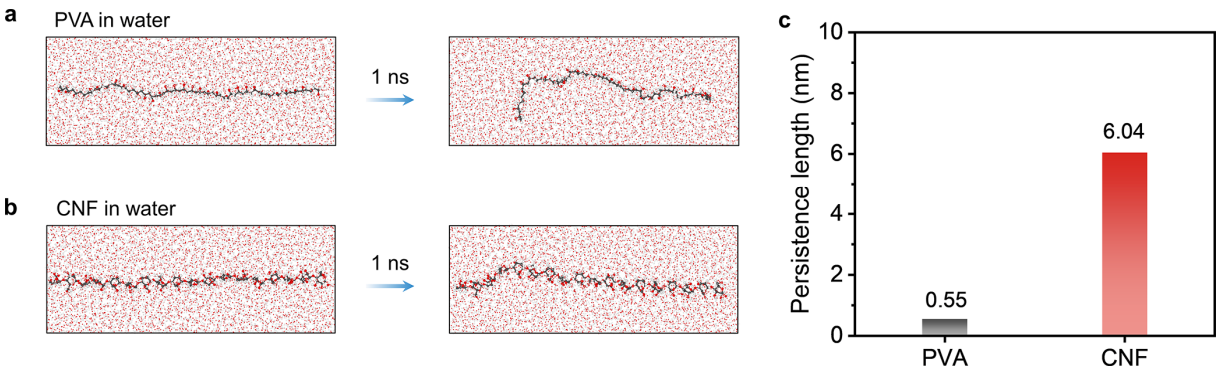

Figure S35. Comparison of rigidity between PVA and CNF. a, b Simulation snapshots of PVA (**a**) and CNF (**b**) in water before and after equilibrium at room temperature (300 K) for 1 ns. **c** Persistence length (L_p) of PVA and CNF chain. The huge discrepancy indicates that CNF is relatively rigid compared to PVA.

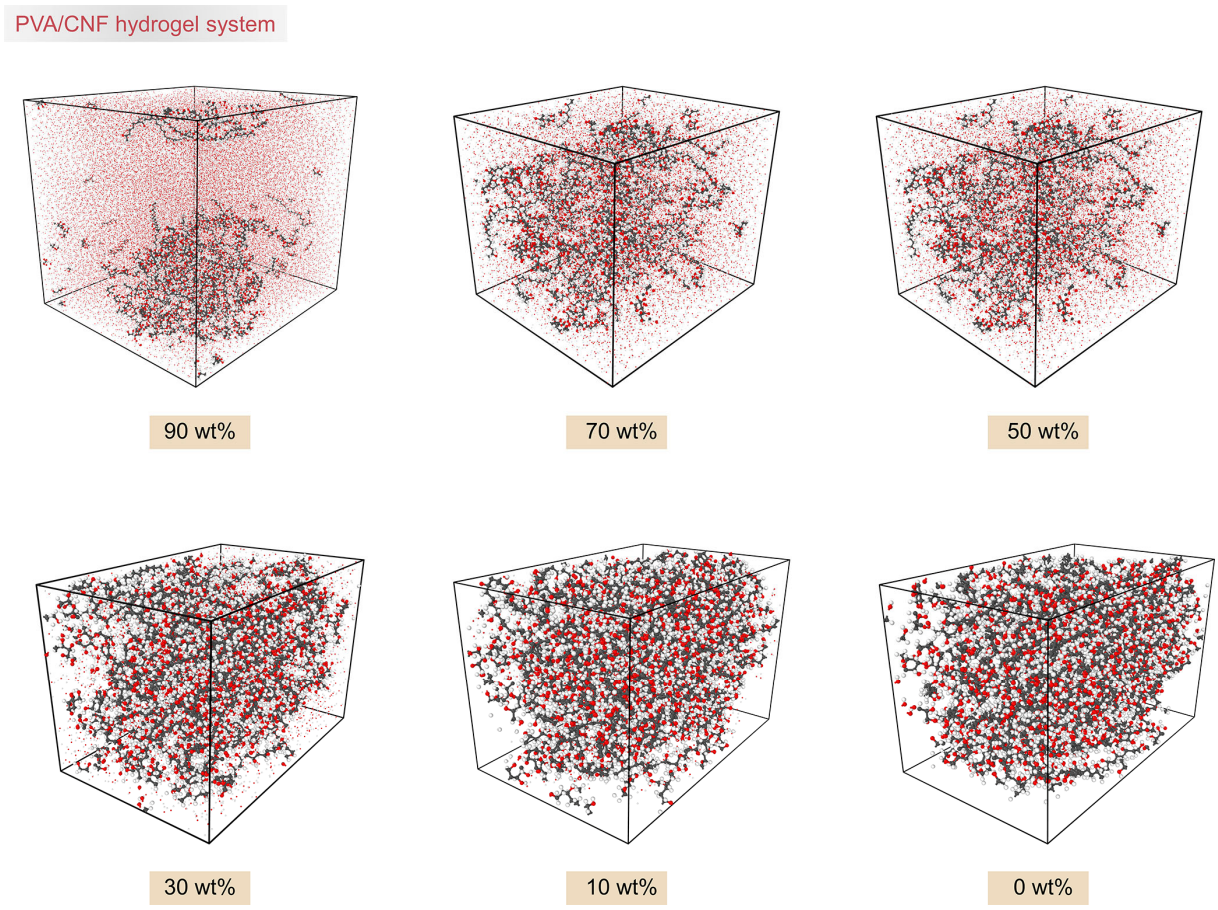

Figure S36. Simulation snapshots of PVA/CNF hydrogels with different water content. To balance the computational cost and accuracy, the water content was regulated by adjusting the number of water molecules. This induces the change of box size for systems equilibrated at 300 K in NPT ensemble.

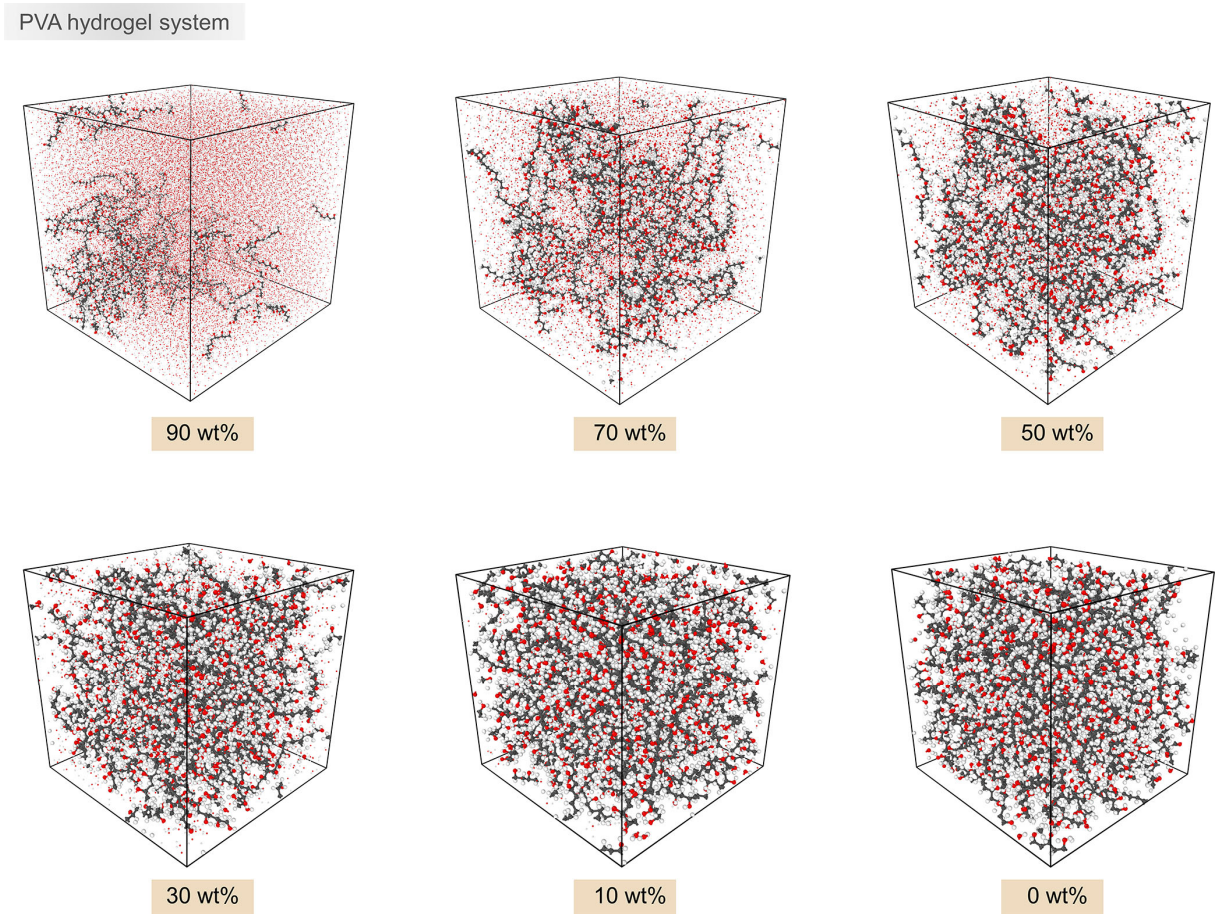

Figure S37. Simulation snapshots of PVA hydrogels with different water content. To balance the computational cost and accuracy, the water content was regulated by adjusting the number of water molecules. This induces the change of box size for systems equilibrated at 300 K in NPT ensemble.

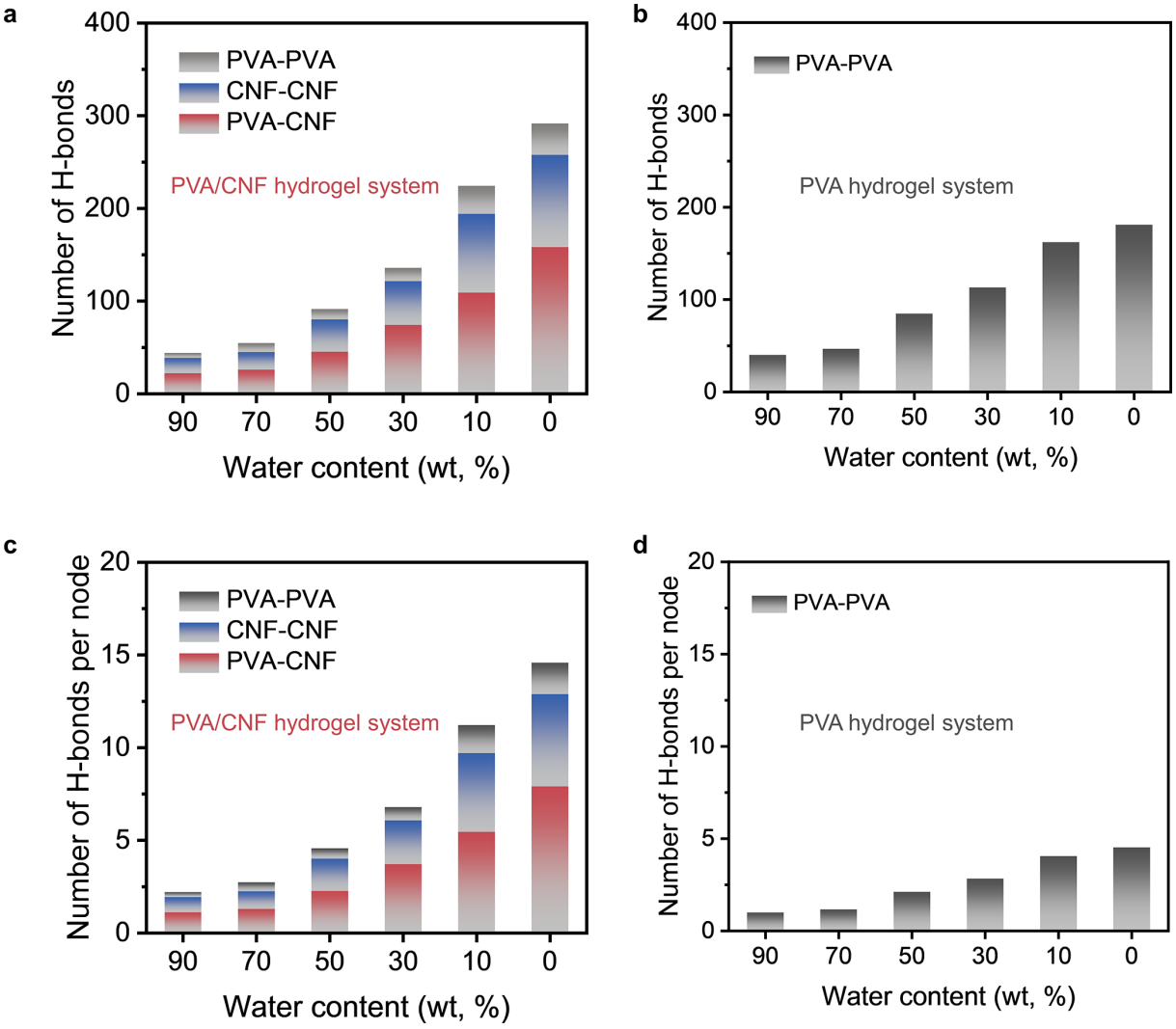

Figure S38. Number of H-bonds of the hydrogels containing different water content. a, b Total number of H-bonds for PVA/CNF hydrogel system and PVA hydrogel system (**b**). **c, d** Number of H-bonds per node for PVA/CNF hydrogel system (**c**) and PVA hydrogel system (**d**).

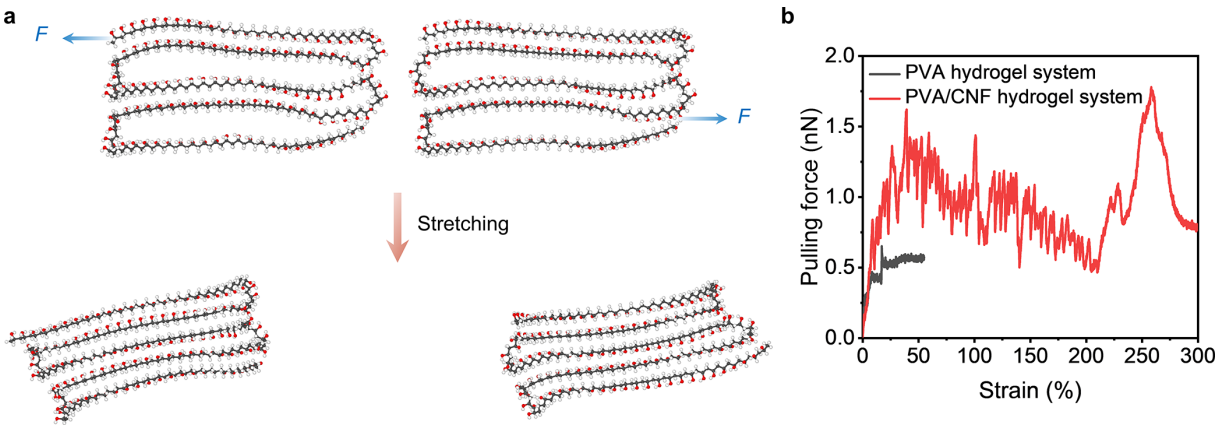

Figure S39. Effect of CNF on the load transfer behaviors. a Simulation snapshots of PVA under tension. **b** Pulling force-strain curves of PVA hydrogel system and PVA/CNF hydrogel system.

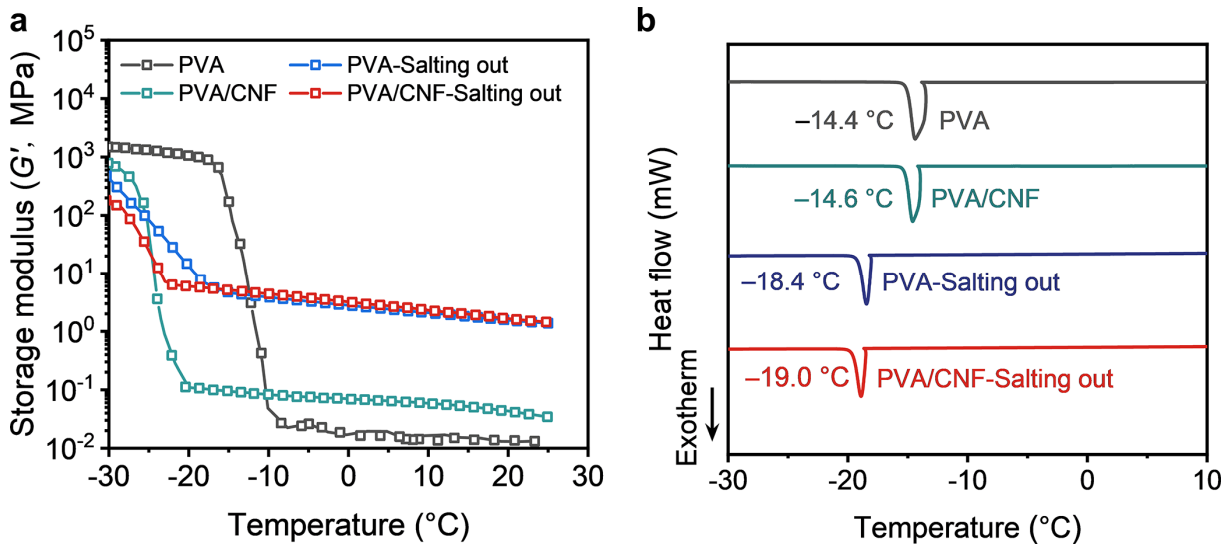

Figure S40. Freezing resistance properties of hydrogels. a, b Storage modulus (G') (**a**) and DSC curves (**b**) of hydrogels.

Benefiting from the ice crystal inhibition of ionic salts, the PVA/CNF-Salting out hydrogel performs a significantly lower freezing point of −19 °C compared to the PVA hydrogel, indicating its excellent low temperature resistance.

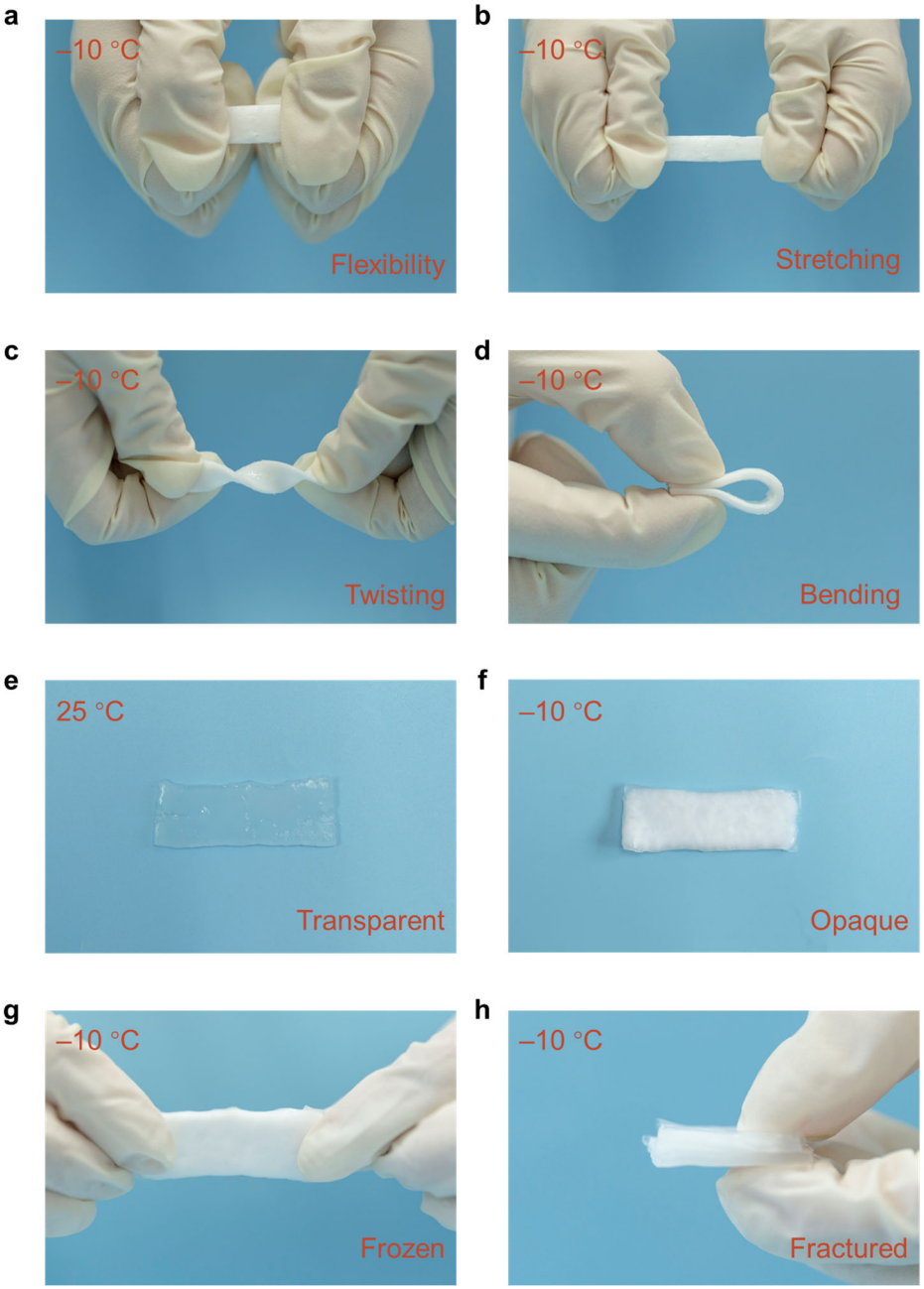

Figure S41. Optical images of hydrogel at low temperature. a-d Photographs of the PVA/CNF-Salting out hydrogel placed (**a**), stretched (**b**), twisted (**c**), and bent (**d**) at −10 °C. **e-f** Photographs of the PVA hydrogel at 25 °C (**e**)and −10 °C (**f**) and before (**g**) and after (**h**) bending at −10 °C.

Due to the excellent freezing tolerance, stretching, twisting or bending of the PVA/CNF-Salting out hydrogel can be easily achieved, representing outstanding mechanical properties even at −10 °C. However, the PVA hydrogel is rapidly frozen at −10 °C and transforms from initially transparent to opaque, while being prone to fracture under external forces because of its inherently high freezing point.

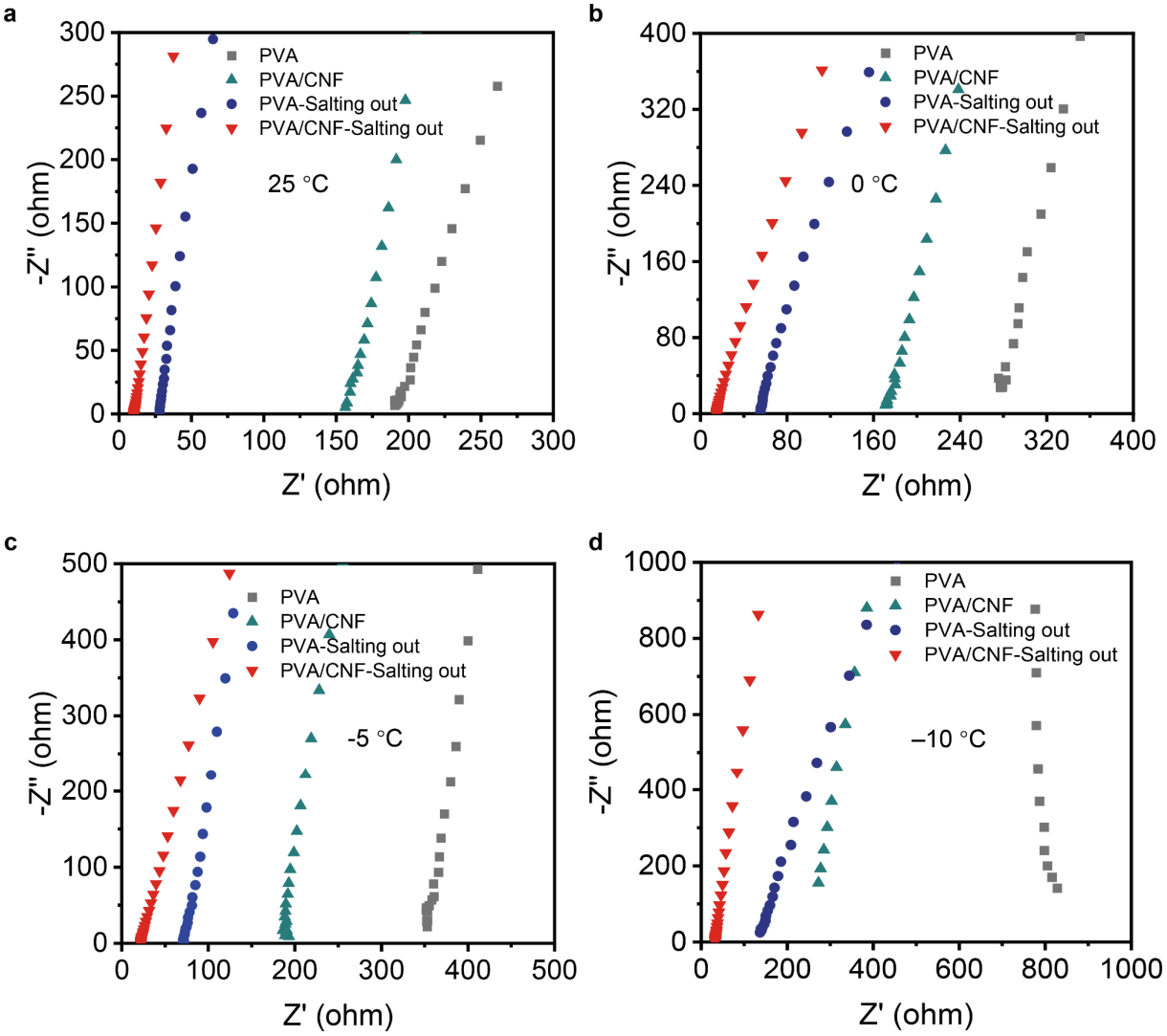

Figure S42. Electrochemical AC impedance spectra (IMP) of hydrogels at 25 (**a**), 0 (**b**), −5 (**c**) and −10 °C (**d**).

It can be seen from the IMP spectrum that the internal resistance of all hydrogels exhibits a natural increasing trend with decreasing temperature. However, we found that the PVA/CNF-Salting out hydrogel possesses the lowest internal resistance regardless of the temperature environment, which is attributed to its low freezing point that ensures the free movement of ions in the network even at low temperature.

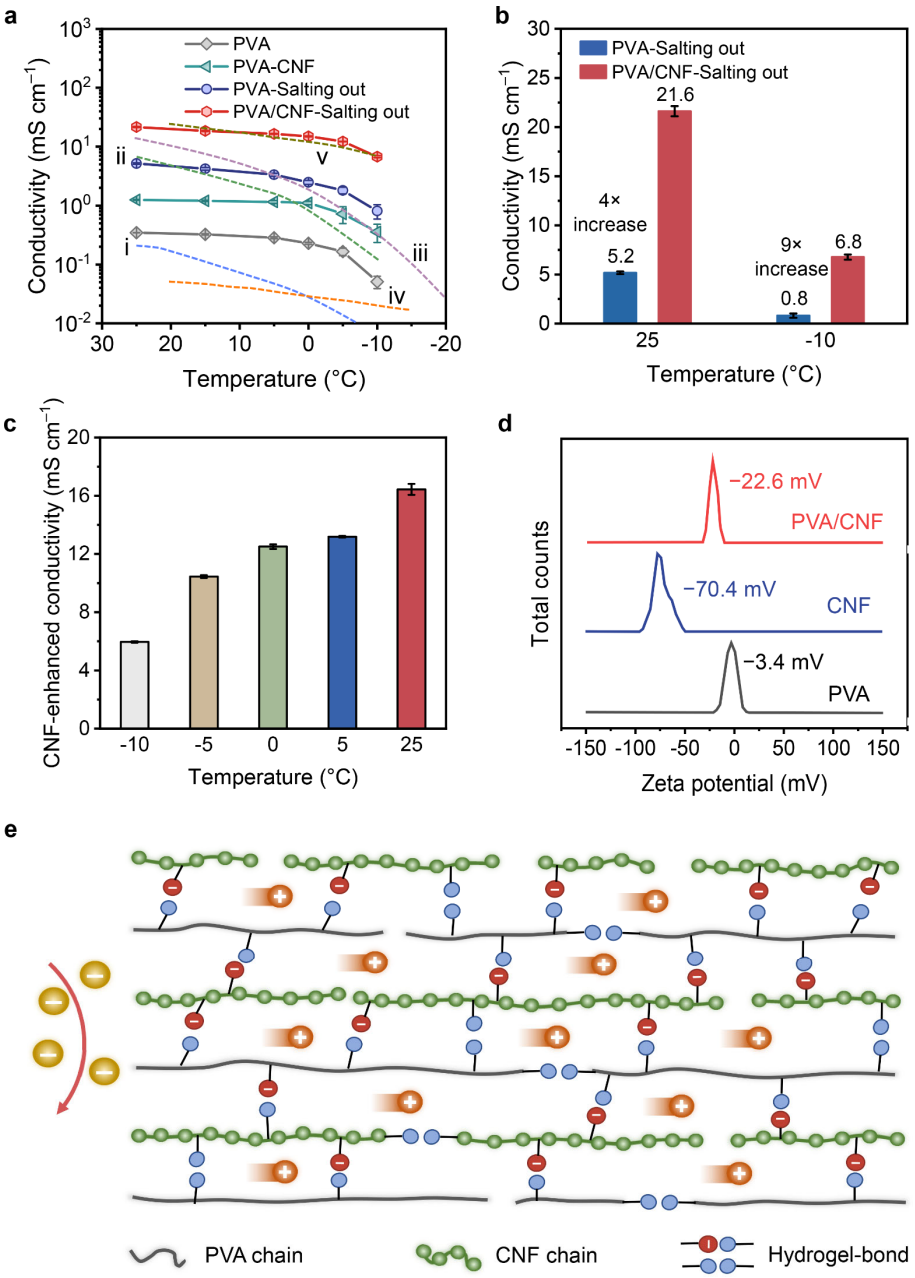

Figure S43. Electrochemical properties of hydrogels. a, Ionic conductivity of hydrogels at different temperatures. **b,** Comparison of ionic conductivity of the PVA-Salting out hydrogel and PVA/CNF-Salting out hydrogel at 25 and −10 °C. **c,** The increasing effect of CNF on the ionic conductivity of hydrogels. **d,** Zeta potential of PVA, CNF and PVA/CNF dispersions. **e,** Schematic illustration of the mechanism of CNF enhancing the ionic conductivity of hydrogels. Error bars show the standard deviation from three independent specimens.

The ionic conductivity of all hydrogels show a natural decreasing trend with decreasing temperature. As we expected, the PVA/CNF-Salting out hydrogel present the highest ionic conductivity, that is, 21.6 and 6.8 mS cm^{-1} at 25 and −10 °C, respectively, which exceeds most

existing ionic conductive tough hydrogels (Figure S43a).[7–11] Notably, the aid of CNFs can significantly enhance the ionic conductivity, respectively showing an astounding 4-fold and 9-fold increase at room temperature and −10 °C compared to the PVA-Salting out hydrogel (Figure S43b, c). This interesting finding is attributed to a fact that negatively charged complexes can facilitate the rapid migration of free ions by providing high-speed channels (Figure S43d, e).

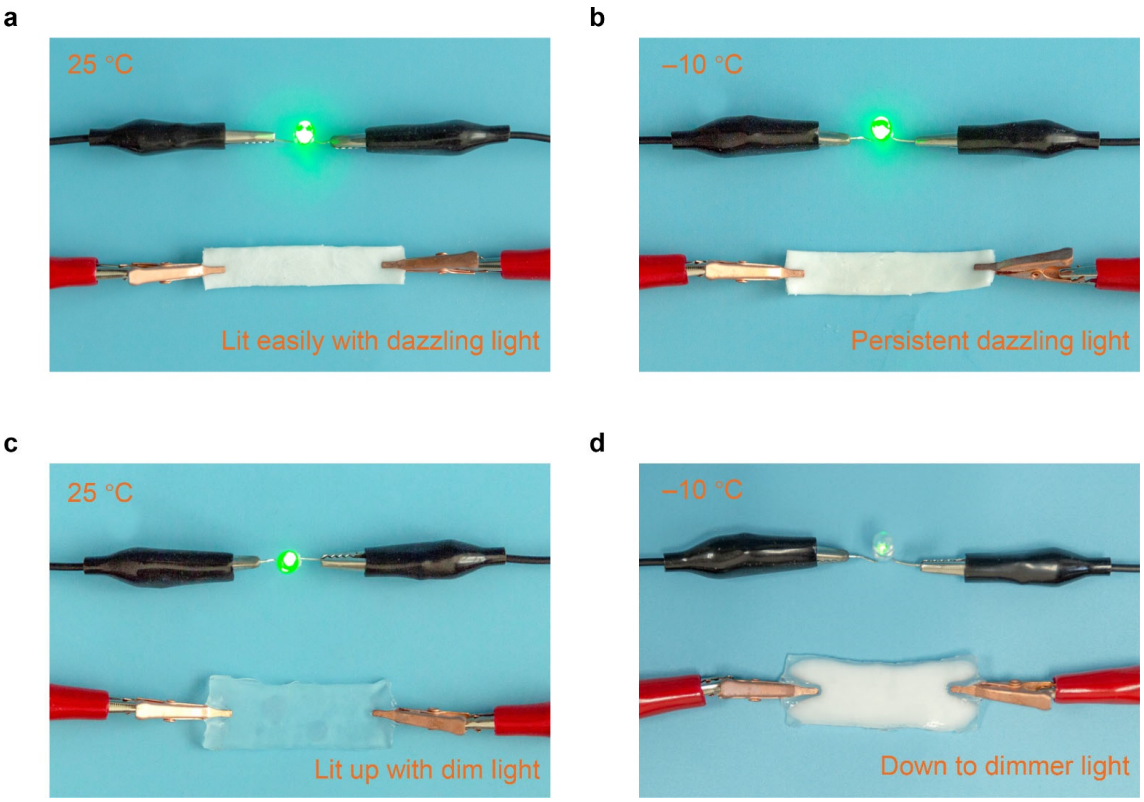

Figure S44. a, b Photographs of the PVA/CNF-Salting out hydrogel as ionic conductor lighting up a LED lamps at 25 °C (**a**) and −10 °C (**b**). **c, d** Photographs of the PVA hydrogel as ionic conductor lighting up a LED lamps at 25 °C (**c**) and −10 °C (**d**).

On account of the excellent freezing resistance and ionic conductivity, the PVA/CNF-Salting out hydrogel can easily light up a LED lamps and emit dazzling light even at −10 °C. In sharp contrast, the high internal resistance of the PVA hydrogel only yield dim a LED despite at 25 °C, and expectedly becomes weaker when placed on −10 °C.

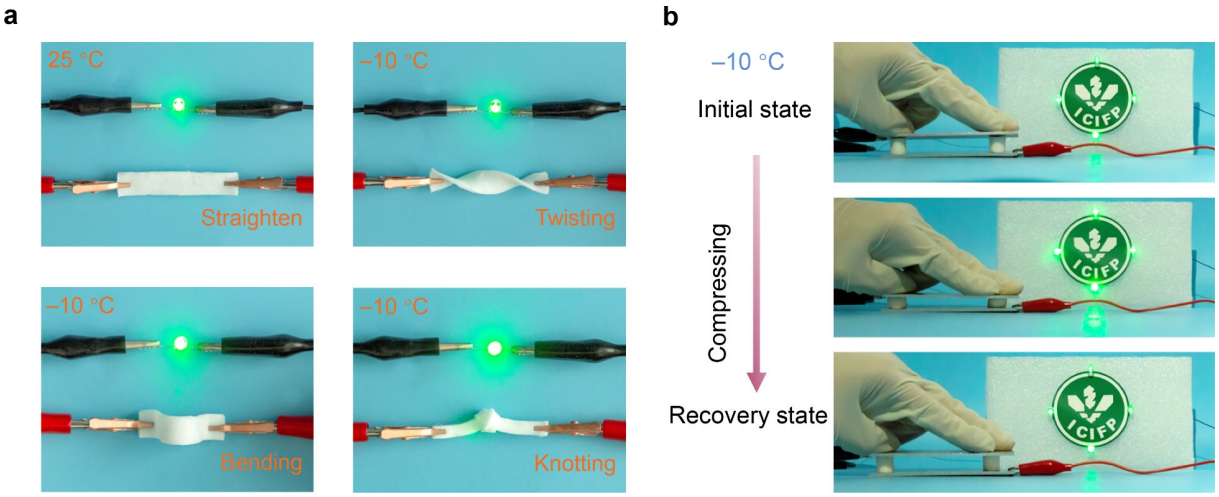

Figure S45. a, Photographs of the PVA/CNF-Salting out hydrogel lighting up a LED under different deformations at −10°C. **b,** Photographs of the change of LED lamp brightness under external force when the PVA/CNF-Salting out hydrogel is served as an ionic conductor.

Combining good mechanical properties, high ionic conductivity, and freezing tolerance, the PVA/CNF-Salting out hydrogel can light up a LED and emit dazzling light under stretching, twisting, bending, and knotting deformation. Moreover, when acting as an ionic conductor, the LED brightness exhibits a visual response of brightening and dimming under the extrusion and recovery of an external force, indicating its promising application in the field of strain or stress sensors.

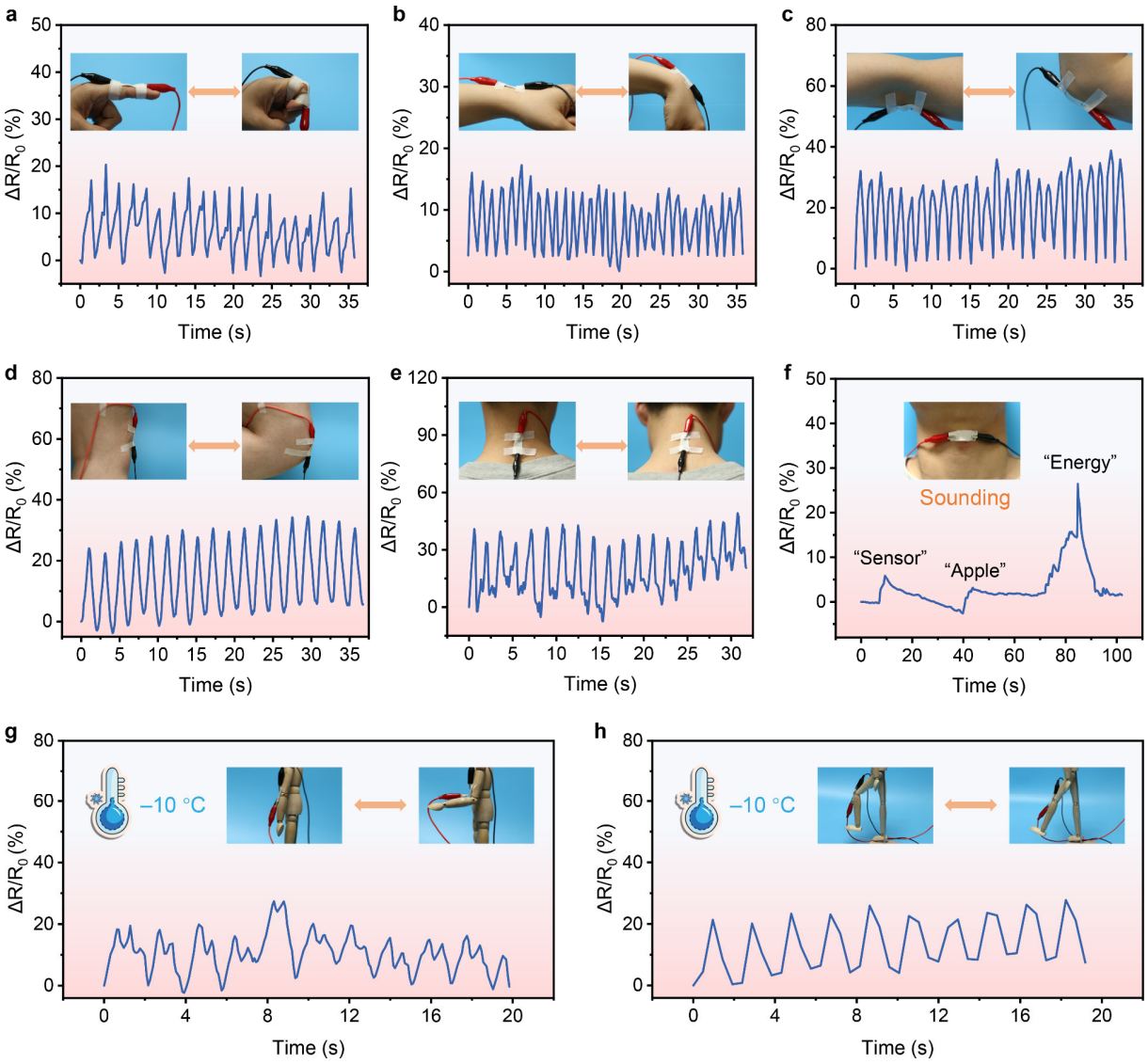

Figure S46. Advanced the PVA/CNF-Salting out hydrogel-based sensor in monitoring human joints and physiological signals. a-f The relative resistance changes of the hydrogel sensor in response to bending and releasing of finger (**a**) wrist (**b**), elbow (**c**), knee (**d**), nod (**e**), and sounding (**f**). **g, h** The hydrogel sensor attachs to a human model for monitoring elbow (**g**) and knee (**h**) rotation at −10 °C.

At room temperature and −10 °C, the resistance of the PVA/CNF-Salting out hydrogel-based sensor show repeated and stable responsive changes during deformations and could be applied to monitor body movements and physiological signals. The peak part of the relative resistance changes curves presents that the hydrogel is deformed, and the valley part indicates it returns to the original state.

Supplemental Tables

Table S1. Summary of the four types of produced hydrogels.

Types	Tensile strain (%)	Tensile strength (MPa)	Toughness (MJ m^{-3})	True tensile strength (MPa)	Compressive strength (MPa)	Fracture energy (kJ m^{-2})	Tearing energy (kJ m^{-2})
PVA	1,231	0.09	0.6	0.6	2.4	0.8	0.5
PVA/CNF	1,974	0.2	2.5	2.6	5.1	4.0	0.7
PVA-Salting out	2,950	1.3	21.5	49.6	18.0	28.3	6.5
PVA/CNF-Salting out	7,430	3.9	141.4	421.6	51.7	95.7	11.9

Table S2. Summary of strong and tough hydrogels.

Network structure	Hydrogel components	Tensile strain (%)	True tensile strength (MPa)	Fracture energy (kJ m^{-2})	Fatigue threshold (J m^{-2})	Compressive strength (MPa)	Tearing energy (kJ m^{-2})	References
Isotropic	**PVA/CNF/NaCitr**	**7,430**	**421.6**	**95.7**	**3,202.7**	**51.7**	**11.9**	**This work**
Isotropic	Gelatin/$(NH_4)_2SO_4$	200	~0.5	2.3	N/A	0.8	N/A	Ref. [12]
	PAAM/PDMAA	~3,230	~9	87	2,120	N/A	N/A	Ref. [13]
	PAM/PAMPS	5,300	~10.6	157	4,200	N/A	N/A	Ref. [14]
	PAM/PDMS	~200	~0.5	87	N/A	N/A	N/A	Ref. [15]
	PVA/Alg/$ZnSO_4$	750	15	39	N/A	N/A	N/A	Ref. [16]
	PVA/KAc	400	~16	70.8	N/A	N/A	N/A	Ref. [17]
	PAM/Carrageenan/KCl	700	~2.8	14.0	N/A	N/A	N/A	Ref. [18]
	PVA/DESs	550	20.2	62.7	N/A	N/A	4.24	Ref. [19]
	PVA	~800	~67.2	~60	770	N/A	N/A	Ref. [20]
	PAM/Alg/$BaCl_2$	~650	~8.5	1.09	N/A	N/A	N/A	Ref. [21]
	PAM/Alg/$CaSO_4$	~2,250	~1.8	8.7	N/A	N/A	N/A	Ref. [22]
	Gelatin/$(NH_4)_2SO_4$	126	~0.5	0.4	N/A	1.05	N/A	Ref. [23]
	PAM/CMCS/$Zn(ClO_4)_2$	~630	~2.5	~12.6	N/A	~10	N/A	Ref. [24]
Anisotropic	PVA/NaCitr	2,900	~440	131.1	10,500	N/A	N/A	Ref. [25]
	PVA /NaCitr/DMSO	1,100	~148.5	~1279	N/A	N/A	N/A	Ref. [26]
	PVA	~250	~13	~65	1,250	N/A	N/A	Ref. [27]
	PVA/GO	~240	~21.1	~105.6	1,567	N/A	N/A	Ref. [28]
	PVA/ethanol/$FeCl_3$	1,710	~111.1	661.54	N/A	N/A	N/A	Ref. [29]
	PVA	400	~10	50	1,340	N/A	N/A	Ref. [30]
	Cellulose	316	~2	0.83	N/A	N/A	N/A	Ref. [31]
	PVA/ polyaniline	360	~4.4	29.8	N/A	4.62	N/A	Ref. [32]
	PAM/AgNW/Ag-CNT	2,430	~41.3	~20.6	N/A	N/A	N/A	Ref. [33]
	PAM/Alg	1,400	~7.3	6.1	N/A	N/A	N/A	Ref. [34]
	PAM/PAA/$FeCl_3$	~240	~84	~42	N/A	N/A	N/A	Ref. [35]

Table S3. Summary of stretchable and tough hydrogels.

Enhancement mechanisms	Hydrogel components	Tensile strain (%)	Toughness (MJ m^{-3})	References
Nanofibril and salt-assisted	**PVA/CNF/NaCitr**	**7430**	**141.4**	**This work**
Single-network (I)	PVA/DMSO	500	5.05	Ref. [36]
Metal coordination (II)	PAM/$CaCl_2$	~5,800	~0.23	Ref. [15]
	PAM/PAA/$FeCl_3$	~240	~42	Ref. [35]
Cross-linked (III)	PVA/Alg/$ZnSO_4$	750	56	Ref. [16]
	PVA	~800	~33.6	Ref. [20]
	Cellulose	316	0.83	Ref. [31]
	PEG/ hydroxypropyl-a-cyclodextrin	~1,300	22	Ref. [37]
	PAM/Polyprotein	~1,100	~0.06	Ref. [38]
Double-network (IV)	PAM/Carrageenan/KCl	700	1.4	Ref. [18]
	PAM/Alg/$BaCl_2$	~650	~4.2	Ref. [21]
	PAM/Alg/$CaSO_4$	~2,250	~0.2	Ref. [22]
	PAM/Alg	1,400	6.1	Ref. [34]
	PAM/PAMPS/bicyclo[6.2.0]decane	1,000	6.4	Ref. [19]
	Gelatin/CS/Phytate	~680	4.76	Ref. [40]
Nanocomposite (V)	PAAM/PDMAA	~3,230	19	Ref. [13]
	PAM/PAMPS	5,300	18.9	Ref. [14]
	PAM/AgNW/Ag-CNT	2,430	~20.6	Ref. [33]
	PAM/PDMS	~200	~0.25	Ref. [41]
	PVA/GO	~240	~10.56	Ref. [28]
Salting-out (VI)	Gelatin/$(NH_4)_2SO_4$	200	0.23	Ref. [12]
	PVA/KAc	400	7.8	Ref. [17]
	Gelatin/$(NH_4)_2SO_4$	126	0.04	Ref. [23]
	PAM/CMCS/$Zn(ClO_4)_2$	~630	~1.26	Ref. [24]
	PVA/NaCitr	2,900	175	Ref. [25]
	PVA/NaCitr/DMSO	1,100	127.9	Ref. [26]
	PAM/CS/NaCitr	~400	~11.2	Ref. [42]
	PVA/PAM/NaCl	2,224	0.28	Ref. [43]
	PVA/CMC/EG/$Zn(CF_3SO_3)_2$	423.1	1.35	Ref. [44]

Table S4. Summary of tough and fatigue-resistant hydrogels.

Enhancement mechanisms	Hydrogel components	Fracture energy (kJ m^{-2})	Fatigue threshold (J m^{-2})	References
Nanofibril and salt-assisted	**PVA/CNF/NaCitr**	**95.7**	**3,202.7**	**This work**
Single-network	PVA/DMSO	~1	~200	Ref. [36]
Double-network	PAM/Alg/$BaCl_2$	1.09	~121.1	Ref. [21]
	PAM/PAMPS/bicyclo[6.2.0]decane	2.84	~315.6	Ref. [39]
	Gelatin/CS/Phytate	13.79	1,532.2	Ref. [40]
	PMMA/Alg	92.3	2,682	Ref. [45]
	PAM/Alg/$CaSO_4$	~1.8	200	Ref. [46]
Nanocomposite	PAAM/PDMAA	87	2,120	Ref. [13]
	PAM/PDMS	4.136	1,290	Ref. [41]
	PVA/GO	~12	1,567	Ref. [28]
Cross-linked	PVA/Alg/$ZnSO_4$	39	N/A	Ref. [16]
	PVA	~60	770	Ref. [20]
	PEG/ hydroxypropyl-a-cyclodextrin	3.6	N/A	Ref. [37]
	PAM/Polyprotein	~0.9	~126	Ref. [38]
Salting-out	PVA/NaCitr	131.1	10,500	Ref. [25]
	PAM/CS/NaCitr	14.0	~1,500	Ref. [42]
	PVA/CMC/EG/$Zn(CF_3SO_3)_2$	13.5	~1,445	Ref. [44]
Annealed	PVA	~10	1,000	Ref. [6]
	PVA	~12.5	1,340	Ref. [30]
Biological	Skeletal muscle	~50	~1000	Ref. [27]
	Heart valve	~20	~400	Ref. [47]

Supplemental References

[1] S. Wang, L. Yu, S. Wang, L. Zhang, L. Chen, X. Xu, Z. Song, H. Liu, C. Chen, *Nat. Commun.* **2022**, *13*, 3408.

[2] M. Vatankhah-Varnosfaderani, A. N. Keith, Y. Cong, H. Liang, M. Rosenthal, M. Sztucki, C. Clair, S. Magonov, D. A. Ivanov, A. V. Dobrynin, S. S. Sheiko, *Science* **2018**, *359*, 1509.

[3] Y. Zheng, R. Kiyama, T. Matsuda, K. Cui, X. Li, W. Cui, Y. Guo, T. Nakajima, T. Kurokawa, J. P. Gong, *Chem. Mater.* **2021**, *33*, 3321.

[4] R. Bai, B. Chen, J. Yang, Z. Suo, *J. Mech. Phys. Solids* **2019**, *125*, 749.

[5] R. Bai, J. Yang, Z. Suo, *Eur. J. Mech. A. Solids* **2019**, *74*, 337.

[6] X. L. Shaoting Lin, Ji Liu, Hyunwoo Yuk, Hyun-Chae Loh, German A. Parada, Charles Settens, Jake Song, Admir Masic, Gareth H. McKinley, Xuanhe Zhao, *Sci. Adv.* **2019**, *5*, eaau8528.

[7] R. Tong, G. Chen, D. Pan, H. Qi, R. a. Li, J. Tian, F. Lu, M. He, *Biomacromolecules* **2019**, *20*, 2096.

[8] Y. Wang, L. Zhang, A. Lu, *J. Mater. Chem. A* **2020**, *8*, 13935.

[9] B. Ying, R. Z. Chen, R. Zuo, J. Li, X. Liu, *Adv. Funct. Mater.* **2021**, *31*, 2104665.

[10] C. Lu, X. Chen, *Nano Lett.* **2020**, *20*, 1907.

[11] J. Xu, R. Jing, X. Ren, G. Gao, *J. Mater. Chem. A* **2020**, *8*, 9373.

[12] L. B. Jiang, D. H. Su, S. L. Ding, Q. C. Zhang, Z. F. Li, F. C. Chen, W. Ding, S. T. Zhang, J. Dong, *Adv. Funct. Mater.* **2019**, *29*, 1901314.

[13] W. Li, L. Li, S. Zheng, Z. Liu, X. Zou, Z. Sun, J. Guo, F. Yan, *Adv. Mater.* **2022**, *34*, 2203049.

[14] W. Li, S. Zheng, X. Zou, Y. Ren, Z. Liu, W. Peng, X. Wang, D. Liu, Z. Shen, Y. Hu, J. Guo, Z. Sun, F. Yan, *Adv. Funct. Mater.* **2022**, *32*, 2207348.

[15] H. Zhang, Z. Liu, J. Mai, N. Wang, H. Liu, J. Zhong, X. Mai, *Adv. Sci.* **2021**, *8*, 2100320.

[16] W. Cui, Y. Zheng, R. Zhu, Q. Mu, X. Wang, Z. Wang, S. Liu, M. Li, R. Ran, *Adv. Funct. Mater.* **2022**, *32*, 2204823.

[17] S. Wu, T.-W. Wang, Y. Du, B. Yao, S. Duan, Y. Yan, M. Hua, Y. Alsaid, X. Zhu, X. He, *NPG Asia Mater.* **2022**, *14*, 65.

[18] Y. Lin, Z. Wu, C. Li, Q. Ding, K. Tao, K. Zhai, M. Chen, M. Zilberman, X. Xie, J. Wu, *EcoMat* **2022**, *4*, e12220.

[19] H. Zhang, N. Tang, X. Yu, M. H. Li, J. Hu, *Adv. Funct. Mater.* **2022**, *32*, 2206305.

[20] J. Ni, S. Lin, Z. Qin, D. Veysset, X. Liu, Y. Sun, A. J. Hsieh, R. Radovitzky, K. A. Nelson, X. Zhao, *Matter* **2021**, *4*, 1919.

[21] D. Ji, T. L. Nguyen, J. Kim, *Adv. Funct. Mater.* **2021**, *31*, 2101095.

[22] J. Y. Sun, X. Zhao, W. R. Illeperuma, O. Chaudhuri, K. H. Oh, D. J. Mooney, J. J. Vlassak, Z. Suo, *Nature* **2012**, *489*, 133.

[23] Q. He, Y. Huang, S. Wang, *Adv. Funct. Mater.* **2017**, *28*, 1705069.

[24] S. Huang, L. Hou, T. Li, Y. Jiao, P. Wu, *Adv. Mater.* **2022**, *34*, 2110140.

[25] M. Hua, S. Wu, Y. Ma, Y. Zhao, Z. Chen, I. Frenkel, J. Strzalka, H. Zhou, X. Zhu, X. He, *Nature* **2021**, *590*, 594.

[26] S. Duan, S. Wu, M. Hua, D. Wu, Y. Yan, X. Zhu, X. He, *iScience* **2021**, *24*, 102989.

[27] S. Lin, J. Liu, X. Liu, X. Zhao, *Proc. Natl. Acad. Sci. U. S. A.* **2019**, *116*, 10244.

[28] X. Liang, G. Chen, S. Lin, J. Zhang, L. Wang, P. Zhang, Y. Lan, J. Liu, *Adv. Mater.* **2022**, *34*, 2107106.

[29] X. Dong, X. Guo, Q. Liu, Y. Zhao, H. Qi, W. Zhai, *Adv. Funct. Mater.* **2022**, *32*, 2203610.

[30] X. Liang, G. Chen, S. Lin, J. Zhang, L. Wang, P. Zhang, Z. Wang, Z. Wang, Y. Lan, Q. Ge, J. Liu, *Adv. Mater.* **2021**, *33*, 2102011.

[31] D. Ye, P. Yang, X. Lei, D. Zhang, L. Li, C. Chang, P. Sun, L. Zhang, *Chem. Mater.* **2018**, *30*, 5175.

[32] L. Li, Y. Zhang, H. Lu, Y. Wang, J. Xu, J. Zhu, C. Zhang, T. Liu, *Nat. Commun.* **2020**, *11*, 62.

[33] J. Dai, H. Qin, W. X. Dong, H. P. Cong, S. H. Yu, *Nano Lett.* **2022**, *22*, 6444.

[34] S. Choi, Y. Choi, J. Kim, *Adv. Funct. Mater.* **2019**, *29*, 1904342.

[35] P. Lin, T. Zhang, X. Wang, B. Yu, F. Zhou, *Small* **2016**, *12*, 4386.

[36] L. Xu, S. Gao, Q. Guo, C. Wang, Y. Qiao, D. Qiu, *Adv. Mater.* **2020**, *32*, 2004579.

[37] C. Liu, N. Morimoto, L. Jiang, S. Kawahara, T. Noritomi, H. Yokoyama, K. Mayumi, K. Ito, *Science* **2021**, *372*, 1078.

[38] H. Lei, L. Dong, Y. Li, J. Zhang, H. Chen, J. Wu, Y. Zhang, Q. Fan, B. Xue, M. Qin, B.

Chen, Y. Cao, W. Wang, *Nat. Commun.* **2020**, *11*, 4032.

[39] L. Liu, M. Zhu, X. Xu, X. Li, Z. Ma, Z. Jiang, A. Pich, H. Wang, P. Song, *Adv. Mater.* **2021**, *33*, 2105829.

[40] L. Xu, C. Wang, Y. Cui, A. Li, Y. Qiao, D. Qiu, *Sci. Adv.* **2019**, *5*, eaau3442.

[41] C. Xiang, Z. Wang, C. Yang, X. Yao, Y. Wang, Z. Suo, *Mater. Today* **2020**, *34*, 7.

[42] Y. Yang, X. Wang, F. Yang, L. Wang, D. Wu, *Adv. Mater.* **2018**, *30*, 1707071.

[43] Y. Wu, Y. Mu, Y. Luo, C. Menon, Z. Zhou, P. K. Chu, S. P. Feng, *Adv. Funct. Mater.* **2021**, *32*, 2110859.

[44] X. Zhu, C. Ji, Q. Meng, H. Mi, Q. Yang, Z. Li, N. Yang, J. Qiu, *Small* **2022**, *18*, 2200055.

[45] M. Li, L. Chen, Y. Li, X. Dai, Z. Jin, Y. Zhang, W. Feng, L. T. Yan, Y. Cao, C. Wang, *Nat. Commun.* **2022**, *13*, 2279.

[46] Junsoo Kim, Guogao Zhang, Meixuanzi Shi, Z. Suo, *Science* **2021**, *374*, 212.

[47] H. Yang, M. Ji, M. Yang, M. Shi, Y. Pan, Y. Zhou, H. J. Qi, Z. Suo, J. Tang, *Matter* **2021**, *4*, 1935.